UNIVERSIDAD COMPLUTENSE DE MADRID

FACULTAD DE CIENCIAS FÍSICAS

Departamento de Física de los Materiales

AC CONTROL OF ATOM DYNAMICS AND TRANSPORT IN BOSE-EINSTEIN CONDENSATES

MEMORIA PARA OPTAR AL GRADO DE DOCTOR
PRESENTADA POR

Martin Heimsoth

Bajo la dirección de los doctores

Fernando Sols Lucia
Charles E. Creffield

MADRID, 2013

Universidad Complutense de Madrid
Facultad de Ciencias Físicas
Departamento de Física de Materiales

PhD Thesis

AC control of atom dynamics and transport in Bose-Einstein condensates

by
Martin Heimsoth

Madrid, April 16, 2013

Supervised by
Fernando Sols Lucia and
Charles E. Creffield

Dedicated to my beloved wife Ana

Contents

List of Publications VII

1. Introduction 1
- 1.1. Ultracold atom gases . . . 1
  - 1.1.1. AC control of ultracold atom systems . . . 2
- 1.2. Ratchet systems . . . 3
- 1.3. Effects of particle interactions . . . 4
- 1.4. Outline of this work . . . 5

2. Few-mode systems 7
- 2.1. Two-mode systems . . . 7
- 2.2. Three-mode systems . . . 8
  - 2.2.1. Effective reduction of Hilbert space . . . 10
  - 2.2.2. Example and numerical cross check . . . 11
- 2.3. Eigenvalue problem of a 3×3-matrix . . . 12

3. Periodically driven systems 15
- 3.1. Extended tt'-formalism . . . 15
  - 3.1.1. Choice of initial loop . . . 18
- 3.2. Linear equations of motion . . . 18
  - 3.2.1. Schrödinger equation . . . 18
  - 3.2.2. Floquet states . . . 19
  - 3.2.3. Generalized view on Floquet quasienergy . . . 20
- 3.3. Nonlinear Schrödinger equation . . . 21
  - 3.3.1. Nonlinear Floquet states . . . 22
- 3.4. Periodic driving in the Heisenberg picture . . . 22
  - 3.4.1. General considerations . . . 22
  - 3.4.2. Field operators in Heisenberg picture . . . 24

4. Orbital Josephson effect in driven BECs 29
- 4.1. The Josephson effect in BECs . . . 29
- 4.2. Generic setup of an OJE . . . 30
  - 4.2.1. Resonantly driven single-particle system . . . 30
  - 4.2.2. Resonantly driven many-particle system . . . 32
- 4.3. Example systems . . . 34
  - 4.3.1. Minimal example: driven two-mode system . . . 34
  - 4.3.2. Box potential with modulated lattice . . . 36

5. Weakly driven coherent quantum ratchets 39
- 5.1. Ratchet systems . . . 39
- 5.2. BECs in ring traps . . . 40
- 5.3. Symmetry aspects . . . 41
- 5.4. Discrete representation . . . 42
- 5.5. Ellipsoidal driving . . . 44

5.6. Factorisable driving . . . 45
5.6.1. Truncated description . . . 46
5.6.2. Numerical study . . . 51

6. Particle interactions in Hamiltonian quantum ratchets **55**
6.1. Many-body quantum systems . . . 55
6.2. Interacting Bose gas on a ring . . . 55
6.3. Translation to tt'-formalism . . . 56
6.4. Truncated picture . . . 57
6.5. Dynamical regimes . . . 58
6.6. Numerical cross-check . . . 59
6.7. Ellipsoidal driving . . . 59
6.7.1. Methods and parameter regimes . . . 59
6.7.2. Simulation results . . . 60
6.7.3. Convergence analysis . . . 63
6.8. Factorizable driving . . . 64
6.8.1. Methods and parameter regimes . . . 64
6.8.2. Effect of detuning . . . 66
6.8.3. Contribution of outer modes . . . 67

7. Three-level system revisited **69**
7.1. Self-trapping in two-mode BECs . . . 70
7.2. Self-trapping and partial self-trapping in three-mode BECs . . . 70
7.3. Parameter space symmetries . . . 73
7.4. Chaos, depletion, and macroscopic superpositions . . . 74
7.5. Two coupled non-rigid pendula . . . 76

8. Conclusions **79**
8.1. Approaching periodically driven systems . . . 79
8.2. Orbital Josephson effect . . . 79
8.3. Hamiltonian quantum ratchets . . . 80
8.4. Outlook . . . 80

Resumen en Español **83**

A. Calculation of Lyapunov exponent within 3GP **87**

B. Generators of Fock space **89**

C. Commutation relations in truncated Hilbert space **91**

D. Glossary **95**

List of publications

Journal articles

1. **Orbital Josephson effect and interactions in driven atom condensates on a ring**
   M. Heimsoth, C. E. Creffield, L. D. Carr, and F. Sols
   New Journal of Physics **14**, 075023 (2012).

2. **Weakly driven quantum coherent ratchets in cold-atom systems**
   M. Heimsoth, C. E. Creffield, and F. Sols
   Physical Review A **82**, 023607 (2010).

3. **Effective Josephson dynamics in resonantly driven Bose-Einstein condensates**
   M. Heimsoth, D. Hochstuhl, C. E. Creffield, L. D. Carr, and F. Sols
   To be submitted to Physical Review A.

4. **Interacting bosons beyond the Gross-Pitaevskii mean-field**
   M. Heimsoth and M. Bonitz
   Physica E **42**, 420-424 (2010).

Selected conference contributions

1. **Orbital Josephson Effect in weakly driven Bose-Einstein condensates**
   M. Heimsoth, C. E. Creffield, and F. Sols
   Poster at the *MUARC & MPAGS Summer school on Quantum Matter* in September 2011, Granada (Spain).

2. **Coherent resonant ratchet currents in driven Bose-Einstein condensates**
   M. Heimsoth, C. E. Creffield, and F. Sols
   Poster at the DPG spring meeting in Hanover, in March 2010.

3. **Orbital Josephson Effect in driven Bose-Einstein condensates**
   M. Heimsoth, C. E. Creffield, L. D. Carr, and F. Sols
   Talk at the Madrid cold atoms conference in December 2011.
   Talk at the *jornada de jóvenes investigadores en física atómica y molecular* in February 2012, Granada (Spain).

4. **Chaos and macroscopic superpositions in a driven Bose gas**
   M. Heimsoth, C. E. Creffield, L. D. Carr, and F. Sols
   Poster at the workshop *Entangle This* at the *Instituto de Física Teórica* in Madrid.

5. **Realizations of novel Josephson dynamics in Bose-Einstein condensates**
   M. Heimsoth, C. E. Creffield, L. D. Carr, and F. Sols
   Poster at the *Theory of Quantum Gases and Quantum Coherence Conference* in Lyon in June 2012.

Seminar talks

1. **Novel Josephson dynamics in Bose-Einstein condensates**
   M. Heimsoth, C. E. Creffield, L. D. Carr, and F. Sols
   At the Center for Quantum Dynamics in Heidelberg, Germany, in July 2012.

2. **Ratchet effect in Bose-Einstein condensates**
   M. Heimsoth, C. E. Creffield, and F. Sols
   Theoretical physics seminar at the Colorado School of Mines.

1. Introduction

Controlling matter by means of time-periodic driving is an exciting prospect that provides the possibility to observe new phenomena, and the design of novel technical applications. A popular example is the periodic excitation of a gain medium, so-called "laser pumping", which is used to produce highly coherent and intense laser light [Sar77]. Another example is the conversion of a semiconductor to a conductive medium by exposing it to electromagnetic radiation [MABW71]. Similarly, the transition of a normal gas to a plasma can be induced by the application of ac-voltages [Stu94] in the radio frequency spectrum. Moreover, the synthesis of complex materials can be vastly accelerated with the assistance of microwave fields [CFFM05].

This work introduces mathematical tools for the study of periodically driven systems, with a strong focus on Bose-Einstein condensates (BECs). The following sections give an overview of state-of-the-art experiments, as well as the underlying theory, with ultracold Bose gases. Special attention is drawn on the possibility to steer these systems, by means of a time-periodic driving field.

1.1. Ultracold atom gases

The emergence and advancement of ultracold atom systems has allowed the study of the dynamics of matter in the absence of thermal effects and decoherence. Atomic BECs are a paradigm of such kinds of system. In the original sense, BECs emerge in three-dimensional ideal Bose gases by passing a phase transition, when the temperature is brought below a critical value T_C. This phenomenon is schematically illustrated in Fig. 1.1. Multiple occupation of a single particle state is possible for particles with integer spin (bosons), which are not subject to the Pauli principle. The first realizations of atomic BECs [AEM+95, DMA+95] were awarded the Nobel prize in physics.

In a more general sense, BECs can be regarded as Bose gases that are well described by a single macroscopic wave-function. Such a generalization is very useful, or even necessary, since many modern experiments do not satisfy the necessary conditions for the creation of a BEC associated with a phase transition. One such example is the theoretical prediction that Bose-Einstein condensation cannot occur at finite temperature in a two-dimensional (2D) system (see e.g. Ref. [KKK+00]). This leads to the concept of a quasicondensate, which describes the macroscopic occupation of the ground mode in a finite-sized Bose gas, e.g. a two-dimensional atomic hydrogen [SVY+98].

As BECs are a coherent matter wave they can be regarded as the atomic counterpart of laser light, which consists of photons. An intriguing experimental manifestation of this analogy can be observed when two spatially separated, but close, condensates expand freely after switching off the trapping potentials. The density profile after sufficiently long expansion, such that both condensates overlap each other, shows interference pattern [ATM+97] that resemble those of Young's double slit experiments with light. Further achievements are the design of wave guides and beam splitter for BECs [GCR+12].

Since the first realization of a BEC based on Rubidium and on Sodium atoms, condensates with many other elements, e.g. Lithium [BSH97], Calcium [BSH97], Ytterbium [BSH97], Cesium [WHM+03], and Chromium [GWH+05] have been achieved, and

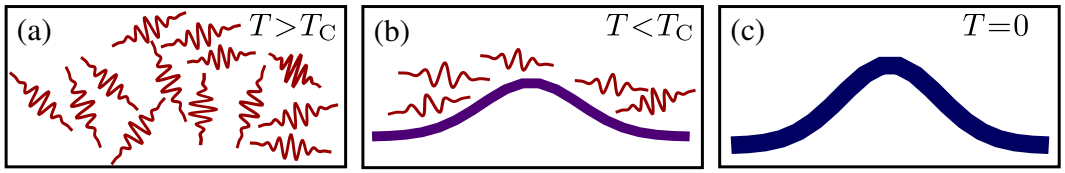

Figure 1.1.: *Heuristic representation of a BEC.* (a) A Bose gas at temperatures beyond the critical temperature T_C can be well described as a classical gas. (b) When the temperature is brought below T_C, the single particle ground mode becomes occupied by a nonzero fraction of the total particle number and form a BEC. (c) An ideal Bose gas at zero temperature is described by a single macroscopic wave function, which is mathematically represented as $|\phi\rangle^{\otimes N}$.

experimentalists have an impressive degree of control over these systems. An extremely valuable tool is the ability to control the strength of particle interactions by means of a Feshbach resonance [PDJ+09]. This allows the interaction strength to be tuned continuously from repulsive to attractive, or to be set to zero. Such a control facilitates the creation of strongly correlated quantum gases, which cannot be found in nature otherwise.

Using the electric field of a laser it is possible to create lattice potentials, known as optical lattices, which can provide insight to many puzzling phenomena of condensed matter systems [LSA+07, MO06]. A famous example is the superfluid to Mott-insulator phase transition, which has been observed in an optical lattice loaded with an ultracold Bose gas [GME+02]. In the Mott-insulating state each lattice site is occupied by a fixed, integer, number of atoms without phase coherence between neighboring lattice sites. It occurs when particle interactions dominate over the the tunneling amplitude between neighboring sites and is a well known phenomenon in solid state physics. Therefore, optical lattices can certainly be regarded as a realization of a so called *quantum simulator*, a concept proposed by Richard Feynman for the study of complex quantum systems. Experiments can also reach the strongly interacting limit of a one-dimensional (1D) dilute Bose gas, which is characterized by the so called Tonks-Giradeau regime [Gir60, PWM+04].

Low dimensional traps with a nontrivial topology, like ring traps [RAC+07, RWM+11, MBS+12] are a further matter of fact of modern experiments with BECs. A main part of this work is dedicated to the study of the creation of particle currents of a BEC inside such ring traps. More generally, one could say that ring traps represent an archetypal setup for the study of superfluidity [KCU08], a phenomenon that is tightly connected to Bose-Einstein condensation.

1.1.1. AC control of ultracold atom systems

In the recent years it has become increasingly popular to use periodic driving to gain further control of ultracold atom systems in general, and Bose gases in particular. In fact, one of the earliest traps for the storage of a BEC is created by a time-averaged orbiting potential (TOP) that emerges from the circular motion of the center of a magnetic quadrupole trap [PAEC95]. Magnetic quadrupole traps harness the Zeeman energy splitting between different magnetic states of the trapped atoms. The idea behind a TOP trap is that the center of the magnetic quadrupole moves much faster than the atoms are able to respond. This concept of an effectively static potential, coming from a far off-resonant driving is an ubiquitous type of ac-control in the field of ultracold quantum gases. A further, equally important, example is the creation of lattice po-

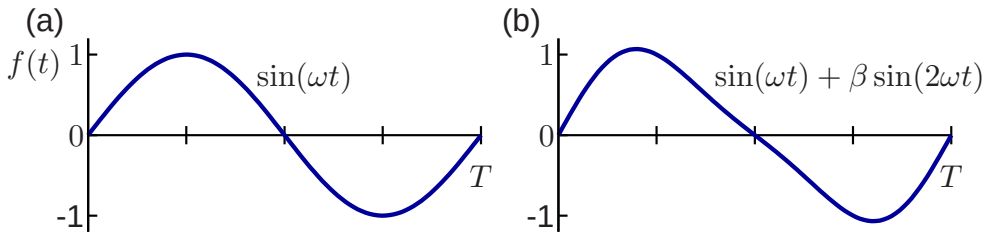

Figure 1.2.: *Breaking time-inversion symmetry by means of bichromatic driving.* (a) A simple harmonic time modulation is inversion symmetric at the extrema. In the depicted case, the mentioned symmetry points are $t = T/4$ and $t = 3T/4$, where T is the period of the modulation. (b) This symmetry gets broken, when a second harmonic is added. The resulting saw-tooth shaped graph gives rise to the term *ratchet potential*.

tentials for ultracold atoms, which are typically formed by the oscillating electric field of a laser [LSA+07]. In this case, the frequency ranges are of the order of magnitude corresponding to transitions of the electronic configurations in the trapped atoms.

Moreover, it has been shown that the tunneling amplitude in a double-well trap can be tuned to zero, using an appropriately adjusted monochromatic driving potential. This surprising phenomenon is called *coherent destruction of tunneling* (CDT) [GDJH91]. Its explanation involves Floquet theory, which is a natural framework for the study of periodically driven quantum systems, analogous to Bloch theory for the case of spatially periodic potentials. In this picture the relevant time scales are determined by the so called (Floquet) quasienergies, and for the case of CDT a degeneracy among the relevant quasienergies leads to infinitely long tunneling times. In a similar manner it is possible to induce localization of particles, equivalent to the Mott-phase, on an optical lattice by means of a monochromatically modulated tilt [CM06]. This idea has been further developed to create lattice potentials with a complex tunneling amplitude among the sites, thus creating an artificial gauge potential [CS11].

Periodically driven BECs form an outstanding arena to study the quantum classical relationship, especially in those regimes where the classical counterpart shows chaotic dynamics [Hol01, BCPS91]. In the theory of (classical) Hamiltonian chaos, the periodically kicked rotor is a paradigmatic system to study the transition from regular to chaotic motion [Sch88]. The time evolution of this system can be solved very efficiently in a time-discretized manner via the Chirikov standard map. An analogous mapping can be applied in the quantum mechanical counterpart, the quantum kicked rotor (QKR). Each kick simply has the effect of a phase imprint on the wave-function, while it evolves freely (without external potential) in between these kicks. The QKR has been intensely studied in the context of a BEC in theoretical [RCM08, MGS08, BG12] and experimental [RAV+06] works. Theoretical studies of a QKR, implemented with a BEC, usually requires the incorporation of particle interactions.

1.2. Ratchet systems

BECs consist of neutral atoms. It is hence not possible to control their motion in the same manner as electrons in electronic circuits. Thus, an intriguing goal of ac-control of quantum gases is the induction of particle currents by means of an unbiased driving potential. This phenomenon is referred to as the "ratchet effect" and is made possible by means of broken space- and time-inversion symmetries, which can explicitly be imposed

on the system via a driving potential [FYZ00].

An typical scheme to break the relevant inversion symmetry, and which will be used in this work, is given by the sum of a first and a second harmonic. This is illustrated in Fig. 1.2 for the case of a time modulation $f(t)$. Lattice potentials that break parity can be created in the same manner. Another possibility to break the time-inversion symmetry is, for example, the inclusion of dissipation [FYZ00, DKH09].

Ratchet systems have been realized, e.g. with mechanical devices [NZCZ01], superconducting setups [ZBSH96, MPG+03], as well as in cold [GBR05] and in ultracold atom gases [SKH+09]. They serve as model for the study of biological molecular motors [JAP97], and more recently, an application of these concepts to control the path of light has been proposed [LC11].

One of the first proposals for a quantum ratchet [RGH97] involved friction and thermal noise as essential features for the creation of directed motion. However, these concepts can be extended to Hamiltonian quantum systems [DF01], where friction is not present. BECs serve as an excellent basis for the study and design of such setups [DMMFH07]. An experimental realization of a Hamiltonian quantum ratchet with a BEC has been accomplished by Salger et al. [SKH+09] on a periodically modulated extended lattice. The breaking of parity and time-inversion symmetry was achieved in the same manner as depicted in Fig. 1.2. In this experiment, the interactions among the particles could be neglected, so that the condensate simply provides an amplification of the single particle dynamics. The role of particle interactions in a BEC-based ratchet has so far mainly been studied within the mean-field limit [CS09, PBC+09, MMF08], which neglects a depletion of the condensate due to particle interactions. One of the main results of this work is that particle interactions can bring these systems far away from this limit, even if it is initially well described by the mean-field approximation.

1.3. Effects of particle interactions

While ideal bosons can be correctly treated in a single particle picture, interactions among the atoms introduce a challenging complexity for both equilibrium and non-equilibrium considerations.

In a finite-sized Bose gas at zero temperature and in thermal equilibrium, particle interactions cause a depletion of the condensate. This means that a fraction of the particles is not in the single-particle ground state[1] [DGPS99]. On the other hand, it was argued by Leggett that interactions can enhance the formation of a condensate [Leg06], because the macroscopic occupation of a single mode with uniform density decreases the total interaction energy. This arises by a combinatorial factor, coming from the underlying Bose statistics. The effect of particle interactions on the critical temperature T_C for the condensate phase transition was studied in a recent experiment [SCTH11]. An expected result is that weak interactions decrease T_C, but they also observe a reduction of this trend for sufficiently strong interactions.

Bringing an interacting many-body quantum system out of equilibrium is a very active field, which is often addressed in the context of ultracold Bose gases [PSSV11]. An important question that is addressed by the study of these complex dynamics is whether a pure many-body quantum state can be ascribed a temperature and an effective statistical ensemble [RDO08, GKL+12], thus probing our fundamental understanding of thermodynamics.

The out-of-equilibrium dynamics can be induced either by a quench, i.e. the sudden change of a system parameter, or by switching on a driving potential. The latter pos-

[1] The ground state of the single-particle part of the Hamiltonian.

sibility can be shown to be mathematically equivalent to a quench, within the so called tt'-formalism [PM93], of which an extended version will be presented in this work.

An unavoidable effect in a non-stationary Bose gas, whose initial preparation is a nearly full condensate, is the depopulation of the condensate wave function [PS03]. As a consequence, the error when describing the system within the mean-field approximation, which assumes a fully condensed system at all times, grows over time. This departure from the mean-field limit can take place in at least two qualitatively different manners. Particles can either scatter into the surrounding gas of non-condensed atoms (depletion) [CD97, CD98], or the system can accumulate a macroscopic amount of particles in further orbitals[2]. This latter process can be termed fragmentation [SS99]. Particle losses due to depletion have become highly controllable in today's experiments and can be neglected in many theoretical considerations [DGPS99, Leg01]. Typically, in a non-stationary Bose gas both processes, occur simultaneously.

Two distinct mechanisms that lead to fragmentation should be pointed out. On one hand the condensate can fragment into independent parts, such that the full state is described by a product state of two or more *condensates*, e.g. states of the type $|\phi_1\rangle^{\otimes N/2} \otimes |\phi_2\rangle^{\otimes N/2}$. This can take place with respect to spatially localized orbitals when the trap features two or more deep potential minima [SS99], but also with respect to delocalized momentum eigenstates in a fermionized homogeneous Bose gases [Pap03]. Alternatively, the system can form a superposition of a Bose gas, being condensed in two macroscopically distinct states [DSC02], e.g. states of the form $|\phi_1\rangle^{\otimes N} + |\phi_2\rangle^{\otimes N}$. Such macroscopic superposition states, or "Schrödinger cat" states, are of high interest from a fundamental viewpoint [Tak05] and there exist several proposed BEC-based protocols for their generation [RCGW98, CLMZ98, MJCZ03].

It was further shown that cat states may arise in BECs for dynamical regimes whose semi-classical limit predicts chaotic motion [WT08]. This aspect has been studied in detail as part of this thesis.

1.4. Outline of this work

This thesis introduces novel approaches for the theoretical study of periodically driven many-body quantum systems, which will be applied, and thoroughly analyzed for the case of resonantly driven BECs. In this context, resonant driving refers to those cases, in which the driving potential induces a coupling among few single particle energy eigenstates of the system without driving. With interacting particles, the dynamics of such systems can be very complex, as will be shown in this work. The approach, introduced here, permits the driven system to be mapped to that of an undriven few-mode Bose gas.

The content of this thesis is subdivided as follows:

Chapter 2 presents some basic calculus for quantum mechanical few-mode systems. The central result of this chapter is a recipe for the calculation of an effective Hamiltonian, when a fraction of the modes participates only marginally in the dynamics. It further contains calculations of asymptotically time-averaged expectation values of certain observables, as well as the identification of relevant time scales.

Chapter 3 introduces a mathematical framework for the treatment of time-periodic systems: the extended tt'-formalism. It starts with a presentation of this formalism, using only very general assumptions on the underlying equation of motion. The subsequent parts of this chapter discuss its application to three different types of equation of

[2] An occupation of further orbitals can be detected via the eigenvalues of the single-particle density matrix.

motion that are relevant for this thesis. Those are the Schrödinger equation, the nonlinear Schrödinger equation, and the Heisenberg equation of motion for field operators. For the first case, its relation to Floquet theory is pointed out.

In Chapter 4 these concepts are used for the derivation of an effective few-mode description for a periodically driven BEC. The structure of the corresponding few-mode Hamiltonian allows the underlying systems to be considered as bosonic Josephson junctions. The participating modes are wave functions whose density may overlap strongly. These characteristics led to the name *orbital Josephson effect*. The mathematical derivations in this chapter are supported with some numerical evidence. In the beginning of this chapter, an introduction to bosonic Josephson junctions will be given .

Chapter 5 presents an analysis of the underlying mechanisms for the creation of coherent ratchet currents in resonantly driven BECs with vanishing particle interactions. The main focus is given to two different driving potentials which both yield an effective time-independent few-mode Hamiltonian, referring to transporting modes in both directions and the initial non-transporting single particle mode. For one case, a perturbative approach of the type presented in Chapter 2 is used. Furthermore, a geometrical construction to determine the resonance condition is introduced.

Chapter 6 shows how the description as an orbital Josephson junction can be applied to study the role of particle interactions in Hamiltonian quantum ratchets. The two main types of ratchet potential, introduced in Chapter 5, are considered, and a thorough numerical comparison between the effective few-mode description and the full dynamics is presented for one of them. A main result is that the approach introduced here is correct, and in some cases clearly preferable over a mean-field approximation, because many-body effects may become important.

Chapter 7 goes more into detail with the dynamics of a bosonic three-level system, which arises as an effective description in Chapter 6. Special attention will be paid to the self-trapping transition and to chaotic dynamics. In the latter case, peaked particle number correlations hint at the creation of macroscopic superposition states.

The appendix presents detailed calculations that are needed for an understanding of the mathematical derivations in this work, but do not fit into the main chapters. Appendix A gives details about the calculation of the Lyapunov exponent, which is used to identify chaotic dynamics in the system. In appendix B is shown that any operator in a bosonic or fermionic Fock space can be expressed in terms of annihilation and creation operators. Finally, in appendix C, the commutation relations of creation and annihilation operators within the extended tt'-formalism are derived for the case of a truncation of Hilbert space to three modes.

2. Few-mode systems

An ubiquitous simplification for the study of quantum systems is the truncation of Hilbert space to a small number of states, or, in the case of a many-particle system, a truncation to a small number of orbitals. Such few-mode descriptions form a recurring element of this work. In this chapter, we will introduce a graphical representation for few mode Hamiltonians, and analyze in which cases further reductions to fewer modes is allowed and how this is done. To this end, we will introduce the T-matrix, which allows the calculation of an effective coupling between two modes perturbatively[1]. This chapter solely deals with time-independent Hamiltonians.

All considerations presented in this chapter, refer to single particle systems. Equivalently, one could also think of them as a BEC of ideal Bosons, whose macroscopic wave-function can be described by the superposition of a few modes.

Concepts, presented in the following, are kept relatively simple and will be referred to in subsequent chapters.

2.1. Two-mode systems

A two-mode system is the simplest nontrivial quantum system and is sometimes referred to as pseudo-spin. The dynamics of such a system is governed by the Schrödinger equation

$$i\partial_t \left|\psi(t)\right\rangle = H \left|\psi(t)\right\rangle , \tag{2.1}$$

where we have set $\hbar = 1$ and the state $|\psi\rangle$ can be represented by a tuple of complex numbers. In the same basis, the Hamilton operator can be represented by a complex Hermitian 2×2-matrix

$$H = \tfrac{1}{2} \begin{pmatrix} \mu & \Gamma \\ \Gamma^* & -\mu \end{pmatrix} , \tag{2.2}$$

where the basis states are labeled as $|\mathrm{L}\rangle$ (left) and $|\mathrm{R}\rangle$ (right). Therefore, the state $|\psi\rangle$ is given by $|\psi\rangle = c_\mathrm{L} |\mathrm{L}\rangle + c_\mathrm{R} |\mathrm{R}\rangle$.

Figure 2.1c shows a graphical representation of Hamiltonian (2.2). The characteristics of the represented system are encoded as follows:

1. The modes are represented by nodes – see labels inside the circles.
2. The coupling strengths $|\Gamma|$ among them is represented by the thickness of the connecting line – Fig. 2.1a.
3. A potential difference μ is indicated by a vertical shift among the modes – Fig. 2.1b.

A complex phase of the coupling Γ is not represented in this picture.

Note that these graphical representations explicitly refer to a certain basis. Consequently, they rather depict matrix representations of a Hamiltonian, instead of the underlying abstract operators.

[1] The idea to use the T-matrix as effective Hamiltonian has been presented in [HCS10] as part of the PhD project of this thesis.

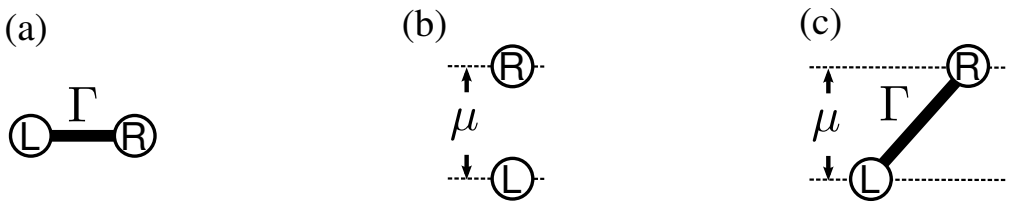

Figure 2.1.: *Network representation of a Hermitian two-mode matrix.* Panels (a) and (b) show representations with vanishing potential difference and with vanishing coupling strength respectively.

Let us briefly analyze Hamiltonian (2.2). The characteristic polynomial of H is of second order, what allows the calculation of its eigenvalues, and from that the related eigenvectors, analytically:

$$\text{eigenvalues: } \varepsilon_\pm = \pm\tfrac{1}{2}\Omega_\mathrm{R}, \quad \text{eigenvectors: } \frac{1}{\mathcal{N}_\pm}\begin{pmatrix} -\Gamma \\ \pm\Omega_\mathrm{R} - \mu \end{pmatrix}, \tag{2.3}$$

where $\Omega_\mathrm{R} = \sqrt{|\Gamma|^2 + \mu^2}$ is the systems Rabi frequency[2], and the normalization factor is $\mathcal{N}_\pm = \sqrt{2\Omega_\mathrm{R}(\Omega_\mathrm{R} \mp \mu)}$.

The Rabi frequency is the energy difference between the two eigenstates of Hamiltonian (2.2). For non-stationary states, $|\psi\rangle$, the time evolution of observables oscillates with the Rabi frequency. It hence serves as a natural energy scale of the system, and the Rabi period $T_\mathrm{R} = 2\pi/\Omega_\mathrm{R}$ serves as natural time scale. Two-mode matrices are often expressed in terms of the Pauli matrices [CS09, GH98], which is not adopted here, in order to extend the concepts to more than two modes.

2.2. Three-mode systems

In principle, the graphical representation of a two-mode system, presented in the previous section, can be extended to any number of modes that are present in the system. In this section, we will consider a certain type of three-mode system. We will label the modes as L (left), C (center), and R (right). A graphical representation of the system considered in the following is given in Fig. 2.2a. It combines the following properties:

(a) The side modes L and R have the same potential energy.

(b) The potential energy of the center mode C is far away from modes L and R.

(c) There is no direct coupling between L and R.

(d) The initial state is either in L or R or a superposition of both. That is, the particle density in C vanishes initially.

(e) The coupling strengths Γ_L and Γ_R is nonzero and far below the energy difference between the center mode C and the side modes, L, and R.

This system can be considered a discrete analog of a tunneling setup. To clarify this statement, let us assume that the particle is initially located in the left mode $|\psi(t=0)\rangle = |\mathrm{L}\rangle$. It is energetically allowed, to be located in the right mode during the dynamics, but the particle can only arrive there via the center mode C, which can be considered an

[2]The subindex R stands for Rabi, not the label of the right mode.

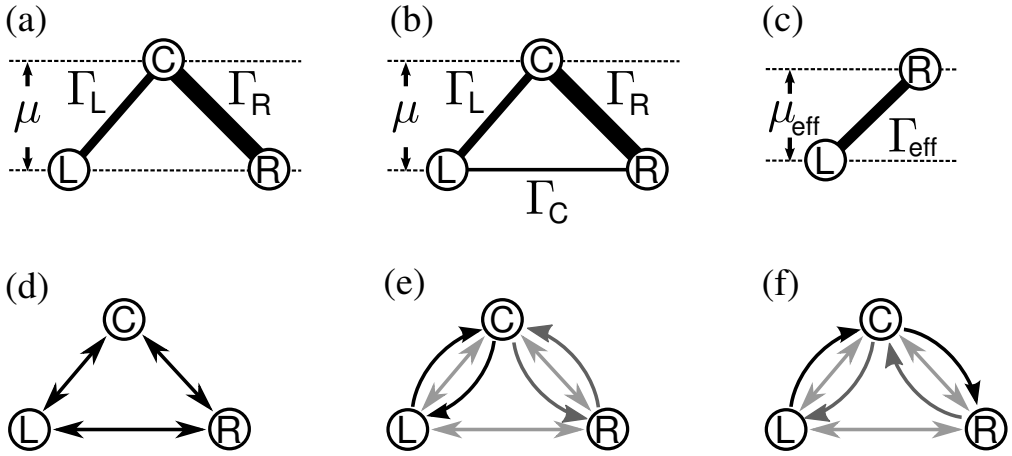

Figure 2.2.: *Network representation with three modes and dynamical processes.* In the depicted three-mode systems, the potential energy of the center mode is shifted with respect to the side modes L and R. The only difference between (a) and (b) is that system (b) features a non-vanishing direct coupling between modes L and R. The lower row depicts main dynamical processes of the here considered three-mode system: (d) direct coupling between modes (elementary process), (e) virtual excitation, and (f) transition to other side mode via center mode. All these processes contribute to the parameters of the effective two-mode system (c).

energetically forbidden mode – cf. item (b) above. Consequently, the system is expected to behave as an effective two-mode system, in which the particle oscillates between L and R, while the particle density in the center mode is negligible throughout the dynamics. One might also say that the center mode is only *visited virtually*.

We will see in the following that the three-mode system considered here can indeed be described as an effective two-mode system – see Fig. 2.2c. It will be shown here how to calculate the parameters Γ_{eff} and μ_{eff} of the effective two-mode system with a perturbative scheme.

We can slightly modify our three-mode Hamiltonian by allowing a nonzero direct coupling Γ_C between L and R – see Fig. 2.2b. In this case, the particle can transit from the left mode to the right mode via two paths:

I. Via the link with strength Γ_C (direct).

II. By passing through the center mode (indirect).

That means that the two modes L and R are effectively coupled via two links with different strengths and, in general, different phases. The question is now, how the two links combine into one effective link. In other words, does the interplay between both paths always yields an enhanced effective coupling between L and R, or can they *interfere* constructively and destructively? This problem resembles the combination of several parallel connections between two vertices in an electronic circuit, which is described by Kirchoff's laws.

The technique that gives answers to these questions is a perturbative calculation, involving Green's functions.

2.2.1. Effective reduction of Hilbert space

In the following, we will determine an effective two-level description of the system, depicted in Figs. 2.2ab. We have noted previously that a particle which is initially prepared in the left mode can transit to the right mode either directly (Fig. 2.2a) or via the center mode (Fig. 2.2c). Both these processes contribute to the effective coupling among the side modes L and R. A further process consists in a transition to the center mode and going back to the initial side mode, which is expected to modify the potential energy of each of the side-modes.

The Hamiltonian of the three-level system depicted in Fig. 2.2b is represented by the matrix

$$H_{3\mathrm{LS}} = \begin{pmatrix} \mu & \Gamma_\mathrm{L} & \Gamma_\mathrm{C} \\ \Gamma_\mathrm{L}^* & 0 & \Gamma_\mathrm{R} \\ \Gamma_\mathrm{C}^* & \Gamma_\mathrm{R}^* & \mu \end{pmatrix}. \tag{2.4}$$

Our goal is to obtain an effective two-level system, cf. Eq. (2.2), involving only the side modes L and R. Note that a simple projection of $H_{3\mathrm{LS}}$ onto the subspace, given by the span of $|\mathrm{L}\rangle$ and $|\mathrm{R}\rangle$ is not sufficient, since this would not involve the indirect processes, shown in Figs. 2.2bc.

In order to apply a perturbative approach, we consider $H_{3\mathrm{LS}}$ to be split up in two parts: We consider the matrix that contains solely the diagonal elements $H_\mu = \mathrm{diag}(\mu, 0, \mu)$ as unperturbed Hamiltonian, and the off-diagonal terms, given by $H_\Gamma = H_{3\mathrm{LS}} - H_\mu$, will be considered the perturbation. According to this decomposition of $H_{3\mathrm{LS}}$, the indirect processes, as depicted in Figs. 2.2ef, are in second order of the perturbation H_Γ. Consequently, the following approach is expected to work best for

$$|\mu| \gg \Gamma \equiv \sqrt{|\Gamma_\mathrm{L}|^2 + |\Gamma_\mathrm{C}|^2 + |\Gamma_\mathrm{R}|^2}. \tag{2.5}$$

The effects from the perturbation H_Γ are described in terms of the T-matrix, which is given by the relation [Eco06]

$$T(z) = H_\Gamma + H_\Gamma G^0(z) T(z), \tag{2.6}$$

where z is a complex parameter and $G^0 \equiv (z - H_\mu)^{-1}$ is the Green's function of the unperturbed system. In order to obtain an expansion of $T(z)$ in terms of H_Γ and G^0, we iterate Eq. (2.6). This yields

$$T(z) = H_\Gamma + H_\Gamma G^0(z) H_\Gamma + H_\Gamma G^0(z) H_\Gamma G^0(z) H_\Gamma + \dots \ . \tag{2.7}$$

According to previous considerations, an approximation of $T(z)$ to second order in H_Γ should be sufficient. This means

$$T(z) \approx H_\Gamma + H_\Gamma G^0(z) H_\Gamma. \tag{2.8}$$

The T-matrix, approximated to second order, yields an effective perturbation which yields the correct second order dynamics, when treated to first order [Eco06]. Since the eigenvalues $|L\rangle$ and $|R\rangle$ for the unperturbed case are $\varepsilon_{L/R} = 0$ the z-dependence is omitted and we assume $z = 0$. Accordingly, the effective coupling between the side

modes is then given by

$$\begin{aligned}\Gamma_{\text{eff}} &= \langle \mathrm{L}|T|\mathrm{R}\rangle = \langle \mathrm{L}|H_\Gamma|\mathrm{R}\rangle + \langle \mathrm{L}|H_\Gamma|\mathrm{C}\rangle \frac{1}{-\mu} \langle \mathrm{C}|H_\Gamma|\mathrm{R}\rangle \\ &= \Gamma_\mathrm{C} - \frac{\Gamma_\mathrm{L}\Gamma_\mathrm{R}}{\mu},\end{aligned} \tag{2.9}$$

and the effective potential energy of the left mode, coming from a second order process in H_Γ (see Fig. 2.2e), reads

$$\langle L|T|L\rangle = \langle \mathrm{L}|H_\Gamma|\mathrm{C}\rangle \frac{1}{-\mu} \langle \mathrm{C}|H_\Gamma|\mathrm{L}\rangle = -\frac{|\Gamma_\mathrm{L}|^2}{\mu}, \tag{2.10}$$

and analogously $\langle R|T|R\rangle = -|\Gamma_\mathrm{R}|^2/\mu$, for the right mode. With these matrix elements, the parameter of the effective two-mode system involving solely L and R are fully determined.

With Eq. (2.9) we can now answer the questions that have been raised previously about how the couplings, related with each possible path combine to an effective coupling. The effective coupling is a sum of the couplings for each path and this sum respects the signs and phases of each of the contributing junctions or effective junctions. In particular this means that two paths can result in an effective coupling that is stronger than each of the couplings associated to each path (constructive combination); or both paths can result in an effectively vanishing coupling (destructive combination). This resembles the addition of conductances to a total conductance in a parallel electrical circuit.

In the next section we will see how the effective two-level description compares to a numerical solution of the full system.

2.2.2. Example and numerical cross check

In the following, we consider numerical solution of the dynamics, governed by Hamiltonian (2.4), using an exact diagonalization routine for the calculation of the unitary time-evolution operator[3]. We consider $|\psi_0\rangle = |\mathrm{L}\rangle$ as initial state. In this case, the dynamics can be described by an effective two-mode system (2.2), involving the side modes L and R, with effective coupling given in Eq. (2.9) and with effective potential energy for each mode given in Eq. (2.10). The dynamics with respect to the effective description was calculated analytically by solving the corresponding eigenvalue problem.

The dynamics of the full system is represented as

$$|\psi(t)\rangle = A_\mathrm{L}(t)\,|\mathrm{L}\rangle + A_\mathrm{C}(t)\,|\mathrm{C}\rangle + A_\mathrm{R}(t)\,|\mathrm{R}\rangle\,, \tag{2.11}$$

and the truncated representation is obtained simply by setting $A_\mathrm{C} \equiv 0$.

Fig. 2.3 shows a comparison between the dynamics of the full system (black curve) and the effective description (red curve). It can be seen that the effective description works best for large values of μ (Fig. 2.3c). The participation of the center mode, shown in Fig. 2.3d, is weak in all considered cases and decreases slowly with increasing μ, while the frequency of the fast oscillation increases. For relatively small values of μ, shown in Fig. 2.3a, two main differences between effective description and full dynamics can be observed:

1. In the full dynamics, the curve shows a fast oscillatory onset on top of the long-time dynamics. The amplitude of this onset decreases for increasing μ, while its frequency raises.

[3] In principle, a 3×3 matrix could still be diagonalized analytically.

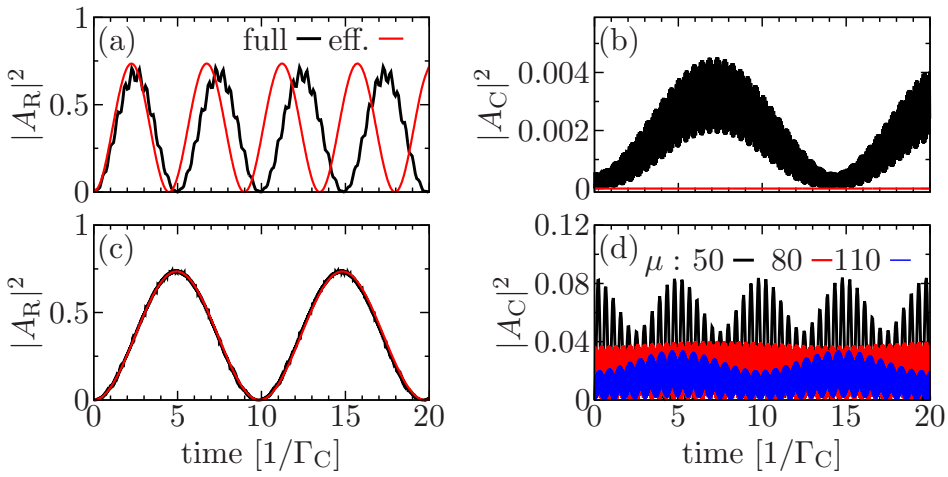

Figure 2.3.: *Dynamics of a three-mode system and its effective two-mode description.* Three different regimes, referring to three different potential energies of the center mode μ are considered: (a) for $\mu = 50$ the second order contribution dominates, (b) both contributions interfere destructively for $\mu = 80$, and (c) for $\mu = 110$ the first order path dominates. Panels (a-c) show the occupation of the right mode $|A_R|^2$, cf. Eq. (2.4). In (d) the contribution of the center mode $|A_C|^2$ is shown. Coupling strengths for all cases are $\Gamma_L = 8$, $\Gamma_C = 1$, and $\Gamma_R = 10$. The weak coupling condition $\Gamma \approx 12.8 < \mu$ is satisfied for all considered values of μ, cf. Eq. (2.5). All parameters are given in units of $|\Gamma_C|$, which serves here as a natural energy scale, and its inverse as natural time-scale.

2. The frequencies of the long-time oscillations do not match precisely, such that a discrepancy between both curves is described by a beat. This beat is also reflected in the time evolution of the occupation of the center mode.

For the case shown in Fig. 2.3b the two paths interfere destructively, yielding a vanishing effective total coupling in a second order calculation. Nevertheless, we see that in the full dynamics, the system transits slightly to the right mode, with an amplitude, two orders of magnitude smaller than the other considered cases. These oscillations arise from third order contributions or higher.

In Fig. 2.3c both descriptions agree so well that the curves overlap each other during the entire considered time range.

2.3. Eigenvalue problem of a 3×3-matrix

Since the characteristic polynomial of a 3×3-matrix has degree 3, it is in principle possible to give a general solution to the related eigenvalue problem. Nevertheless, for the purpose of this thesis it is sufficient to consider only a certain class of 3×3-matrix. This way we avoid unnecessarily cumbersome mathematical terms. The class of matrices considered here is obtained from the matrix in Eq. (2.12) by setting the coupling term Γ_C to zero:

$$H = \begin{pmatrix} \mu & \Gamma_L & 0 \\ \Gamma_L^* & 0 & \Gamma_R \\ 0 & \Gamma_R^* & \mu \end{pmatrix} \tag{2.12}$$

In this case we do not assume the condition (2.5) to be valid, such that in general the study of the full matrix is necessary. Its eigenvalues are given by the zeros of its

characteristic polynomial

$$p(\varepsilon) = -\varepsilon(\varepsilon-\mu)^2 + \Gamma^2(\varepsilon-\mu)\ , \tag{2.13}$$

with Γ given in Eq. (2.5). The zeros of $p(\varepsilon)$ are

$$\tilde{\varepsilon}_0 = \mu,\ \tilde{\varepsilon}_\pm = \tfrac{1}{2}(\mu \pm \Omega_\mathrm{R}), \tag{2.14}$$

with Rabi frequency $\Omega_\mathrm{R} = \sqrt{4\Gamma^2+\mu^2}$. The corresponding eigenvectors are

$$|\tilde{0}\rangle = \frac{1}{\Gamma}\begin{pmatrix}\Gamma_\mathrm{L}\\ 0\\ -\Gamma_\mathrm{R}^*\end{pmatrix},\ |\tilde{\pm}\rangle = \frac{1}{\mathcal{N}_\pm}\begin{pmatrix}-2\Gamma_\mathrm{R}\\ \mu\mp\Omega_\mathrm{R}\\ -2\Gamma_\mathrm{L}^*\end{pmatrix}\ , \tag{2.15}$$

with the normalization factor $\mathcal{N}_\pm = \sqrt{2\Omega_\mathrm{R}(\Omega_\mathrm{R}\mp\mu)}$.

For later chapters, the consideration of the initial state $|\psi_0\rangle = |\mathrm{C}\rangle$ is of special interest. In this case, the eigenvector[4] $|\tilde{0}\rangle$ does not participate in the dynamics of the system, because its overlap with $|\mathrm{C}\rangle$ vanishes. This means that the dynamics can be further reduced to an effective two-level system involving the only the two eigenvectors $|\tilde{\pm}\rangle$. In contrast to previous sections, the truncation in this case is exact and does not require a perturbational approach. Another representation of this two-level system is given by the orthonormal vectors $|\mathrm{C}\rangle$ (the initial vector) and

$$|a\rangle = \langle\tilde{-}|\mathrm{C}\rangle\,|\tilde{+}\rangle - \langle\tilde{+}|\mathrm{C}\rangle\,|\tilde{-}\rangle = \frac{1}{\Gamma}\begin{pmatrix}\Gamma_\mathrm{R}^*\\ 0\\ \Gamma_\mathrm{L}\end{pmatrix}\ . \tag{2.16}$$

Hence, the system oscillates between the two modes $|0\rangle$ and $|a\rangle$, with the frequency Ω_R. Note that for $\mu \neq 0$, the system does not transit completely from the initial state $|0\rangle$ to $|a\rangle$, because of energy conservation.

These results can be used for the calculation of asymptotic time-averaged expectation values. For later purposes we consider two observables given by the matrices

$$E_\mathrm{kin} = \begin{pmatrix}1&0&0\\0&0&0\\0&0&1\end{pmatrix},\ \text{and}\ I = \begin{pmatrix}1&0&0\\0&0&0\\0&0&-1\end{pmatrix}, \tag{2.17}$$

which will later be identified (up to a prefactor) as representations of kinetic energy and particle current respectively. Using the recipe given in Box 2.3.1, we obtain the Lorentzian

$$\bar{E}_\mathrm{kin} = \left[1+\left(\frac{\mu}{2\Gamma}\right)^2\right]^{-1} \tag{2.18}$$

for the time-averaged kinetic energy and for the time-averaged particle current we obtain

$$\bar{I} = 4(|\Gamma_\mathrm{R}|^2 - |\Gamma_\mathrm{L}|^2)/\Omega_\mathrm{R}^2. \tag{2.19}$$

[4] The state $|\tilde{0}\rangle$ is called $|b\rangle$ in Ref. [HCS10].

Box 2.3.1 | Time averaged expectation value

The solution of the Schrödinger equation with a time-independent Hamiltonian can be expressed as

$$|\psi(t)\rangle = \sum_n e^{-\mathrm{i}\mathcal{E}_n t} \hat{P}_n \, |\psi_0\rangle \, ,$$

where $\hat{P}_n$ is the projector onto the eigenspace with energy eigenvalue $\mathcal{E}_n$ and $|\psi_0\rangle$ is the initial state. The infinite time averaged expectation value of observable A is given by

$$\bar{A} = \lim_{\tau\to\infty} \frac{1}{\tau} \int_0^\tau dt \, \langle\psi(t)|\hat{A}|\psi(t)\rangle \, .$$

By inserting the sum for $|\psi(t)\rangle$, we obtain

$$\bar{A} = \sum_n \langle\psi_0|\hat{P}_n \hat{A} \hat{P}_n|\psi_0\rangle \, .$$

Conclusions

We have analyzed certain aspects of a few-mode systems, which encompass two or three modes. In the present analysis the related eigenvalue problems are considered and relevant time and energy scales have been identified. An important result of this chapter is the development of a recipe for the calculation of the effective Hamiltonian, when a system can be further truncated to fewer modes and when the contribution of second order processes is relevant. The largest few-mode system, encountered in this work involves five modes.

3. Periodically driven systems

This chapter presents common and new approaches for the study of time-periodically driven systems, with a strong emphasis on the treatment of quantum systems.

Floquet theory is a fundamental method for the analysis of periodically driven quantum systems. In principle, this technique requires the underlying equation of motion to be linear. Nevertheless, there exist proposals to extend some concepts from Floquet theory to nonlinear equations of motion [Hol01, MMF08, WDWD12]. A more recently developed alternative is the so called *geometric-phase-propagator* approach [DKK+12].

Another framework for the analysis of time-periodic systems is the so called tt'-formalism [PL83, PM93], which has been shown to be a very successful method for the study of linear systems and is tightly connected to Floquet theory. So far, this framework has been extended to treat aperiodic [MCL95], or quasi-periodic systems [MS06], i.e. perturbations with several dissonant frequencies involved. It has been proven to be an efficient approach for the study of linear systems with a periodic driving field [MCL95, MS06, MW97].

This chapter introduces a further extension of the tt'-formalism to treat nonlinear equations of motion and apply this extension to the Heisenberg equation of motion for field operators[1]. The following paragraphs give an introduction to the extended tt'-formalism for a general setup. After that it will be applied to three different equations of motion which are of special interest for the subsequent chapters of this work:

1. Linear equations of motion, e.g. the Schrödinger equation. This part includes an introduction to Floquet theory.

2. The Gross-Pitaevskii (GP) equation or nonlinear Schrödinger equation. Here, we will see that stationary solutions yield the so called nonlinear Floquet states.

3. Heisenberg equation of motion for field operators.

In previous works, where the tt'-formalism has been derived for the special case of linear systems [PL83, PM93], the linearity of the underlying equation of motion was assumed and used. To be precise, the solution of a Schrödinger equation with a static Hamiltonian was expressed via a unitary time-evolution operator, given by the exponential of the Hamiltonian. Such an approach cannot be used for an extension to arbitrary equations of motion. Therefore, we will follow a different path, presented in the following section.

3.1. Extended tt'-formalism

Our goal is to map systems with an underlying time-periodic equation of motion to systems without explicit time dependence. This is realized by an extension of the tt'-formalism. The dynamics of a system is typically determined by the initial state and the underlying equations of motion. The solution of such an initial-value problem can

[1] An extension of the tt'-formalism to bosonic field operators has been published in Ref. [HCCS12] as part of this thesis. A publication containing the general version of this extension is in preparation [HHC+].

be represented by a trajectory in the corresponding phase space $\mathcal{P}$. For now, we do not need to make any further assumptions on the properties of $\mathcal{P}$. It can have finite or infinite dimensions and does not have to be a Hilbert space. We will later discuss in greater detail the above listed cases.

The point in $\mathcal{P}$ which indicates the state of the system will be denoted by v. The corresponding initial-value problem can be written as

$$\frac{d}{dt}v(t) = F\big[v(t), t\big], \text{ and } v(0) = v_0. \tag{3.1}$$

As mentioned above, we restrict our considerations to time-periodic systems,

$$F[\cdot, t+T] = F[\cdot, t], \tag{3.2}$$

where T is the period. In any other sense, F is arbitrary. It can be nonlinear, discontinuous in v or in t, and of course it is allowed to have no explicit time-dependence at all. In this case the period T can be chosen freely. The solution to Eq. (3.1) forms a trajectory in $\mathcal{P}$, schematically represented by the red curve in Fig. 3.1.

Now consider an arbitrary generalized *loop* embedded in the phase space $\mathcal{P}$, given by

$$\bar{v}(t') \in \mathcal{P} \text{ for all } t' \in [0, T] \text{ and } \bar{v}(0) = \bar{v}(T); \tag{3.3}$$

where $\bar{v}(t')$ is allowed to be degenerate, such that is forms, e.g., a point ($\bar{v}(t') \equiv \bar{v}_0$) or to a line. It hence, strictly speaking, does not necessarily form a loop, therefore the term *generalized loop*. The black line in Fig. 3.1 represents such a loop in $\mathcal{P}$. This generalized loop may evolve in time according to the initial-value problem

$$\begin{aligned}\frac{\partial}{\partial t}\bar{v}(t', t) &= \mathcal{F}\big[\bar{v}(t', t), t'\big] \\ &\equiv F\big[\bar{v}(t', t), t'\big] - \frac{\partial}{\partial t'}\bar{v}(t', t), \text{ and } \bar{v}(t', 0) = v_0,\end{aligned} \tag{3.4}$$

where the first argument t' in $\bar{v}$ is the parametrization of the loop at time instant t. Note that $\mathcal{F}$ is a more general object than F, since it contains a partial derivative of $\bar{v}$ with respect to t'. The periodicity of $\bar{v}(t', t)$ in t' is preserved over time, since $F(\cdot, t')$ is periodic with period T. The dynamics of this generalized loop describes a surface with the structure of a generalized tube embedded in the phase space of the considered system. The gray surface in Figure 3.1 represents the generalized tube in $\mathcal{P}$. The trajectory described by Eq. (3.1) winds around it, which will be explained in the following. We are looking for an equation of motion that determines a parametrized family of curves through this surface. This family, with parameter τ, is given by

$$v'_\tau(t) \coloneqq \bar{v}(t'_\tau(t), t), \tag{3.5a}$$

$$\text{with } t'_\tau(t) \coloneqq (t + \tau) \bmod T\ . \tag{3.5b}$$

Since $\bar{v}(t', t)$ and $\mathcal{F}$ are periodic in t', it is sufficient to restrict ourselves to $\tau \in [0, T]$. An equation of motion for $v'_\tau(t)$ can be obtained by deriving both sides of Eq. (3.5a) with respect to t. The first argument of $\bar{v}$ on the right hand side of the definition (3.5) is itself a function of t. Therefore, we have to derive partially with respect to both arguments

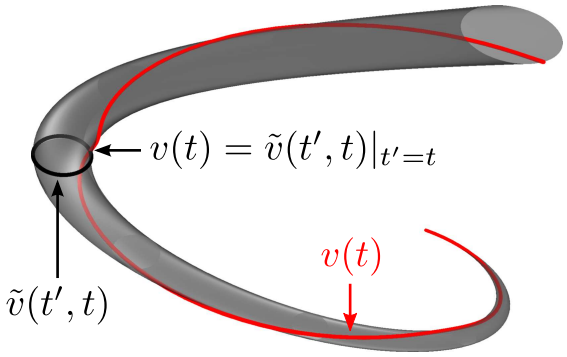

Figure 3.1.: *Illustration of extended tt' formalism.* The dynamics of the system is described by a tube (gray surface) instead of a trajectory in phase-space. The physically relevant trajectory (red line) is embedded on the surface of the tube and can be recovered by setting $t' = t$. A snap-shot of the system described by Eq. (3.4) is now given by a loop (black line), instead of a point.

of $\bar{v}$ and apply the chain rule for the case of the first argument. This yields

$$\frac{d}{dt}v'_\tau(t) = \frac{d}{dt}\bar{v}(t'_\tau(t), t) = \underbrace{\frac{\partial t'}{\partial t}}_{=1}\frac{\partial \bar{v}(t', t)}{\partial t'} + \frac{\partial \bar{v}(t', t)}{\partial t}\bigg|_{t'=t'_\tau(t)} = F\big[\bar{v}(t'_\tau, t), t'_\tau\big]. \tag{3.6}$$

Here, t'_τ is always meant to be a function of t, although it is not explicitly expressed. Because of the periodicity of $F[v, \cdot]$, the modulus operation does not have any effect within the second argument of F. The same holds for the first argument of $\bar{v}$. Hence, we obtain the equation of motion for $v'_\tau(t)$, given by

$$\frac{d}{dt}v'_\tau(t) = F\big[v'_\tau(t), t + \tau\big]. \tag{3.7}$$

With the initial condition $v'_\tau(0) = v_0$, following from Eq. (3.4). This means that for each $\tau \in [0, T]$, $v'_\tau(t)$ is the solution to the parametrized initial-value problem

$$\frac{d}{dt}v(t) = F\big[v(t), t + \tau\big], \text{ and } v(0) = v_0, \tag{3.8}$$

with parameter τ. In particular, the solution to the initial-value problem (3.1) is obtained by

$$v(t) = \bar{v}(t, t). \tag{3.9}$$

Note that the t'-dependence of $\bar{v}$ is originally restricted to the interval $[0, T]$. However, since periodic boundary conditions are imposed in Eq. (3.3), we can directly extend $\bar{v}(t')$ to be defined on the entire real axis.

The extension of the tt'-formalism presented here is very general and does not refer to the particular case of quantum systems. It can be applied to study, e.g., the dynamics of a driven pendulum, with and without dissipation; classical or quantum ratchet systems; or the dynamics of classical fluids under time-periodic forces. However, since this thesis focuses on the dynamics of ultracold atomic gases, the discussions in the subsequent sections are restricted to its application to equations of motion that describe quantum mechanical systems.

3.1.1. Choice of initial loop

In principle, the loops which are introduced here contain more information than we are originally interested in. The approach, presented above, still holds when the initial loop $\bar{v}(t',0)$ differs from the one given in Eq. (3.4). The correct trajectory of the system can be recovered from $\bar{v}$, always when it initially holds $\bar{v}(0,0) = v_0$, where v_0 is the considered initial state of the system. This condition only fixes the value of $\bar{v}(t',0)$ for the point $t' = 0$, the t'-dependence on the remaining interval can be chosen freely, with the only constraint that $\bar{v}$ should be differentiable in both arguments. A convenient choice for the initial loop that satisfies this condition is given by

$$\bar{v}(t',0) \equiv v_0 \,, \tag{3.10}$$

which was used in the previous section [see Eq. (3.4)] and will be called standard initial conditions in this work. With the standard initial conditions, we can assign a physically relevant meaning to $\bar{v}(t',t)$ also for $t' \neq t$, as has been shown above. The state given by $\bar{v}(t',t) = \bar{v}(t+\tau,t)$ is the state the system would have at time t, if the function $F[v,t]$ had a phase shift τ in the time parameter – see Eq. (3.8).

In physical systems, where the time-dependence comes from a driving field $V(t)$, the loop $\bar{v}(t',t)$ describes the set of solutions referring to different times t_0 at which the field is switched on.

3.2. Linear equations of motion

The above presented introduction to the extended tt'-formalism was kept completely general. It can be applied to classical and quantum systems. In the following, we will apply these concepts to systems that are of special interest in this thesis.

Linear time-periodic equations of motions are typically analyzed in the context of Floquet theory [GH98]. This section introduces this technique and points out its connection to the tt'-formalism. Moreover, this section serves as introduction of important basic concepts that will be needed in the subsequent sections and chapters. Those concepts comprise extensions of the Hilbert space for time-periodic wave functions (Sambe space), Floquet states, and quasienergies. Furthermore, for linear systems it can be seen that the parameter t' from the tt'-formalism accounts for dynamics on time scales shorter than the driving period and t accounts for dynamics that take place on longer time scales. Because this thesis focuses on quantum mechanical systems, we will restrict ourselves to those linear systems that yield a unitary time evolution.

3.2.1. Schrödinger equation

The Schrödinger equation is a linear equation of motion that yields a unitary time-evolution, stemming from a Hermitian Hamilton operator. In its most general form it reads

$$\mathrm{i}\frac{d}{dt}\,|\psi(t)\rangle = H(t)\,|\psi(t)\rangle \,, \tag{3.11}$$

where we have set $\hbar = 1$, and $H(t)$ is the underlying Hamilton operator, which is assumed to be T-periodic, i.e. $H(t+T) = H(t)$. The underlying Hilbert space $\mathcal{R}$ has an arbitrary dimension. In order to make the dynamics of the system fully determined one has to fix the initial state, which will be denoted by $|\psi_0\rangle$.

According to Section 3.1, the tt'-version of the T-periodic Schrödinger equation (3.11)

reads

$$\begin{aligned} i\partial_t \left|\tilde{\psi}(t',t)\right\rangle &= H(t') \left|\tilde{\psi}(t',t)\right\rangle - i\partial_{t'} \left|\tilde{\psi}(t',t)\right\rangle \\ &= \mathcal{H}(t') \left|\tilde{\psi}(t',t)\right\rangle , \end{aligned} \tag{3.12}$$

where the so called generalized Floquet operator $\mathcal{H}$ [GH98] was introduced

$$\mathcal{H}(t') \equiv H(t') - \mathrm{i}\partial_{t'}. \tag{3.13}$$

Sambe proposed an extension of Hilbert space [Sam73], such that t' is treated formally as a (pseudo spatial) canonical coordinate, i.e. as an additional configuration-space parameter. The resulting Sambe space is a Hilbert space which is given by the tensor product $\mathcal{H} \otimes \mathcal{T}$ of the Hilbert space $\mathcal{R}$ of the original system and the Hilbert space $\mathcal{T}$ of T-periodic functions. Accordingly, the state $|\tilde{\psi}(t')\rangle$ can be regarded as a partial projection on the *localized* state $|t'\rangle$, i.e.

$$|\tilde{\psi}(t')\rangle = \langle t'|\tilde{\psi}\rangle\!\rangle. \tag{3.14}$$

The notation on the right hand side emphasizes that the state $|\tilde{\psi}\rangle\!\rangle$ lives in a different Hilbert space than $|\tilde{\psi}(t')\rangle$. This notation is also used in other works [GH98].

Due to the periodicity of $|\tilde{\psi}(t')\rangle$ in t', a suitable representation of the t'-dependence is given by the Fourier sum

$$|\tilde{\psi}(t')\rangle = \sum_{m=-\infty}^{\infty} e^{\mathrm{i}m\omega t'} \left|\tilde{\psi}_m\right\rangle , \tag{3.15a}$$

$$\text{with } \left|\tilde{\psi}_m\right\rangle \equiv \frac{1}{T}\int_0^T dt' e^{-\mathrm{i}m\omega t'} \left|\tilde{\psi}(t')\right\rangle . \tag{3.15b}$$

With the convention, used here, the extended states are normalized to T, i.e.

$$\langle\!\langle\tilde{\psi}|\tilde{\psi}\rangle\!\rangle = \int_0^T dt' \left\langle\tilde{\psi}(t')|\tilde{\psi}(t')\right\rangle = T , \tag{3.16}$$

instead of being normalized to unity. This convention is connected to the prescription for recovering the physically relevant state [cf. Eq. (3.9)], which is given by

$$|\psi(t)\rangle = \left|\tilde{\psi}(t',t)\right\rangle\Big|_{t'=t} . \tag{3.17}$$

These concepts can be extended to non-periodic systems, e.g. by considering the dynamics during a single period [MCL95].

The obvious disadvantages, related to an increase of the dimension of configuration-space by one and the directly implied increase of the Hilbert space, are opposed by the advantage that methods from time-independent scattering theory can be applied, although the Hamiltonian is time dependent [MCL95].

3.2.2. Floquet states

Eq. (3.12) has the form of a Schrödinger equation with a static Hamiltonian $\mathcal{H}$. The auxiliary parameter t' behaves as an additional configuration-space parameter with the only peculiarity that its kinetic term is diffusive (first order) instead of dispersive (second order). As a consequence, the Hamiltonian $\mathcal{H}$ is not bounded from below, which is

unproblematic for initial-value problems[2].

The most standard approach to the Schrödinger equation with a static underlying Hamiltonian, is to calculate the eigenstates and eigenvalues of the Hamilton operator. The eigenvalue equation for $\mathcal{H}$ reads

$$\mathcal{H}\,|\nu,n\rangle\!\rangle = \varepsilon_{\nu,n}\,|\nu,n\rangle\!\rangle. \tag{3.18}$$

The eigenstates $|\nu,n\rangle\!\rangle$ are called Floquet states of $\mathcal{H}$ and the eigenvalues $\varepsilon_{\nu,n}$ are called quasienergies of $|\nu,n\rangle\!\rangle$.

The quasienergies and eigenstates are labeled with two quantum numbers because the quasienergies come in classes $\varepsilon_{\nu,n} = \varepsilon_{\nu,0} + n\omega$, with $n \in \mathbb{Z}$ and the cardinality of the index set for ν is the dimension of $\mathcal{R}$. Each shifted quasienergy corresponds to a physically equivalent solution, given by $\langle t'|\nu,n\rangle\!\rangle = \exp(\mathrm{i}m\omega t)\,\langle t'|\nu,0\rangle\!\rangle$. Therefore, the entire spectrum can be folded back into the interval $-\omega/2 \leq \varepsilon \leq \omega/2$, in complete analogy to the Brillouin zone in spatially periodic systems.

Given all eigenstates and eigenvalues of $\mathcal{H}$, the solution to the Schrödinger equation (3.12) with initial state $|\tilde{\psi}_0\rangle\!\rangle$ can be expressed as[3]

$$|\tilde{\psi}(t)\rangle\!\rangle = \sum_{\nu,n} \exp[-\mathrm{i}\varepsilon_{\nu,n}t]A_{\nu,n}\,|\nu,n\rangle\!\rangle, \text{ with } A_{\nu,n} = \langle\!\langle \nu,n|\tilde{\psi}_0\rangle\!\rangle\,, \tag{3.19}$$

where normalized eigenstates, $\langle\!\langle \nu,n|\nu,n\rangle\!\rangle = 1$, are assumed.

According to the prescription (3.17), the physically meaningful solution contained in Eq. (3.19) reads

$$|\psi(t)\rangle = \sum_{\nu} e^{-\mathrm{i}\varepsilon_\nu t} A_\nu\,|\phi_\nu(t)\rangle\,, \tag{3.20a}$$

$$\text{with } A_\nu \equiv \sum_n A_{\nu,n} = \langle\phi_\nu(0)|\psi_0\rangle\,, \tag{3.20b}$$

where the notations $|\phi_\nu(t')\rangle \equiv \langle t'|\nu\rangle\!\rangle$, and $\varepsilon_\nu \equiv \varepsilon_{\nu,n}$ have been used. Eq. (3.20a) is one of the central equations in Floquet theory. It shows that the physical solution to a time-periodic quantum system can be expressed as a superposition of time-periodic Floquet states, which are multiplied with a time-dependent phase factor whose time dependence is incommensurate with the driving frequency. Note that Eqs. (3.20) only involve a single time, what means that we have left the tt'-framework.

According to Eq. (3.20a), the time-evolution of a single Floquet state (e.g. $A_\nu = \delta_{\nu 0}$) is given by

$$|\psi_\nu(t)\rangle = e^{-\mathrm{i}\varepsilon_\nu t}\,|\phi_\nu(t)\rangle\,. \tag{3.21}$$

This is the time-like analogy to Bloch states, i.e. the eigenstates of a spatially periodic Hamiltonian, which can be factorized in a spatially periodic wave function and a plane wave whose wave length is larger than the underlying lattice constant.

3.2.3. Generalized view on Floquet quasienergy

In literature, quasienergies are usually assigned to the Floquet states only. In fact, this concept can be extended to any state. For states that live in Sambe space, $\mathcal{R}\otimes\mathcal{T}$, one

[2] Unbounded Hamiltonians are problematic, e.g. when it comes to the consideration of thermal ensembles.

[3] Sums over n and ν are to be understood to run over all possible values.

can define a total quasienergy $\mathcal{E}$ as

$$\frac{\langle\langle\tilde{\psi}(t)|\mathcal{H}|\tilde{\psi}(t)\rangle\rangle}{\langle\langle\tilde{\psi}|\tilde{\psi}\rangle\rangle} = \mathcal{E}, \tag{3.22}$$

which is a conserved quantity. This conservation holds also for nonlinear systems, which will be discussed in Section 3.3.

The definition (3.22) refers explicitly to states that are considered within the tt'-formalism. It is possible to define a total quasienergy, also for the physically relevant states that live in the original Hilbert space $\mathcal{R}$ via the expansion (3.20a). Accordingly, the (conserved) total quasienergy of $|\psi(t)\rangle$, is given by $\mathcal{E} = \sum_\nu |A_\nu|^2\varepsilon_\nu$, where A_ν is the expansion coefficient with respect to the Floquet states – see Eqs. (3.20). In any case, for periodically driven linear systems, a rather unconventional "conservation law" is given by

$$\langle\psi(t+T)|\psi(t)\rangle = \sum_\nu |A_\nu|^2 e^{\mathrm{i}\varepsilon_\nu T} = \text{const.}. \tag{3.23}$$

This conservation law does not require to calculate the Floquet states and can be used for consistency and convergence checks in numerical solutions of a driven linear system.

3.3. Nonlinear Schrödinger equation

The GP equation, is an efficient approximation for weakly interacting ultracold Bose gases [DGPS99, Leg01]. It describes the condensate wave function on a mean-field level. This means that the interaction of the particles among each other is modeled by an effective *external* potential, which depends itself on the particle density. Therefore, GP is considered a mean-field approximation. The resulting mathematical description is that of a single particle with a self-interaction term. Accordingly, within GP, one cannot describe the motion of particles out of the condensate. The GP equation for spinless particles reads

$$i\partial_t\psi(\mathbf{x},t) = H_0(\mathbf{x},t)\psi(\mathbf{x},t) + g|\psi(\mathbf{x},t)|^2\psi(\mathbf{x},t), \tag{3.24}$$

where $H_0(\mathbf{x},t) = V(\mathbf{x},t) - \frac{1}{2}\partial_{\mathbf{x}}^2$ is the operator associated with the linear part of this equation. The wave function ψ shall be normalized as

$$\int d\mathbf{x}\,|\psi(\mathbf{x})|^2 = 1, \tag{3.25}$$

which can be shown to be conserved under equation of motion (3.24).

Equation (3.24) is dimensionless. This can be realized by the choice of an appropriate length scale x_0 and then express all lengths, energies, frequencies, and times in units of x_0, $\hbar^2/Mx_0^2$, $\hbar/Mx_0^2$, and $Mx_0^2/\hbar$ respectively; where M is the atom mass. These natural units will also be used in Section 3.4.2. Furthermore, we set $\hbar = 1$, such that energies and frequencies have the same dimension.

Interactions among the particles enter with the latter, nonlinear, part in Eq. (3.24). Its strength is controlled via the prefactor g, which is proportional to the s-wave scattering length a and the total particle number[4] N and depends on the trap geometry if some degrees of freedom are effectively frozen out. The GP equation is sometimes called

[4]Strictly speaking $g \propto (N-1)$, but since N is supposed to be of the order of several thousand particles or more, the relative difference between N and $N-1$ becomes vanishingly small. In numerical simulations on the other hand, one often describes rather a handful of particles. In this case the relative error becomes large when a full many-body simulation is compared to the mean-field limit and one has to use $(N-1)$.

nonlinear Schrödinger equation, since for $g = 0$, the standard Schrödinger equation is obtained. We consider the single particle part to be time periodic, with period T: $H_0(\mathbf{x}, t+T) = H_0(\mathbf{x}, t)$.

In this case the phase space is the Hilbert space $L_2(\mathbb{C})$ of square integrable complex-valued wave functions. Applying the recipe from the previous section, we obtain the nonlinear Schrödinger equation within the tt'-formalism:

$$i\partial_t \psi(\mathbf{x}, t'; t) = (H_0(\mathbf{x}, t') - i\partial_{t'})\psi(\mathbf{x}, t'; t) + g|\psi(\mathbf{x}, t'; t)|^2 \psi(\mathbf{x}, t'; t), \tag{3.26}$$

with the normalization

$$\int d\mathbf{x} dt \; |\psi(\mathbf{x}, t'; t)|^2 = T. \tag{3.27}$$

This normalization is a direct consequence of the fact that the physically relevant wave function is obtained as $\psi(\mathbf{x}, t) = \psi(\mathbf{x}, t, t)$.

Equation (3.26) has the form of a GP equation, with the linear part being static, and the related wave function lives in the extended space $\mathcal{R} \otimes \mathcal{T}$. This implies that Eq. (3.26) can be derived from the Hamiltonian

$$H'_{\mathrm{GP}} = \int d\mathbf{x}\, dt' \; \psi^* \mathcal{H}_0(\mathbf{x}, t')\psi + \frac{g}{2}|\psi(\mathbf{x}, t')|^4, \tag{3.28}$$

with $\mathcal{H}_0(\mathbf{x}, t') \equiv H_0(\mathbf{x}, t') - i\partial_{t'}$. In full analogy to linear systems, the parameter t' takes on the role of an additional configuration-space parameter, similar to the spatial coordinates contained in $\mathbf{x}$. This interpretation of t' fails, when the tt'-formalism is applied to the equation of motion of field operators in Heisenberg picture, as will be discussed in Section 3.4.2

3.3.1. Nonlinear Floquet states

The minima of the Hamiltonian (3.28) are stationary states of the equation of motion (3.26). The physically relevant solutions that correspond to stationary solutions within the tt'-formalism are T-periodic states except for a global phase factor and are named nonlinear Floquet states [Hol01, MMF08]. It was shown that, in some cases, the nonlinear Floquet states serve as a good minimal basis to describe the dynamics of an ac-driven BEC [Hol01, MMF08, WDWD12]. Here, the extended tt'-formalism can be used to derive a determining equation for nonlinear Floquet states. By applying the variational principle to equation (3.28), one obtains

$$\varepsilon\psi(\mathbf{x}, t') = \left(\mathcal{H}_0(\mathbf{x}, t') + g|\psi|^2\right)\psi(\mathbf{x}, t'), \tag{3.29}$$

where ε is the nonlinear analog of the quasienergy, known from the linear case. That is, a solution of Eq. (3.29) accumulates an overall phase of $e^{-i\varepsilon T}$ after one driving period, but turns back to its original state (except for the overall phase). This equation has been previously introduced in Ref. [WDWD12], but was not brought into the context with the (extended) tt'-formalism.

3.4. Periodic driving in the Heisenberg picture

3.4.1. General considerations

An interesting question to ask is, whether the concepts from linear systems, cf. Section 3.2, can still be applied when we change from the Schrödinger picture to the

Heisenberg picture. The answer to this question is "it depends". In order to give a more precise answer, we will have a closer look at the Heisenberg picture.

In the Heisenberg picture, the dynamics is *attached* to the operators acting on Hilbert space. This means that when it comes to the calculation of expectation values of an operator A over time, it can be expressed in two formally different manners:

$$\text{Schrödinger picture: } \langle A\rangle(t) = \langle\psi(t)|A|\psi(t)\rangle\,, \tag{3.30a}$$

$$\text{Heisenberg picture: } \langle A\rangle(t) = \langle\psi_0|A^{\mathrm{H}}(t)|\psi_0\rangle\,, \tag{3.30b}$$

$$\text{with } A^{\mathrm{H}}(t) \equiv U^\dagger(t,0)AU(t,0). \tag{3.30c}$$

Here, ψ_0 is the initial state, and $U(t,0)$ is the unitary time-evolution operator, which maps a given initial state to the state that is reached at time t, i.e. $|\psi(t)\rangle = U(t,0)\,|\psi_0\rangle$. Inserting this identity in the expression for $\langle A\rangle(t)$ in the Schrödinger picture makes the equivalence between both pictures of motion evident. Note that the definition (3.30c) refers to systems with both, time-dependent and time-independent Hamiltonians, and that at $t = 0$, both pictures are equivalent, i.e. $A^{\mathrm{H}}(0) = A$.

The equation of motion for operators in the Heisenberg picture can be derived via the equation of motion for the unitary time-evolution operators, given by

$$\mathrm{i}\frac{d}{dt}U(t) = H(t)U(t) \text{ and } -\mathrm{i}\frac{d}{dt}U(t)^\dagger = U(t)^\dagger H(t), \tag{3.31}$$

where the initial time $t_0 = 0$ as argument has been omitted. From this follows directly the Heisenberg equation of motion for an operator A:

$$\mathrm{i}\frac{d}{dt}A^{\mathrm{H}}(t) = \mathrm{i}\frac{d}{dt}\left(U^\dagger AU\right) = \mathrm{i}(-U^\dagger HAU + U^\dagger AHU) \tag{3.32a}$$

$$\Leftrightarrow \quad \mathrm{i}\frac{d}{dt}A^{\mathrm{H}}(t) = \left[A^{\mathrm{H}}(t), H^{\mathrm{H}}(t)\right]. \tag{3.32b}$$

The latter equation is obtained by the insertion of identity operators expressed as $U^\dagger U$ between the operators H and A in Eq. (3.32a). It is important to note that in the Heisenberg equation of motion (3.32b), the Hamilton operator is given in Heisenberg picture. Only for the case of a time-independent Hamiltonian, the Hamiltonian in the Heisenberg picture coincides with its counterpart in the Schrödinger picture, i.e.

$$\frac{d}{dt}H = 0 \;\Rightarrow\; H^{\mathrm{H}} = H. \tag{3.33}$$

In the Heisenberg picture, the initial preparation $|\psi_0\rangle$ of the system only enters, when expectation values are calculated. This means that with this framework one can formally solve the dynamics without fixing the initial state. To be precise, in the Heisenberg picture the initial conditions refer to the initial *meaning* or action of the operators. An example would be the time evolution of the momentum operator $p^{\mathrm{H}}(t)$ in Heisenberg picture, which for finite times t is in general not the momentum operator any more, although one tends to speaks about the time-evolution of the momentum operator.

Mapping an operator, which is given in the Schrödinger picture, to its counterpart in the Heisenberg picture is a homomorphism for

$$\text{addition: } (A+B)^{\mathrm{H}} = A^{\mathrm{H}} + B^{\mathrm{H}}, \tag{3.34a}$$

$$\text{and multiplication: } (AB)^{\mathrm{H}} = A^{\mathrm{H}}B^{\mathrm{H}}. \tag{3.34b}$$

From this follows directly that this mapping preserves (anti-) commutation relations

Box 3.4.1 | Matrix generators

Quadratic matrices can be expressed in two qualitatively different manners: (*i*) via a linear basis, e.g. component wise, or (*ii*) using generators of the space of quadratic matrices. Let us take, for example, the space of complex 2×2-matrices. A linear basis of this space is given by the identity matrix $\sigma_0 = \mathbb{1}$, together with the Pauli matrices

$$\sigma_1 = \begin{pmatrix} 0 & 1 \\ 1 & 0 \end{pmatrix}, \quad \sigma_2 = \begin{pmatrix} 0 & -\mathrm{i} \\ \mathrm{i} & 0 \end{pmatrix},$$
$$\text{and } \sigma_3 = \begin{pmatrix} 1 & 0 \\ 0 & -1 \end{pmatrix}.$$

This means that a given 2×2-matrix $\mathcal{M}$ can be expressed as a linear combination the of the four matrices σ_i. However, if one allows also matrix multiplication for the representation of $\mathcal{M}$, only two Pauli matrices are needed. Let us take for example σ_1 and σ_2. The identity matrix can be obtained as

$$\sigma_i^2 = \mathbb{1}, \text{ for } i = 1, 2.$$

And the third Pauli matrix is given by the commutator

$$\tfrac{1}{2\mathrm{i}}[\sigma_1, \sigma_2] = \sigma_3.$$

As a result, the linear basis $\{\sigma_0, \ldots, \sigma_3\}$ can be obtained from the first two Pauli matrices, using matrix multiplication and addition. Consequently, any given matrix $\mathcal{M}$ can be expressed as a polynomial in σ_1 and σ_2. The matrices σ_1 and σ_2 can be called *generators* of the algebra of complex 2×2 matrices [AM69]. Similarly, the space of 4×4-matrices is generated by the four gamma matrices γ^ν from Dirac theory, and the operators acting on bosonic or fermionic Fock space is generated by the annihilation and creation operators. See Appendix B for a proof.

between operators.

Unfortunately, the Heisenberg picture does not preserve time periodicity of a Hamiltonian. That is, if in the Schrödinger picture the equation $H(t+T) = H(t)$ holds, it does, in general, not hold in the Heisenberg picture, i.e. $H^{\mathrm{H}}(t+T) \neq H^{\mathrm{H}}(t)$. This is due to the fact that the time-evolution operator $U(t)$, which enters in the definition of the Heisenberg picture, involves the phases $\exp(-\mathrm{i}\varepsilon_\nu t)$, which are in general incommensurate with the driving frequency. A trivial exception is the case of a static Hamiltonian, which is identical in the Schrödinger picture and the Heisenberg picture.

In principle, this broken time-periodicity in the Heisenberg picture, forbids the use of Floquet theory or the tt'-formalism in this picture of motion. Fortunately, in many cases, there is a way around this problem by expressing the Hamilton operator in terms of a set of operators that generates all others via a linear combination and matrix multiplication. The price for this circumvention is that the resulting equation of motion, when it is expressed with these generators, is not linear any more, although the starting point, the Heisenberg equation of motion, is linear. An example of such a set are the field operators from the formalism of second quantization, which will be discussed in the following section.

3.4.2. Field operators in Heisenberg picture

We consider a system with only one species of indistinguishable particles whose interaction is given by the potential $w(\mathbf{x})$. The Hamilton operator of this system can be

expressed via the field operators of second quantization

$$\hat{H}(t) = \int d^3\mathbf{x}\, \hat{\psi}^\dagger(\mathbf{x}) H_0(\mathbf{x},t)\hat{\psi}(\mathbf{x}) + \iint d^3\mathbf{x}\, d^3\mathbf{y}\, \hat{\psi}^\dagger(\mathbf{x})\hat{\psi}^\dagger(\mathbf{y}) w(\mathbf{x}-\mathbf{y})\hat{\psi}(\mathbf{x})\hat{\psi}(\mathbf{y}), \quad (3.35)$$

where $H_0(\mathbf{x},t) = V(\mathbf{x},t) - \frac{1}{2}\partial_{\mathbf{x}}^2$ determines the single-particle part of the Hamiltonian. Here, we assume the single-particle part $H_0(\mathbf{x},t) = H_0(\mathbf{x},t+T)$ to be time dependent. The operators $\hat{\psi}^\dagger(\mathbf{x})$ and $\hat{\psi}(\mathbf{x})$ are the field operators and satisfy bosonic or fermionic (anti-) commutation relations, according to whether the underlying many-particle system consists on bosons or fermions. That means

$$\left[\hat{\psi}(\mathbf{x}), \hat{\psi}^\dagger(\mathbf{y})\right]_{-\zeta} = \delta(\mathbf{x}-\mathbf{y}), \quad (3.36a)$$

$$\text{and } \left[\hat{\psi}(\mathbf{x}), \hat{\psi}(\mathbf{y})\right]_{-\zeta} = \left[\hat{\psi}^\dagger(\mathbf{x}), \hat{\psi}^\dagger(\mathbf{y})\right]_{-\zeta} = 0, \quad (3.36b)$$

with $\zeta = +1\,(-1)$ for bosons (fermions) and $[\cdot,\cdot]_{-1}$ denotes the commutator of two operators and $[\cdot,\cdot]_{+1}$ their anti-commutator. The expression refers to a commutator, if the index $-\zeta$ is omitted. Their action is the creation $[\hat{\psi}^\dagger(\mathbf{x})]$ or annihilation $[\hat{\psi}(\mathbf{x})]$ of a localized particle at point $\mathbf{x}$. The space, which they act on is the Hilbert space, given by a direct sum of all N-particle Hilbert spaces and is known as Fock space.

Mapping the Hamiltonian (3.35) to the Heisenberg picture, can be realized by mapping the field operators, which are used to express the Hamiltonian, to the Heisenberg picture. The Heisenberg equation of motion for the field operators then reads [5]

$$\begin{aligned} \mathrm{i}\frac{\partial}{\partial t}\hat{\psi}(\mathbf{x},t) &= [\hat{\psi}(\mathbf{x},t), \hat{H}^{\mathrm{H}}(t)] \\ &= H_0(\mathbf{x},t)\hat{\psi}(\mathbf{x},t) + \int d^3\mathbf{y}\, \hat{\psi}^\dagger(\mathbf{y},t) w(\mathbf{y}-\mathbf{x})\hat{\psi}(\mathbf{y},t)\hat{\psi}(\mathbf{x},t). \end{aligned} \quad (3.37)$$

Note that for any finite time $t > 0$ the action of $\hat{\psi}^\dagger(\mathbf{x},t)$ and $\hat{\psi}(\mathbf{x},t)$ is not any more a simple creation or annihilation of localized particles. The time evolution of the field operators suffices to obtain the time evolution of any other operator on Fock space, because the field operators generate the space of operators acting on Fock space, cf. Box 3.4.1 and Appendix B.

If H_0 is time periodic, then so is the equation of motion for the field operators (3.37). This observation contradicts the main message of Section 3.4.1, where it was argued that mapping to Heisenberg picture does not preserve the time periodicity of the Hamiltonian in the Schrödinger picture. The fact that Eq. (3.37) is time periodic nevertheless, has to do with the used representation of the Hamiltonian $\hat{H}^{\mathrm{H}}$: For the equation of motion of the field operators, we chose to represent the Hamiltonian $\hat{H}^{\mathrm{H}}$ via the field operators themselves, which in turn form a nonlinear basis (generators) of the space of operators – cf. Appendix B. This choice is not necessary, but extremely convenient. Main consequences are preservation of time periodicity in Heisenberg picture and that the resulting equation of motion is nonlinear in the fields.

Before we transfer the equation of motion (3.37) for field operators to the tt'-formalism we need to do some preliminary considerations about the underlying phase space. Unfortunately, Eq. (3.37) is not a closed equation of motion for the field operator at space point $\mathbf{x}$, because the integral in the interaction term is, in principle, performed over the entire space. Even for contact interaction ($w(\mathbf{x}) = \delta(\mathbf{x})$), Eq. (3.37) is not closed for a fixed space point $\mathbf{x}$, due to the spatial derivative contained in $H_0(\mathbf{x},t)$. In order to

[5] In agreement with the conventions in literature, we will simply write $\hat{\psi}(\mathbf{x},t)$ instead of $\hat{\psi}(\mathbf{x})^{\mathrm{H}}(t)$.

solve Eq. (3.37) it is necessary to solve it for all points $\mathbf{x} \in \mathbb{R}^3$ simultaneously. In other words, one has to solve Eq. (3.37) for the indexed family of operators $\hat{\Psi} \coloneqq \{\hat{\psi}(\mathbf{x})\}_{\mathbf{x}\in\mathbb{R}^3}$. Consequently, the phase space of this system is the space of operator-valued functions on $\mathbb{R}^3$. This way, Eq. (3.37) becomes a closed system and the extended tt'-formalism is applicable. For the sake of simplicity, we will not use the family of operators, but do our considerations by referring to each "component" of $\hat{\Psi}$, which is simply $\hat{\psi}(\mathbf{x})$.

Analogously to the case of square integrable wave functions, the generalized loops for the tt'-formalism are given by operator-valued functions $\hat{\psi}(\mathbf{x}, t'; t)$ with an additional parameter.

We can directly construct an equation of motion from Eq. (3.37) which is of the form given in Eq. (3.4):

$$\mathrm{i}\frac{\partial}{\partial t}\hat{\psi}(\mathbf{x}, t'; t) = H(\mathbf{x}, t')\hat{\psi}(\mathbf{x}, t'; t) - \mathrm{i}\frac{\partial}{\partial t'}\hat{\psi}(\mathbf{x}, t'; t) + \int d^3\mathbf{y}\ \hat{\psi}^\dagger(\mathbf{y}, t'; t)w(\mathbf{y}-\mathbf{x})\hat{\psi}(\mathbf{y}, t'; t)\hat{\psi}(\mathbf{x}, t'; t). \tag{3.38}$$

From Section 3.1.1, we know that, for standard initial conditions, $\hat{\psi}(\mathbf{x}, t'; t)$ is a solution of the Heisenberg equation of motion that is obtained from Eq. (3.37) by replacing $H_0(\mathbf{x}, t)$ with $H_0(\mathbf{x}, t+\tau)$, with

$$\tau = (t' - t)\mathrm{mod}T. \tag{3.39}$$

This means that the field operators satisfy the "equal-time" commutation relations

$$\left[\hat{\psi}(\mathbf{x}, t'; t), \hat{\psi}^\dagger(\mathbf{y}, t'; t)\right]_{-\zeta} = \delta(\mathbf{x}-\mathbf{y}), \tag{3.40a}$$

$$\text{and } \left[\hat{\psi}(\mathbf{x}, t'; t), \hat{\psi}(\mathbf{y}, t'; t)\right]_{-\zeta} = \left[\hat{\psi}^\dagger(\mathbf{x}, t'; t), \hat{\psi}^\dagger(\mathbf{y}, t'; t)\right]_{-\zeta} = 0, \tag{3.40b}$$

for all t and t'. Note that both times t' and t have to coincide. These commutation relations show that the interpretation of t' as additional (space-like) configuration-space parameter does not hold in all regards. If t' *behaved* like a spatial coordinate, it would appear within the Dirac delta on the right-hand side of equation (3.40a).

Analogously to first quantization, it is often convenient to approach the solution of the Heisenberg equation in another basis. So, instead of considering operators that create (annihilate) particles at a localized space point, we are interested in operators that create (annihilate) particles in a delocalized orbital, e.g. a plane wave. For most purposes it is convenient to choose the set of single-particle eigenstates $\phi_\ell(\mathbf{x})$ of $H_0(\mathbf{x}, 0^-)$ before[6] the driving is switched on.

In order to map also the t'-dependence to a discrete basis, we Fourier transform with respect to that parameter in the same step, i.e.

$$\hat{a}_{\ell m}(t) = \frac{1}{T}\int dt' d^3\mathbf{x}\ e^{\mathrm{i}m\omega t'}\phi^*_\ell(\mathbf{x})\hat{\psi}(\mathbf{x}, t'; t) \tag{3.41a}$$

$$\text{and } \hat{\psi}(\mathbf{x}, t'; t) = \sum_{m\in\mathbb{Z}}\sum_\ell e^{-\mathrm{i}m\omega t'}\phi_\ell(\mathbf{x})\hat{a}_{\ell m}(t). \tag{3.41b}$$

In the new representation, the commutation relations transform to

[6] The superscript in the time argument of H_0 indicates that if the driving is switched on suddenly with a step function at time $t = 0$, one has to take the value before this time point of switching.

Box 3.4.2 | Calculus for Heisenberg operators in t,t′-formalism

Although the extension of the tt'-formalism, as it is introduced in Section 3.4.2, deals explicitly with operators of second quantization, a big part of the needed calculus applies to arbitrary loops [in the sense of Eq. (3.3)] of operators that act on a Hilbert space. The Fourier transform of an operator loop $\tilde{A}$ is given by:

$$\tilde{A}_m = \frac{1}{T}\int_0^T dt' \tilde{A}(t') e^{\mathrm{i}\omega m t'}. \tag{3.42}$$

The Fourier transform of the product of two loops, then reads

$$\left(\tilde{A}\tilde{B}\right)_m = \sum_{m'} \tilde{A}_{m-m'}\tilde{B}_{m'} \ . \tag{3.43}$$

This yields the following expression for the Fourier components of the (anti-) commutator of $\tilde{A}$ and $\tilde{B}$

$$\left[\tilde{A},\tilde{B}\right]_{-\zeta}\Big|_m = \sum_{m'}\left[\tilde{A}_{m-m'},\tilde{B}_{m'}\right]_{-\zeta}. \tag{3.44}$$

The Hermitian adjoint of an operator loop is given by

$$\tilde{A}^\dagger|_{t'} := \tilde{A}|_{t'}{}^\dagger \ . \tag{3.45}$$

Inserting Eq. (3.41b) in this identity, we obtain

$$\tilde{A}(t')^\dagger = \sum_m e^{\mathrm{i}m\omega t'}(\tilde{A}_m)^\dagger \ , \tag{3.46}$$

which implies the relation

$$(\tilde{A}_m)^\dagger = (\tilde{A}^\dagger)_{-m} \ . \tag{3.47}$$

Hence, Fourier transformation and Hermitian adjunction do not commute. In order to avoid confusion, we introduce the definition

$$\tilde{A}^\dagger_m := (\tilde{A}_m)^\dagger = (\tilde{A}^\dagger)_{-m} \ . \tag{3.48}$$

$$\sum_{m'}\left[\hat{a}_{\ell,m+m'}(t),\hat{a}^\dagger_{\ell'm'}(t)\right]_{-\zeta} = \delta_{\ell\ell'}\delta_{m0}, \tag{3.49a}$$

$$\sum_{m'}\left[\hat{a}_{\ell,m'-m},\hat{a}_{\ell'm'}\right]_{-\zeta} = 0, \text{ and} \tag{3.49b}$$

$$\sum_{m'}\left[\hat{a}^\dagger_{\ell,m'-m},\hat{a}^\dagger_{\ell'm'}\right]_{-\zeta} = 0, \text{ for all } \ell,\ell',m. \tag{3.49c}$$

The definition of the adjoint of $\hat{a}_{\ell m}$ is given in Box 3.4.2. Implementing these transformations in Eq. (3.38) yields the equation of motion for $\hat{a}_{\ell m}(t)$, which reads

$$\begin{aligned} i\tfrac{\partial}{\partial t}\hat{a}_{\ell m}(t) = &\sum_{\ell' m'}\left(H_{\ell m,\ell' m'} - \delta_{mm'}\delta_{\ell\ell'}\omega m\right)\hat{a}_{\ell' m'}(t) \\ &+ \lambda \sum_{\substack{\ell_1\ell_2\ell_3\\ m_1m_2m_3}} \delta_{m+m_1,m_2+m_3} w_{\ell\,\ell_1,\ell_2\ell_3}\ \hat{a}^\dagger_{\ell_1 m_1}(t)\hat{a}_{\ell_2 m_2}(t)\hat{a}_{\ell_3,m_3}(t). \end{aligned} \tag{3.50}$$

The matrix elements of the single particle part of the Hamiltonian are diagonal in ℓ for the undriven case. The time-like part of the interaction is contact like and is independent of the spatial part whose two-body matrix elements $w_{\ell_1\ell_2,\ell_3\ell_4}$ are given by

$$w_{\ell_1\ell_2,\ell_3\ell_4} := \int d^3\mathbf{x}\, d^3\mathbf{y}\ \phi^*_{\ell_1}(\mathbf{x})\phi^*_{\ell_2}(\mathbf{y})w(\mathbf{x}-\mathbf{y})\phi_{\ell_3}(\mathbf{y})\phi_{\ell_4}(\mathbf{x}). \tag{3.51}$$

The presented results refer explicitly to three dimensional systems. They are obtained

for lower dimensions, simply by making the trapping potential highly anisotropic, and thus freezing out other degrees of freedom.

Conclusions

In this chapter, an extended version of the tt'-formalism, which allows for the treatment of nonlinear equations of motion, was introduced. In previous works, where this formalism was introduced for linear systems, the linearity of the underlying equation of motion was used explicitly. We have seen that the concepts of this extension can be illustrated by a geometric interpretation – cf. Fig. 3.1. Three examples have been presented. For the case of square integrable wave functions, the additional parameter t' can be regarded as an additional configuration-space parameter. This interpretation fails when this formalism is applied to field operators in the Heisenberg picture. So far, we have not yet seen how the tt'-formalism is actually useful for the study of time-periodic systems. This will be the objective of the next chapter.

4. Orbital Josephson effect in driven BECs

The Josephson effect [Jos62] is a fundamental macroscopic quantum phenomenon. It can occur in a system that features a macroscopic wave function formed by the coherent occupation of two or a few single-particle modes. This concept is illustrated in Fig. 4.1, in which the two modes are spatially separated parts of a wave function, and the coupling between these modes is induced by the potential barrier which allows particle transitions via tunneling.

The original version of the Josephson effect refers to superconductors, where it was observed [AR63, Sha63] only one year after its prediction. Since then it has been realized in further experimental setups, such as superfluid Helium [AV85], and most recently in BECs [AGF+05, HMWC98, ZNGO10]. A Josephson junction in BECs can be realized in three qualitatively different ways, which one may refer to as (*i*) external [AGF+05], (*ii*) internal [HMWC98, ZNGO10], and (*iii*) orbital Josephson effect (OJE). The difference between the listed types lies in the characteristics of the participating modes. The modes in an external Josephson system are localized Wannier functions in a double-well potential. Such a setup is represented in Fig. 4.1. In an internal Josephson junction the modes refer to different electronic configurations of the gas atoms, usually given by two hyperfine states. In an OJE the modes are wave functions, whose density may overlap strongly, see Fig. 4.2a. The terms *internal* and *external* Josephson effect are quite standard in the literature, as opposed to the *orbital* Josephson effect, which has recently been proposed as part of this thesis[1].

4.1. The Josephson effect in BECs

For noninteracting particles, the dynamics of a bosonic two-level system is merely an amplification of the dynamics undergone by a single atom [HMWC98, Sol99]. In order to observe truly collective behavior particle interactions are required [Sol99, ZSL98]. In this work, a system is considered to be a bosonic Josephson junction (BJJ) when it can effectively be described by the two-level Hamiltonian

$$\hat{H}_{2\mathrm{L}} = J a_1^\dagger a_2 + J^* a_2^\dagger a_1 + \mu(\hat{n}_1 - \hat{n}_2) + \frac{\lambda}{2} \sum_{\nu=1,2} \hat{n}_\nu(\hat{n}_\nu - 1), \tag{4.1}$$

where the single particle part is left as general as possible, and the interaction term is such that particles only interact with each other when they reside in the same mode. This Hamiltonian is the same for all types of BJJs listed above.

[1] A specific setup for the realization of an OJE has been published as part of this thesis in Ref. [HCCS12]. A more general presentation of this concept, discussed in this chapter, will be published [HHC+].

Figure 4.1: *Semi-heuristic representation of a Josephson System.*

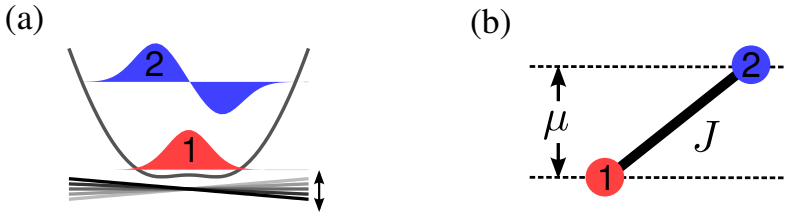

Figure 4.2.: *Schematic illustration of an orbital Josephson junction.* A one-dimensional setup is used for illustrative purposes. (a) The driving potential, indicated by the green lines, couples the initial state $|1\rangle$ with an excited state $|2\rangle$. (b) The resulting dynamics is that of a bosonic Josephson junction, cf. Eq. (4.1).

BJJs can be used for high precision measurement, e.g., on temperature [GHF+06], weak forces [BnS12, CMZ99], or chemical potential differences [KS03]. Furthermore, they serve as an outstanding basis to perform tomography of a quantum many-body state [Zib12].

4.2. Generic setup of an OJE

In the following a recipe for the realization of an orbital Josephson junction in a very general setup is presented. However, in Chapter 6 we will see that a variety of orbital Josephson junctions exists which cannot be considered a specific realization of the type presented here.

We consider a static BEC, trapped in an arbitrary geometry, given by a static external potential $V_{\text{trap}}(\mathbf{x})$. Some trap geometries are not suited for the realization of an OJE. This will be discussed more deeply in Section 4.3.2. At time $t = 0$, a time-periodic weak driving potential,

$$V(\mathbf{x}, t) = V(\mathbf{x}, t + T), \tag{4.2}$$

is switched on. The dynamics of the system is determined by the Heisenberg equation of motion for bosonic field operators,

$$\mathrm{i}\partial_t \hat{\psi}(\mathbf{x}, t) = H_0(\mathbf{x})\hat{\psi}(\mathbf{x}, t) + V(\mathbf{x}, t)\hat{\psi}(\mathbf{x}, t) + \frac{\lambda}{2}\hat{\psi}^\dagger(\mathbf{x}, t)\hat{\psi}(\mathbf{x}, t)\hat{\psi}(\mathbf{x}, t), \tag{4.3}$$

where $H_0(\mathbf{x}) \equiv \frac{1}{2}\nabla^2 + V_{\text{trap}}(\mathbf{x})$ is the single particle part of the unperturbed Hamiltonian, consisting of kinetic energy and external potential. This equation is a version of Eq. (3.37) with a specific particle statistics and interaction type. The basic concepts of the Heisenberg picture and the algebraic structure of the field operators was discussed in Section 3.4. The semi-classical limit of the equation of motion for bosonic field operators is given by the Gross-Pitaevskii equation, which was introduced in Section 3.3. The interaction strength λ is proportional to the s-wave scattering length and depends on the trap geometry, but is independent on the total particle number.

4.2.1. Resonantly driven single-particle system

For illustrative purposes, begin with a study of the noninteracting case, before considering the many-body case. This justifies a calculation in the single-particle picture. Later on, the obtained results will be translated to the equation of motion for field-operators including particle interactions.

To start, we translate the single particle Hamiltonian $H_0(\mathbf{x}) + V(\mathbf{x}, t)$ to the Sambe space $\mathcal{R} \otimes \mathcal{T}$, introduced in Section 3.2.1, and represent it in the discrete basis of un-

perturbed Floquet states $|\ell\, m\rangle\!\rangle$, defined as the eigenstates of the unperturbed Floquet operator,

$$\mathcal{H}_0 = H_0(\mathbf{x}) - \mathrm{i}\partial_{t'}, \tag{4.4}$$

which factorizes into time-like plane waves and the eigenstates $\phi_\ell(\mathbf{x})$ of $H_0(\mathbf{x})$

$$\langle\!\langle \mathbf{x}\, t|\ell\, m\rangle\!\rangle = e^{-\mathrm{i}m\omega t}\phi_\ell(\mathbf{x}). \tag{4.5}$$

Note that the unperturbed Floquet operator $\mathcal{H}_0$ is time-independent, but can formally be considered to have the period of the driving $V(\mathbf{x}, t)$. We focus on a driving of the form

$$V(\mathbf{x}, t) = \cos(\omega t + \vartheta)V(\mathbf{x}), \text{ with } \omega = 2\pi/T, \tag{4.6}$$

where ϑ is a real-valued parameter that is determined by the time-point at which the driving potential is switched on. This driving can be obtained experimentally as superposition of an intensity modulated potential, $V(\mathbf{x})$, and its inverted potential, $-V(\mathbf{x})$, modulated with a timely shift of $T/4$, i.e.,

$$V(\mathbf{x}, t) = \cos^2(\omega t/2 + \vartheta/2)V(\mathbf{x}) - \sin^2(\omega t/2 + \vartheta/2)V(\mathbf{x}). \tag{4.7}$$

Such type of modulations can be experimentally realized via an acousto-optic modulator [SKH+09][2].

The matrix elements of the full Floquet operator $\mathcal{H} = \mathcal{H}_0 + V(\mathbf{x}, t')$ in this basis read

$$\langle \ell m|\mathcal{H}|\ell' m'\rangle = \delta_{\ell\ell'}\delta_{mm'}\varepsilon^0_{\ell m} + V_{\ell\ell'}\tfrac{1}{2}\left(e^{\mathrm{i}\vartheta}\delta_{m+1,m'} + e^{-\mathrm{i}\vartheta}\delta_{m,m'+1}\right), \tag{4.8}$$

which involves the unperturbed quasienergies $\varepsilon^0_{\ell m} \equiv \varepsilon^0_\ell - m\omega$, with $\varepsilon^0_\ell \equiv \langle \ell|H_0(\mathbf{x})|\ell\rangle$; and the matrix elements of the driving potential,

$$V_{\ell\ell'} \coloneqq \int d\mathbf{x}\, \phi^*_\ell(\mathbf{x})V(\mathbf{x})\phi_{\ell'}(\mathbf{x}). \tag{4.9}$$

The system shall be initialized in an eigenstate of the undriven Hamiltonian. This initial state will be labeled as $|\ell = 1\rangle$. Within the tt'-formalism this initial state is given by $|\psi_0(t')\rangle \equiv |\ell\rangle$, i.e. $|\psi_0\rangle\!\rangle = |\ell = 1, m = 0\rangle\!\rangle$, cf. Chapter 3.

The following conditions shall be imposed on the driving field: First, there exists a further orbital, denoted as $|2\rangle$, to which the driving potential couples, i.e. $\langle 1|V(\mathbf{x})|2\rangle \neq 0$. Second, the driving frequency ω shall be near-resonant, i.e., close to the energy difference, $\omega_0 \coloneqq \varepsilon^0_2 - \varepsilon^0_1$, between $|1\rangle$ and $|2\rangle$. This means that the driving frequency can be expressed as $\omega = \omega_0 + \Delta$, where Δ is a possible detuning from exact resonance. It should satisfy $\Delta < \frac{1}{2}|\omega_0 - \omega_1|$, where ω_1 is the resonance closest to ω_0. When these two conditions are met, we say that the driving $V(\mathbf{x}, t)$ induces a resonant coupling between $|1\rangle$ and $|2\rangle$. As final condition, the driving $V(\mathbf{x}, t)$ shall not induce a resonant coupling between the state $|1\rangle$ ($|2\rangle$) and a third state. Within the tt'-formalism, this means that exactly one further state $|\ell = 2, m = 1\rangle\!\rangle$ exists which is quasi-degenerate with respect to the unperturbed Floquet operator, and to which the driving potential has nonzero coupling. As a consequence a two level description of the system is justified [Sch07].

A typical approach to extract the long-time dynamics of such a driven system is obtained via the rotating wave approximation (RWA) [GH98]. The reason why the approach presented here makes use of the tt'-formalism, instead of the RWA, is that in Chapter 5 and 6 these concepts will be extended to driven potentials that contain a

[2] The information that an acousto-optic modulator was used in this experiment is not given in the cited reference. It was obtained via a private communication with Tobias Salger.

second harmonic in the time-like part and induce a coupling among three modes. Such systems are beyond the standard use of RWA, while the tt'-formalism can straightforwardly be applied to more general types of driving. The state $|\ell = 2, m = -1\rangle\!\rangle$ would be the resonant state for a negative driving frequency and a phase $\vartheta = \pi$. In the end, it is rather a question of convention whether the perturbation couples to $|2, 1\rangle\!\rangle$ or $|2, -1\rangle\!\rangle$.

With a truncation to the two modes $|1\,0\rangle\!\rangle$ and $|2\,1\rangle\!\rangle$ the second quantum number m can be deduced from the value of the first quantum number ℓ. Therefore, the second number can be omitted and we can refer to the states $|1\,0\rangle\!\rangle$ and $|2\,1\rangle\!\rangle$ as $|1\rangle$ and $|2\rangle$[3] respectively.

As a result, the dynamics of the system is well approximated by the two-level Hamiltonian that is obtained by projecting the original Hamiltonian (4.8) to the subspace that is spanned by the modes $|1\rangle$ and $|2\rangle$. The resulting Hamiltonian is, up to a constant energy shift $\frac{1}{2}(3\varepsilon_1^0 - \varepsilon_2^0 + \omega)$, given by the matrix

$$H_{\mathrm{TL}} = \frac{1}{2}\begin{pmatrix} -\Delta & v e^{\mathrm{i}\vartheta} \\ v^* e^{-\mathrm{i}\vartheta} & \Delta \end{pmatrix} \tag{4.10}$$

where $v \equiv \langle 1|V(\mathbf{x})|2\rangle$ is the matrix element of $V(\mathbf{x})$ between the two modes and $\Delta = \omega - (\varepsilon_2^0 - \varepsilon_1^0)$ is a small detuning from exact resonance.

4.2.2. Resonantly driven many-particle system

The Hamiltonian (4.10) either describes a single particle system or a gas of ideal bosons ($\lambda = 0$) in which each particle moves independently. In the following the effective two-level description from the previous section will be extended to the case of interacting particles.

To this end, we come back to the equation of motion of field operators (4.3). As was shown in Chapter 3, we can apply the tt'-formalism also to the dynamics of field operators. It was further shown that we can represent the tt'-version of Eq. (4.3) with respect to the unperturbed Floquet states of the system, see Eq. (3.50).

Entering the matrix elements given in Eq. (4.8) into Eq. (3.50) we obtain

$$\begin{aligned} i\partial_t \hat{a}_{\ell m}(t) = \varepsilon^0_{\ell m}\hat{a}_{km}(t) + \sum_{\ell'} V_{\ell\ell'}\frac{1}{2}(\hat{a}_{\ell',m+1}e^{\mathrm{i}\vartheta} + \hat{a}_{\ell',m-1}e^{-\mathrm{i}\vartheta}) \\ + \lambda \sum_{\ell_1\ell_2\ell_3}\sum_{m_1m_2m_3} \delta_{m+m_1,m_2+m_3} w_{\ell\,\ell_1,\ell_2\ell_3}\, \hat{a}^\dagger_{\ell_1 m_1}(t)\hat{a}_{\ell_2 m_2}(t)\hat{a}_{\ell_3,m_3}(t), \end{aligned} \tag{4.11}$$

for all ℓ, m. For contact interaction the two-body matrix elements, involved in the latter sum of this equation, read

$$w_{\ell_1\ell_2,\ell_3\ell_4} \equiv \int d^3\mathbf{x}\; \phi^*_{\ell_1}(\mathbf{x})\phi^*_{\ell_2}(\mathbf{x})\phi_{\ell_3}(\mathbf{x})\phi_{\ell_4}(\mathbf{x}). \tag{4.12}$$

With the conditions on the driving potential given in Section 4.2.1, and the further condition of weak particle interactions, we can assume that the two-level description, involving only those modes that have nearly degenerate quasienergies $\varepsilon^0_{\ell m}$ with the initial mode, remains valid. Therefore, the set of equations (4.11) can be truncated to a set of equations that only involves the operators $\hat{a}_{1\,0}$, $\hat{a}_{2\,1}$, and their Hermitian adjoint.

Note that in general, particle interactions induce a coupling to further modes and could invalidate the two-level description. Therefore we consider weakly interacting particles

[3] For convenience, we also omit the notation $|\cdot\rangle\!\rangle$ which is just to emphasize that these states live in the extended Hilbert space $\mathcal{R} \otimes \mathcal{T}$.

and a weak driving potential, such that the set of modes participating in the dynamics is mainly determined by the undriven single particle part, given by the quasienergies $\varepsilon^0_{\ell m}$ in Eq. (4.11). This justification of a two-level truncation cannot be deduced merely from Eq. (4.11) since the Heisenberg picture does not factor in the initial preparation of the system, but only the initial action of the operators.

For the case of interacting particles, the initial condensate orbital, given by $\ell = 1$ will be depleted to some extent. However, the assumption of a nearly fully condensed initial state is justified for

$$\lambda N \ll \Delta E, \tag{4.13}$$

where ΔE is the the energy difference with neighboring single particle levels. This condition of weak particle interactions shall be assumed here. The effect of initial depletion will be discussed more deeply in Chapter 6.

For the single-particle case, cf. Section 4.2.1, within the truncated picture, the second index m can be omitted, since its value can be deduced from the value of the quantum number ℓ.

An important benefit of a truncation of the Hilbert space to the two modes $|1\rangle$ and $|2\rangle$ is that the commutation relations (3.49) become those of standard bosonic creation and annihilation operators:

$$[\hat{a}_{\ell'}(t), \hat{a}^\dagger_\ell(t)] = \delta_{\ell'\,\ell}\ , \text{ and} \tag{4.14a}$$

$$[\hat{a}_{\ell'}(t), \hat{a}_\ell(t)] = [\hat{a}^\dagger_{\ell'}(t), \hat{a}^\dagger_\ell(t)] = 0\,, \text{with } \ell', \ell \in \{1, 2\}. \tag{4.14b}$$

In this truncated picture, Eq. (4.11) reduces to a system of two equations,

$$\begin{aligned} \mathrm{i}\partial_t \hat{a}_1 &= -\tfrac{1}{2}\Delta\hat{a}_1 - \tfrac{1}{2}\theta\hat{a}_2 + \lambda\Big(\bar{w}_1\hat{n}_1 + 2\bar{w}_{12}\hat{n}_2\Big)\hat{a}_1, \text{ and} \\ \mathrm{i}\partial_t \hat{a}_2 &= \tfrac{1}{2}\Delta\hat{a}_2 - \tfrac{1}{2}\theta^*\hat{a}_1 + \lambda\Big(\bar{w}_2\hat{n}_2 + 2\bar{w}_{12}\hat{n}_1\Big)\hat{a}_2\,, \end{aligned} \tag{4.15a}$$

where $\hat{n}_\ell = \hat{a}^\dagger_\ell\hat{a}_\ell$, and $\theta = ve^{i\vartheta}$. Furthermore, the abbreviations $\bar{w}_1 \equiv w_{11,11}$, $\bar{w}_2 \equiv w_{22,22}$, and $\bar{w}_{12} \equiv w_{12,12}$ have been introduced. These are the key overlap terms, corresponding to interactions within mode $|1\rangle$, within mode $|1\rangle$, and between modes $|1\rangle$ and $|2\rangle$. With contact interaction the indices in the two-body matrix elements are symmetric under a swap of the first two or the last two indices. For that reason, $\bar{w}_{12} = \bar{w}_{21}$ has four equivalent permutations of indices, which explains the prefactor 2. It is important to note that the Kronecker delta in the second quantum number m in Eq. (4.11) has to be taken into account as well. That is why terms like $w_{11,12}$, $w_{22,21}$, or other terms with permuted indices of these do not appear. The first Kronecker-delta in the indices m makes these two-body matrix elements effectively vanish.

In contrast to the full set of equations of motion (4.11), the truncated equations of motion (4.15) can be regarded as Heisenberg equations of motion coming from the two-level Hamiltonian

$$\begin{aligned} \hat{H}_{\mathrm{TL}} = -\tfrac{1}{2}\theta\hat{a}^\dagger_1\hat{a}_2 + \mathrm{h.c.} - \tfrac{1}{2}\Delta(\hat{n}_1 - \hat{n}_2) + u_1\frac{\lambda}{2}\hat{n}_1(\hat{n}_1 - 1) + u_2\frac{\lambda}{2}\hat{n}_2(\hat{n}_2 - 1) \\ + \lambda w_{12}(\hat{N}^2 - \hat{N}), \end{aligned} \tag{4.16}$$

with

$$u_\ell = \bar{w}_\ell - 2\bar{w}_{12}, \tag{4.17}$$

and $\hat{N}$ being the total particle number operator. For systems with conserved particle number, the last term in Hamiltonian (4.16) has no effect on the dynamics and can hence

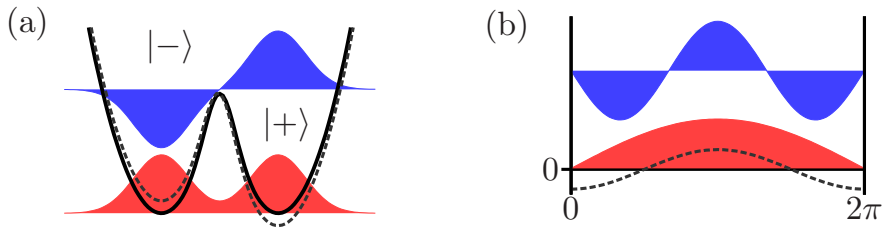

Figure 4.3.: *Schematic illustration of the example systems discussed*: (a) driven two-mode system, (b) box-potential with driving. The dashed line illustrates the deformation of the trapping potential due to the driving. For illustrative purposes, the driven two-mode system (a) is here depicted as a double-well trap. The considerations in Section 4.3.1 may also refer to an internal Josephson system.

be skipped. With the last term skipped, Hamiltonian (4.16) is that of a BJJ, with the peculiarity of a mode-dependent interaction strength.

If more than two modes are involved, it is still possible to incorporate the particle interactions in the same manner. However, in general the particle interactions will include terms that induce a mixture among the modes. Additionally, the complexity grows fast with the inclusion of further states. For example, if a third state would participate in the dynamics one can encounter two main cases for the time-like quantum number m: (i) they can all be different, e.g. $m = 0, 1, 2$, or (ii) two of them can be equal, e.g. $m = 0, 1, 1$. In Chapter 6, the case of three modes having the exact same spatial density distribution is presented.

4.3. Example systems

This section presents two examples of specific setups that meet the characteristics listed in the previous section, and hence represent a realization of an OJE. A schematic illustration of the systems discussed here is shown in Fig. 4.3.

4.3.1. Minimal example: driven two-mode system

The first explicit example of an OJE is given by a conventional[4] two-mode BJJ. For convenience, the modes are labeled with L and R. Accordingly, our starting point is a driven bosonic two-mode Hamiltonian

$$\hat{H}(t) = -\tfrac{1}{2}J(\hat{a}_L^\dagger \hat{a}_R + \hat{a}_R^\dagger \hat{a}_L) + \frac{\lambda}{2}\sum_{i=L,R} \hat{n}_i(\hat{n}_i - 1) + \tfrac{1}{2}K\cos(\omega t + \vartheta)(\hat{a}_L^\dagger \hat{a}_L - \hat{a}_R^\dagger \hat{a}_R), \quad (4.18)$$

where $\hat{a}_i^\dagger$ ($\hat{a}_i$) are bosonic creation (annihilation) operators with respect to the modes $i = L, R$, and $\hat{n}_i \equiv \hat{a}_i^\dagger \hat{a}_i$ is the occupation number operator of mode i. Just as for the general case, discussed in the previous section, the driving is switched on at $t = 0$. The eigenmodes of the undriven single particle part of Hamiltonian (4.18) are given by the bonding and anti-bonding state

$$|\pm\rangle \equiv \frac{1}{\sqrt{2}}\Big(|L\rangle \pm |R\rangle\Big). \quad (4.19)$$

[4] Conventional means here either internal or external.

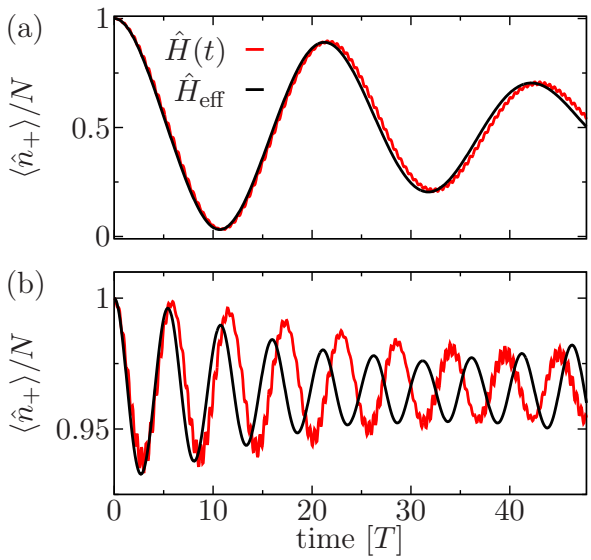

Figure 4.4.: *Time-evolution of a driven bosonic two-mode system.* Shown is the normalized occupation of the initial mode $|+\rangle$ in two dynamical regimes. (a) Josephson oscillations are observed for weak interaction strength ($\lambda N = 0.1$). (b) For large interaction strength ($\lambda N = 0.4$), the system is self-trapped in the initial mode $|+\rangle$ – note the different scaling on the vertical axes. Parameters are: $N = 30$, $J = 1$, $K = 0.05$, $\vartheta = \frac{1}{2}\pi$, $\omega = 1$, ($\Delta = 0$).

Their energy difference is $\varepsilon_- - \varepsilon_+ = J$. Note that $\varepsilon_+ < \varepsilon_-$. For weak driving strengths K, and when the system is initially condensed in one of the eigenmodes $|\pm\rangle$, we can apply the recipe presented in Section 4.2 and obtain an effectively time-independent description of the system. In this minimal example, the two-body matrix elements have the simple form

$$w_{--,--} = w_{-+,-+} = w_{++,++} = \frac{1}{2}. \tag{4.20}$$

All the other elements of w can be either obtained by permutation of the indices, or vanish. In any case, the above listed elements are all we need to apply the prescription (4.17). Hence we obtain an effective inversion of the interaction strength, i.e. $u_\pm = -1$. The matrix element of the driving is $v = \frac{1}{2}K$, and the potential difference is given by $\Delta = \omega - J$. With these quantities, the effective two-level Hamiltonian (4.16) is fully determined.

Figure 4.4 shows a comparison of the dynamics, governed by the original many-body Hamiltonian (4.18) (red curve) and the time-independent effective Hamiltonian (4.16) (black curve). We can see that the qualitative behavior of the system, changing from a Josephson oscillation to a self-trapped regime as the coupling is increased, is reproduced well. However, discrepancies are also visible on closer inspection. The curve referring to the original system in Fig. 4.4 features a fast oscillation whose frequency is similar to that of the external driving potential. One clearly sees that the effective description refers to the long-term behavior of the system and does not show this oscillation. Furthermore, there is a discrepancy in the long-term behavior, which becomes more evident for stronger particle interactions. The precision of the effective description as orbital Josephson junction, given by Hamiltonian (4.16), will be more deeply discussed in Section 6.6.

4.3.2. Box potential with modulated lattice

A second illustrative example is given by a BEC with a single spatial degree of freedom, trapped in a box potential of length 2π:

$$V_{\text{box}}(x) = \begin{cases} 0, & \text{for } 0 \leq x \leq 2\pi \\ \infty, & \text{otherwise} \end{cases}. \tag{4.21}$$

The eigenfunctions of the single particle Hamiltonian are standing waves

$$\phi_k(x) = \frac{1}{\sqrt{\pi}} \cos(kx/2), \tag{4.22}$$

where k is a natural number, and the related energy eigenvalue is given by $\varepsilon_k = k^2/8$. In this basis the two-body matrix elements for contact interaction are given by

$$w_{kl,k'l'} = \frac{1}{2\pi}\Big[\delta_{|k-l|,|k'-l'|} \cdot (1+\delta_{kl}) + \delta_{k+l,k'+l'} - \delta_{|k-l|,k'+l'} - \delta_{k+l,|k'-l'|}\Big]. \tag{4.23}$$

As spatial part of the driving potential, we consider a lattice that is composed by a single spatial harmonic

$$V(x) = \cos(\kappa x/2), \tag{4.24}$$

where κ is an integer valued parameter. The matrix elements, with respect to the standing waves (4.22) read

$$\langle k|V|l\rangle = \tfrac{1}{2}\delta_{|k-l|,\kappa}. \tag{4.25}$$

Therefore, the potential $V(x)$ induces a coupling among those modes that a have momentum difference $(k-l)$ of magnitude κ. A condensate that is initially prepared in a certain condensate wave-function k_0, will couple either to the mode $|k_0+\kappa\rangle$ or $|k_0-\kappa\rangle$. A simultaneous coupling to both modes is suppressed, because the driving frequency ω cannot match both energy spacings.

At this point, it should become clear why a harmonic trap would not be suitable for the realization of an OJE. For a harmonic trap the spacing of neighboring energy levels is constant. This means a resonant driving frequency would in general induce a subsequent coupling to all eigenmodes of the system. However, in actual experiments traps are only locally harmonic. Optical traps for example are built on Gaussians [BDZ08], and harmonic plus quartic traps have also been used [BSSD04]. So in general one does not require a box potential, and a series of extant experimental systems are viable for the OJE. The illustrative example here can be adapted straightforwardly to these systems.

As in the previous example, the effective interaction strength for the box potential is $u_k = -1$, independent of the modes $|k_0\rangle$ and $|k_0 \pm \kappa\rangle$ that form the orbital Josephson system. This is a consequence of the symmetry properties of the original system.

Conclusions

A novel type of Josephson junction in BECs was introduced, in which the macroscopically occupied modes are single-particle wave functions whose densities may overlap strongly. This differs from the standard examples of the internal and external Josephson effects. So far, two specific examples have been presented. For one of them, it was shown that the underlying effective description is correct, but we could also observe discrepancies between the effective description and the full dynamics. An important result is that the truncation of Hilbert space within the tt'-framework yields a valid approximation to the

dynamics of the full system. Previous applications of the tt'-formalism mainly focused on the possibility to deploy methods that are originally developed for systems with a static Hamiltonian. Therefore, a novel application of the tt'-formalism is presented in this chapter.

5. Weakly driven coherent quantum ratchets

In this chapter[1] we study of the dynamics of a particle, subject to a weak space- and time-asymmetric driving potential. The obtained analytical results are supported by a comparison with a numerical study. For now, we will focus on systems without particle interactions, which justifies a single particle treatment. The driving potentials considered here give rise to a ratchet effect, which will be further discussed in the next section.

5.1. Ratchet systems

Ratchets are systems in which directed motion is created although the acting forces vanish on average [Rei02]. One of the earliest thought experiments in this direction is the so called Brownian ratchet [Smo12], which became popular through the Feynman Lectures on Physics [Fey63, PE96]. In this example the external forces originate from thermal fluctuations, which can be modeled as a source of dissipation on the system. Ratchets also are a model for molecular motors [JAP97]. These are complex organic molecules that are able to perform mechanical work, like duplication of DNA strings, while burning chemical energy of the surrounding medium.

In the following, we will focus on Hamiltonian quantum ratchets. In these systems a particle current is induced via a time-periodic driving field. An important difference from Brownian ratchets is that dissipation plays a negligible role in the creation of directed motion. Without dissipation the Hamiltonian itself has to break space and time-inversion symmetry in order to produce ratchet motion [Rei02]. Such symmetry breaking can be achieved by a two-harmonic driving potential of the type shown in Fig. 1.2. Hamiltonian quantum ratchets are a fundamental arena for the study of transport processes in quantum systems, and their realization based on BECs has gained increasing interest in recent years [DKH09, DMMFH07, MMF08, PBC+09, CS09, BCD+10, CS10, HCS10, HCCS12, SMOR11].

The ratchet systems considered here model a fully condensed ideal Bose gas, but could equally well describe a single particle, regardless of its underlying particle statistics. In Chapter 6, an extension of this analysis to interacting Bose gases will be presented. Two distinct basic topologies for the creation of a particle current are typically considered: An infinitely extended periodic setup, i.e. a lattice potential, or a circulating flow in a ring structure. In the case of a classical particle both possibilities are mathematically equivalent, as can be made clear with the example of a pendulum in a static force field – see Fig. 5.1. In a quantum mechanical systems, this equivalence is lost in general. A stationary quantum particle in an extended lattice potential can be characterized by the phase difference between two endpoints of a unit cell, viz. its quasi momentum. The corresponding wave function can have a periodic density with the same periodicity as the potential, but can still exhibit a broken translational symmetry in its phase [AM76]. Only if phase and density both fulfill the same translational symmetry as the lattice does, the equivalence, discussed above, remains valid for the quantum counterpart. A

[1] The main results of the present chapter are published as part of this thesis in Refs. [HCS10, HHC+].

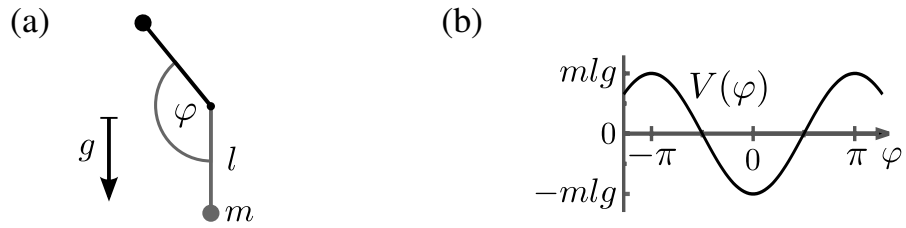

Figure 5.1.: *Periodic boundary conditions versus extended lattice.* (a) A rigid pendulum with length l and mass m exposed to a gravitational field of strength g is mathematically equivalent to (b) a particle moving in a sinusoidal lattice potential with amplitude mlg and lattice constant 2π. For the quantum version of the these setups, these equivalence does not hold in general.

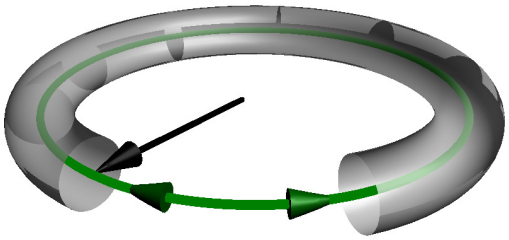

Figure 5.2: Equipotential surface of a ring trap and effective degree of freedom, indicated by the green line. The black arrow shows the major radius R of the torus.

system where periodic boundary conditions for density and phase are enforced, is given by a particle trapped in a ring geometry. Such a trap geometry will be more deeply discussed in the next section.

5.2. BECs in ring traps

Trapping potentials whose equipotential surfaces close to the potential minimum form tori, as depicted in Fig. 5.2, are called ring traps, given that the confinement in the direction of the minor radius of the torus (perpendicular confinement) is sufficiently strong. The major radius R of the torus is a characteristic quantity of the trapping potential and will be used here as natural length scale, i.e. we express all lengths in units of R. Accordingly, for a system with atom mass M, $\hbar^2/MR^2$ serves as a unit for energies, $MR^2/\hbar$ serves as a time-scale, and its inverse as a frequency unit. The perpendicular confinement can typically be modeled as harmonic, and we will denote its characteristic trapping frequency by $\omega_\perp$. If the characteristic length of the perpendicular confinement $r_\perp = \sqrt{\hbar/M\omega_\perp}$ is small compared to R, i.e. $\omega_\perp \gg 1$ in the natural units of the system, the motion of the particles becomes effectively constrained along the major radius and we can describe the system by a single degree of freedom with periodic boundary conditions.

One of the first experimental realizations of a BEC in a ring trap was presented in Ref. [RAC+07]. In this work, a BEC of about $2 - 5 \cdot 10^5$ ^{23}Na atoms (mass $M_{\mathrm{Na}} = 22.99\,\mathrm{u} = 3.8 \cdot 10^{-26}\mathrm{Kg}$) was confined in a ring trap with major radius $R \approx 10\mu$m. Thus, the relevant time scale is $t_0 \approx 36$ms, and the energy difference between the ground state and the first excited state corresponds to a frequency of about 900Hz. A driving potential that couples between the initial state and the first excited state would have a resonance at this frequency.

A particle flow inside the ring can be observed with time-of-flight measurements [RAC+07]. For non-rotating condensates, the initial hole at the center is filled in during expansion [DGPS99], while for the rotating case the hole persists. Nowadays, there are

many experimental works with BECs in ring traps, set up with time-orbiting potentials [RAC+07, RWM+11, MBS+12], magnetic traps [AGR06], and "painted" time-averaged optical dipole potentials [HRMB09]. Furthermore, there are proposals for trap designs that are especially well-suited to reach regimes of effectively reduced dimensionality [MCL+06], which is considered in this work.

We consider an ideal Bose gas at zero temperature, trapped in a such ring geometry. Its dynamics is described by the time-dependent Schrödinger equation for a system with a single degree of freedom and periodic boundary conditions

$$i\partial_t\psi(x,t) = H(x,p,t)\psi(x,t) \tag{5.1a}$$
$$= [\tfrac{1}{2}p^2 + V(x,t)]\psi(x,t). \tag{5.1b}$$

Here, x is the remaining degree of freedom, given by the angle along the circumference of the ring, and $p = -\mathrm{i}\partial_x$ is the operator for the angular momentum. The time-periodic driving potential,

$$V(x,t+T) = V(x,t), \tag{5.2}$$

is switched on at $t = 0$, and as initial state, we choose the ground state of the undriven system, given by the zero angular momentum mode

$$\psi(x,t=0) = \frac{1}{\sqrt{2\pi}}. \tag{5.3}$$

The preparation of a BEC in this state can be accomplished by cooling of the undriven system.

According to the considerations of Section 5.1, Eq. (5.1) can also describe the dynamics of a particle on an extended lattice whose quasimomentum vanishes initially, given that the driving does not couple among states with different quasimomenta. Particle interactions can induce a coupling to states with nonzero quasimomentum via so-called umklapp processes.

5.3. Symmetry aspects

As has been mentioned in the introduction, symmetries play a major role in ratchet systems. It was shown by Flach et al. [FYZ00] that for the creation of a finite dc particle current in a classical system, time and space inversion symmetry must be broken. In further works these symmetry considerations were successfully extended to the quantum case [DMMFH07, DKH09, GH98]. To be precise, in a one-dimensional system the underlying time-periodic Hamiltonian $H(x,p,t)$ must not be invariant under two transformations. Those are

$$\text{generalized parity } (x,t) \to (2x_\mathrm{S} - x, t + T/2), \tag{5.4a}$$
$$\text{and time-inversion } t \to 2t_\mathrm{S} - t, \tag{5.4b}$$

where x_S and t_S are the origins of parity and time-inversion symmetry respectively. The kinetic energy term of the Hamiltonian given in Eq. (5.1) is symmetric under these transformations. Accordingly, the driving potential $V(x,t)$ has to break these symmetries in order to induce a long-lasting nonzero particle current.

The instantaneous overall particle current, $I(t)$, is simply given by the expectation

value of the angular momentum,

$$I(t) = \langle\psi(t)|p|\psi(t)\rangle = -\mathrm{i}\int dx\, \psi(x,t)^* \partial_x \psi(x,t). \tag{5.5}$$

The ratchet effect refers to the asymptotic time-averaged particle current [DMMFH07], defined as

$$\bar{I} = \lim_{t\to\infty} \frac{1}{t}\int_0^t dt'\, I(t'). \tag{5.6}$$

Nevertheless, there has been increasing interest in the creation of a transient particle current by means of an unbiased driving potential [PBC+09, CS09, SMOR11].

The solution of the Schrödinger equation (5.1), $|\psi(t)\rangle$, can be represented in terms of Floquet states $|\phi_\nu(t)\rangle$, cf. Eq. (3.20),

$$|\psi(t)\rangle = \sum_\nu e^{-\mathrm{i}\varepsilon_\nu t} A_\nu\, |\phi_\nu(t)\rangle\,, \tag{5.7}$$

with $A_\nu = \langle\psi(0)|\phi_\nu(0)\rangle$. Assuming that there is no degeneracy among the quasienergies ε_ν, and following the same argument as given in Box 2.3.1, we can express the time-averaged current as

$$\bar{I} = \sum_\nu |A_\nu|^2 \frac{1}{T} \langle\!\langle \phi_\nu|p|\phi_\nu\rangle\!\rangle\,, \text{ with } \langle\!\langle \phi_\nu|p|\phi_\nu\rangle\!\rangle \equiv \int_0^T dt\, \langle\phi_\nu(t)|p|\phi_\nu(t)\rangle\,. \tag{5.8}$$

This implies that the emergence of dc currents in Hamiltonian quantum systems is possible when the system features transporting Floquet states [DMMFH07]; i.e. states that have a nonzero momentum, averaged over a single period.

5.4. Discrete representation

The main analysis in this chapter will be given within the tt'-formalism. Therefore, we are considering states that live in the extended Hilbert space $\mathcal{R}\otimes\mathcal{T}$, which was introduced in Section 3.2.1. We will consider systems with weak driving. This implies that the dynamics will be dominated by the eigenstates of the kinetic energy part of the Hamiltonian. Therefore, within the tt'-framework, the predominant part is given by unperturbed Floquet operator

$$\mathcal{H}_0 = \tfrac{1}{2}p_x^2 - \mathrm{i}\partial_{t'}, \tag{5.9}$$

whose eigenstates are the unperturbed Floquet states, given by

$$\phi_{\ell m}(x,t) \equiv \frac{1}{\sqrt{2\pi}} \exp(\mathrm{i}\ell x - \mathrm{i}\omega m t') = \langle\!\langle xt|\ell m\rangle\!\rangle\,. \tag{5.10}$$

Here, ℓ refers to the angular momentum and m is the analog *quantum number* for the t'-dependence of $\phi_{\ell m}$. The corresponding unperturbed quasi energy reads

$$\varepsilon^0_{\ell m} \equiv \langle\!\langle \ell m|\mathcal{H}_0|\ell m\rangle\!\rangle = \tfrac{1}{2}\ell^2 - m\omega. \tag{5.11}$$

In Chapter 6, this basis serves as representation of creation and annihilation operators.

Using this basis, we can express any time-periodic potential, with period T, via the Fourier sum

$$V(x,t') = \frac{1}{\sqrt{2\pi}T} \sum_{\ell,m} V_{\ell,m} \exp(-\mathrm{i}\ell x + \mathrm{i}\omega m t'), \tag{5.12}$$

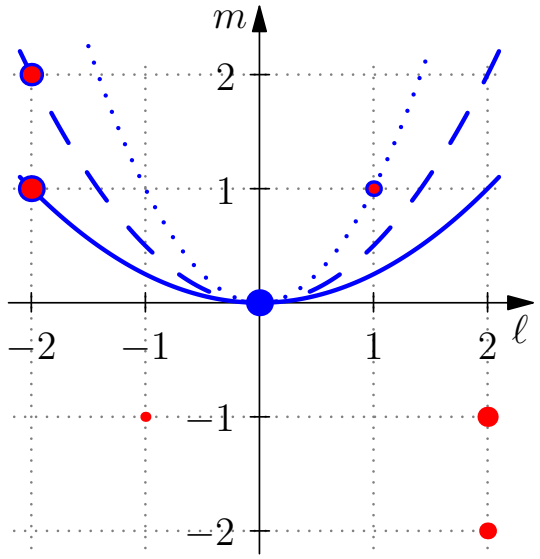

Figure 5.3: *Graphical illustration of resonance condition.* The size of each red dot reflects the absolute value of the Fourier component of $V(x,t)$ – cf. Eq. (5.16). The condition (5.14) causes a point symmetry with respect to the origin. The three curves refer to the three main resonant driving frequencies: $\omega = 2$ (solid line), $\omega = 1$ (dashed line), $\omega = 0.5$ (dotted line).

where the Fourier modes $V_{\ell,m}$ can be viewed as matrix elements with respect to the unperturbed Floquet states, i.e.

$$V_{\ell,m} = \langle\langle 0\,0|V|\ell m\rangle\rangle = \frac{1}{\sqrt{2\pi}} \int dx\, dt\; V(x,t') \exp(\mathrm{i}\ell x - \mathrm{i}\omega m t'). \tag{5.13}$$

In order to obtain a real-valued driving potential, the Fourier components must satisfy the constraints

$$V_{\ell,m} = V^*_{-\ell,-m}. \tag{5.14}$$

Note that $|0\,0\rangle\rangle$ is the tt'-version of the initial state (5.3), when we use standard initial conditions, cf. Section 3.1.1. That is, a driving potential induces a direct coupling[2] between the initial mode $|0\,0\rangle\rangle$ and another mode $|\ell m\rangle\rangle$, if the related Fourier component $V_{\ell,m}$ is nonzero. Furthermore, within the tt'-formalism, the resonance condition from Section 4.2 can be expressed as

$$\varepsilon^0_{0\,0} - \varepsilon^0_{\kappa m} = 0 \Leftrightarrow m = \frac{1}{2\omega}\ell^2. \tag{5.15}$$

These resonance conditions can be illustrated by a graphical construction, shown in Fig. 5.3[3]. Nonzero Fourier components $V_{\ell,m}$ of the exemplary driving potential,

$$V(x,t) = +K_1 \cos(2x + \omega t) + K_2 \cos(2x + 2\omega t) + K_3 \cos(x - \omega t), \tag{5.16}$$

are given by red dots in a two-dimensional plane. The size of the dots roughly indicates the absolute value of the component, i.e. here $K_1 > K_2 > K_3$. Equation (5.15) defines a parabola on this plane whose minimum is placed at the origin. The curvature of the parabola is controlled via the driving frequency ω, and resonant states occur when the parabola *hits* a Fourier component (red dots).

For strong driving potentials, the width of the related resonance peaks become broader, until the response of the system becomes notable for almost all driving frequencies, in which case the notion of resonances rather loses its meaning.

In the subsequent sections, we will consider two different types of driving potential. Both potentials represent a realization of a ratchet potential and we will see in the

[2] The possibility of an indirect coupling will be discussed in Section 5.6.
[3] The idea of such a geometric interpretation of the resonance conditions goes back to Fernando Sols.

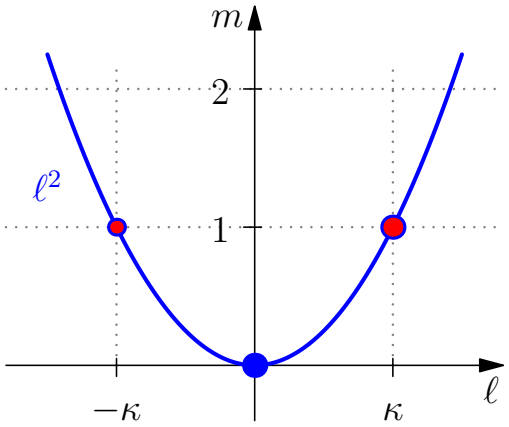

Figure 5.4: *Resonance condition for potential* V^{I}. Only the the upper half of the (ℓ, m)-plane is shown. The full construction is point symmetric at the origin – cf. Fig. 5.3. Both plane waves, contained in V^{I} are resonant at the same driving frequency ω.

following that both lead to an equivalent effective description.

5.5. Ellipsoidal driving

As first specific example, we consider the (real-valued) driving potential with the least number of nonzero Fourier modes that induces a coupling to two nonzero angular momentum modes. It is given by two counter-propagating harmonic waves

$$V^{\mathrm{I}}(x,t) = K_+ \cos(\kappa x - \omega t - \varphi_+) + K_- \cos(-\kappa x - \omega t - \varphi_-)\,. \tag{5.17}$$

The amplitude of each wave is controlled separately via $K_\pm$ and the relative phases $\varphi_\pm$ determine at which point and time the maxima collide. This driving may be called ellipsoidal driving, based on the following observation: For $\kappa = 1$ it can be realized via the inertial forces the particles feel, when the center of the ring trap orbits along an ellipse with eccentricity

$$\eta = (K_- - K_+)/K \in [-1:1]\,. \tag{5.18}$$

The eccentricity controls the breaking of both, the generalized parity (5.4a) and the time inversion symmetry (5.4b), which are broken for $|\eta| \neq 0$. An overall amplitude can be defined as

$$K = \frac{1}{2}(K_+ + K_-). \tag{5.19}$$

The modes to which the driving V^{I} couples is imposed via the wave vector κ, and the frequency ω controls whether this coupling is tuned to or near resonance.

The Fourier decomposition of V^{I} contains four summands:

$$V^{\mathrm{I}}_{\ell,m} = \frac{K_+}{2}\Big(e^{\mathrm{i}\varphi_+}\delta_{\ell,\kappa}\delta_{m,1} + e^{-\mathrm{i}\varphi_+}\delta_{\ell,-\kappa}\delta_{m,-1}\Big) + \frac{K_-}{2}\Big(e^{-\mathrm{i}\varphi_-}\delta_{\ell,\kappa}\delta_{m,-1} + e^{\mathrm{i}\varphi_-}\delta_{\ell,-\kappa}\delta_{m,1}\Big). \tag{5.20}$$

For resonant driving ($\omega = \frac{1}{2}\kappa^2$), V^{I} induces a coupling between the initial mode $|0\,0\rangle\!\rangle$ and the modes $|\pm\kappa\,1\rangle\!\rangle$. Fig. 5.4 illustrates the resonance condition and the corresponding resonant modes. In principle, the system couples to further states via higher order processes. For example, the next degenerate mode is given by $|2\kappa\,4\rangle\!\rangle$ and can be reached via a third order process in the driving. This means that the coupling between $|0\,0\rangle\!\rangle$ and $|2\kappa\,4\rangle\!\rangle$ will be proportional to K^3. Since we are considering weakly driven systems, the coupling to further modes can be neglected.

It was just argued that the dynamics will mainly involve the three modes $|-\kappa\,1\rangle\!\rangle$, $|0\,0\rangle\!\rangle$, and $|\kappa\,1\rangle\!\rangle$, which will be henceforth denoted by $|-\rangle$, $|0\rangle$, and $|+\rangle$ respectively. Furthermore, we will refer to the initial mode $|0\rangle$ as center mode and the nonzero angular momentum modes as side modes. The effective truncation to three modes holds also when the driving frequency is slightly detuned from exact resonance, i.e. $\omega = \frac{1}{2}\kappa^2 + \Delta$, as long as the detuning Δ is sufficiently weak. Accordingly, we can approximate the dynamics under driving V^{I}, by truncating the Hilbert space to the three main modes.

Accordingly, in this truncated picture the state $|\psi(t)\rangle\!\rangle$ is given by the triple (A_-, A_0, A_+), and the Hamiltonian $H(x, p, t')$ is represented by the matrix

$$H_{3\mathrm{LS}} = \begin{pmatrix} -\mu & \Gamma_- & 0 \\ \Gamma_-^* & 0 & \Gamma_+ \\ 0 & \Gamma_+^* & -\mu \end{pmatrix}, \tag{5.21}$$

where, in this case, the potential difference μ is simply given by the detuning ($\mu = -\varepsilon^0_{\pm\kappa\,1} = \Delta$) and the coupling terms, $\Gamma_\pm$, are the matrix elements of the driving potential V^{I} in this truncated picture

$$\Gamma_\pm = \frac{K_\pm}{2} e^{\mathrm{i}\varphi_\pm}. \tag{5.22}$$

An analysis of the dynamics of this three level system is given in Section 2.3, where it was shown that the dynamics under such a three-level Hamiltonian is given by a Rabi oscillation between the initial state and a further state, given by a superposition of the two side modes.

A numerical comparison of this truncated picture with the full dynamics is discussed in Chapter 6, where particle interactions will be included.

5.6. Factorisable driving

In the previous section we have considered a simple driving, in which the coupling strengths of the effective few-mode description are the *naked* matrix elements of the driving potential – see Eq. (5.22). In the following we will consider a driving that yields the same truncation to a three-level system, but the calculation of the transition elements $\Gamma_\pm$ requires a perturbational approach of the type introduced in Chapter 2. We will consider a driving that factorizes in a spatial and a time-like part, both of which can be decomposed in a first and a second harmonic:

$$V^{\mathrm{II}}(x,t) = KV(x)\cdot f(t), \text{ with} \tag{5.23a}$$

$$V(x) = \sin(\kappa x) + \alpha\sin(2\kappa x + \phi) \text{ and} \tag{5.23b}$$

$$f(t) = \sin(\omega t) + \beta\sin(2\omega t + \vartheta). \tag{5.23c}$$

The symmetry properties are controlled via the parameters α and ϕ for parity and analogously via β and ϑ for time-inversion symmetry. Space- (time-) inversion symmetry is broken for $\alpha \neq 0$ ($\beta \neq 0$) and for $\phi \neq \frac{1}{2}\pi, \frac{3}{2}\pi$ ($\vartheta \neq \frac{1}{2}\pi, \frac{3}{2}\pi$). This symmetry breaking via the contribution of a second harmonic is illustrated in Fig. 1.2. A driving potential of this type has been realized on an extended optical lattice [SKH+09]. It was loaded with a BEC with negligible particle interactions. For the case of an extended lattice, V^{II} conserves quasi momentum. Therefore, the system considered here is a model for the experiment of Ref. [SKH+09].

The matrix elements of V^{II} with respect to the plane-wave representation (5.13) are

given by

$$V^{\mathrm{II}}_{\ell,m} = -K\frac{1}{4}\Big(\delta_{-\kappa,\ell} - \delta_{\kappa,\ell} + \alpha e^{i\varphi}\delta_{-2\kappa,\ell} - \alpha e^{-i\varphi}\delta_{2\kappa,\ell}\Big) \cdot \Big(\delta_{\kappa,m} - \delta_{-\kappa,m} + \beta e^{i\vartheta}\delta_{2\kappa,m} - \beta e^{-i\vartheta}\delta_{-2\kappa,m}\Big). \quad (5.24)$$

The fact that V^{II} contains higher harmonics in both the spatial and the time-like part, causes a more complex spectrum of resonant driving frequencies than for the previously discussed potential V^{I}. A graphical representation of this driving is shown in Fig. 5.5, together with the parabolas (5.15) for the four main resonances at $\omega = 1/4$, $1/2$, 1, and 2, in which cases the parabola *hits* a nonzero Fourier mode of the driving. In complete analogy to the driving V^{I}, the modes that are hit by the parabola contribute mainly to the dynamics, because they are quasienergetically degenerate with the initial mode $|0\,0\rangle\!\rangle$. That means the dynamics under driving V^{II} can again be described with an effective three-level Hamiltonian in the same manner as with driving V^{I}. What differs in this case is the functional dependence of the transition elements $\Gamma_{\pm}$, and the potential difference μ, on the driving.

5.6.1. Truncated description

Each Fourier mode $V^{\mathrm{II}}_{\ell,m}$, depicted by the red dots in Fig. 5.5, represents a coupling between the initial mode $|0\,0\rangle\!\rangle$ and the Floquet mode $|\kappa m\rangle\!\rangle$ due to the driving. The reason why the system does not undergo transitions to all those modes to which V^{II} couples, is that they are quasienergetically too far away from the initial mode, and quasienergy is conserved in this system (cf. Section 3.2.3). Nevertheless, since this is a quantum mechanical system, quasienergy has a nonzero variance, except for the unlikely case that one starts with a Floquet eigenstate as initial state. This implies that the overlap between $|\psi(t',t)\rangle$ and a forbidden Fourier mode can be nonzero. One could say that the system is allowed to virtually visit the quasienergetically forbidden states. Such virtual transitions are represented by dashed arrows in Fig. 5.5, while solid arrows correspond to energetically allowed transitions. Therefore, the system can transit to the side modes either directly (first order transition), or indirectly via a virtually visited mode (second order transition).

Figure 5.6 shows a few mode representation of the situation described above for the resonance at $\omega = 1$, in the same manner as is introduced in Chapter 2. In this case the resonant side modes are $|\ell\, m\rangle\!\rangle = |-2\kappa\, 2\rangle\!\rangle$ and $|2\kappa\, 2\rangle\!\rangle$, and there exists only a single second order transition for each side mode, which includes the virtual transition to the mode $|\kappa\, 1\rangle\!\rangle$ and $|-\kappa\, 1\rangle\!\rangle$. Together with the initial mode $|0\,0\rangle\!\rangle$, we obtain five mainly contributing modes $|-2\kappa\, 2\rangle\!\rangle$, $|-\kappa\, 1\rangle\!\rangle$, $|0\,0\rangle\!\rangle$, $|\kappa\, 1\rangle\!\rangle$, and $|2\kappa\, 2\rangle\!\rangle$, which will be labeled as $|\bar{2}\rangle$, $|\bar{1}\rangle$, $|0\rangle$, $|1\rangle$, and $|2\rangle$ respectively.

According to Chapter 2, the virtual transition to the modes $|1\rangle$ and $|\bar{1}\rangle$ will modify the transition elements $\Gamma^{\mathrm{II}}_{\pm}$ between $|0\rangle$ and the side modes $|2\rangle$ and $|\bar{2}\rangle$. In the sense of Section 2.2.1, the coupling Γ^{II}_{+} between $|0\rangle$ and $|2\rangle$ is given by the corresponding matrix element of the T-matrix, calculated up to second order in the driving. The value of this matrix element reads

$$\Gamma^{\mathrm{II}}_{+} = \langle 0|\mathrm{T}|2\rangle = \langle 0|V|2\rangle + \langle 0|V|1\rangle\,\frac{1}{\frac{1}{2}}\,\langle 1|V|0\rangle = \frac{K}{4}\Big(\frac{K}{2} + \alpha\beta e^{-\mathrm{i}(\vartheta+\phi)}\Big). \quad (5.25)$$

ω	$\lvert\pm\rangle$	$\Gamma_{\pm}^{\mathrm{II}}$	μ
$\frac{1}{4}$	$\lvert\pm\kappa\,2\rangle$	$\frac{1}{4}K(\frac{1}{35}K\beta e^{-\mathrm{i}\vartheta} \pm \alpha e^{\mp\mathrm{i}\phi})$	2Δ
$\frac{1}{2}$	$\lvert\pm\kappa\,1\rangle$	$\frac{1}{40}K(K\alpha\beta e^{-\mathrm{i}(\vartheta\pm\phi)} \pm 1)$	Δ
1	$\lvert\pm 2\kappa\,2\rangle$	$\frac{K}{4}(\frac{K}{2} \pm \alpha\beta e^{-\mathrm{i}(\vartheta\pm\phi)})$	2Δ
2	$\lvert\pm 2\kappa\,1\rangle$	$-\frac{2}{7}K^2\alpha e^{\mp\mathrm{i}\phi} \mp K\beta e^{-\mathrm{i}\vartheta}$	Δ

Table 5.1.: Overview of the resonant modes, coupling terms, and potential energy differences that enter in the truncated picture given by H_{3LS} for the four main resonant driving frequencies of the driving potential V^{II}.

The calculation for the other side mode $|\bar{2}\rangle$ is done analogously, and we obtain

$$\Gamma_{\pm}^{\mathrm{II}} = \tfrac{1}{4}K\Big(\tfrac{1}{2}K \pm \alpha\beta e^{-\mathrm{i}(\vartheta\pm\phi)}\Big). \tag{5.26}$$

In this calculation, we have neglected the shift of the the unperturbed quasienergies $\varepsilon_{\kappa 1}^{0}$ of the intermediate modes due to a possible detuning Δ. This is justified for $\Delta \ll 1$.

In Section 2.2.1 we considered a further, qualitatively different, type of process, which shifts the potential energy of the modes in the truncated space. In the case considered here, this shift arises by a virtual transition to an intermediate mode and a subsequent back transition. We can call this kind of process a return process. An inspection of Fig. 5.5 reveals that these return processes are not restricted to a virtual transition to the intermediate modes $|1\rangle$ and $|\bar{1}\rangle$. Instead, the system can transit to any of the modes that correspond with a nonzero Fourier components in the driving, indicated by red dots. Furthermore, by starting from one of the side modes, we obtain contributions of further return processes involving the modes $|\ell\, m\rangle$ that yield nonzero elements of $V^{\mathrm{II}}_{\pm 2\kappa+\ell,2+m}$. As a result, the contributions of all return processes nearly cancel each other and can be neglected in the calculation of the effective three-level Hamiltonian.

A non-negligible modification of the potential energy for each mode can arise from a possible detuning of the system from exact resonance. Since for the resonance $\omega = 1$, the initial mode couples to the side modes via the second harmonics in time, the potential energy shift between the side modes and the center mode is given by -2Δ, with $\Delta \equiv \omega - 1$.

Table 5.1 gives an overview of the effective parameters, $\Gamma_{\pm}$ and μ, that enter in the truncated three-level Hamiltonian, represented by the matrix (5.21). For all four resonances, we have control over the magnitude and phase of the coupling parameters via the parameters of the driving potential V^{II}. In particular, it is possible to tune one of the transition amplitudes to zero or to make them equal for both modes.

According to Section 2.3, the Rabi frequency for each resonance can be calculated analytically within the three-level description. Table 5.2 lists the functional dependence of the Rabi frequency Ω_{R} and the ratchet current $\bar{I}$ for each resonance of V^{II}, for the case of exact resonances ($\Delta = 0$). In agreement to the symmetry considerations, discussed below Eqs. (5.23), the ratchet current vanishes when α or β vanishes, or when the phases ϕ and ϑ approach the zeros of the cosine, given by $\frac{1}{2}\pi$ and $\frac{3}{2}\pi$. For all resonances, we obtain a linear dependence on K for the ratchet current in the limit $K \to 0$. For the resonance at $\omega = 1$, the Rabi frequency and ratchet current with nonzero detuning are given by

$$\Omega_{\mathrm{R}} = 4\left[K^4 + 4K^2\alpha^2\beta^2 + 64\Delta^2\right]^{\frac{1}{2}}, \tag{5.27a}$$

ω	Ω_{R}	$\bar{I}$
$\frac{1}{4}$	$\frac{K}{\sqrt{2}}\left[(\frac{4}{7}K\alpha)^2+\beta^2\right]^{1/2}$	$\frac{56K\alpha\beta\cos\vartheta\cos\phi}{7\beta^2+16(K\alpha)^2}$
$\frac{1}{2}$	$\frac{K}{\sqrt{2}}\left[1+(\frac{1}{10}K\alpha\beta)^2\right]^{1/2}$	$-\frac{10K\alpha\beta\cos\vartheta\cos\phi}{(K\alpha\beta)^2+100}$
1	$\frac{K}{2\sqrt{2}}\left[K^2+(2\alpha\beta)^2\right]^{1/2}$	$\frac{4K\alpha\beta\cos\vartheta\cos\phi}{K^2+(2\alpha\beta)^2}$
2	$\frac{K}{\sqrt{2}}\left[(\frac{1}{35}K\beta)^2+\alpha^2\right]^{1/2}$	$\frac{70K\alpha\beta\cos\vartheta\cos\phi}{(35\alpha)^2+(K\beta)^2}$

Table 5.2.: Analytic results for the Rabi frequencies and the continuously time-averaged ratchet currents for the four resonant frequencies considered.

$$\bar{I}=\frac{K^3\alpha\beta}{\Omega_{\mathrm{R}}^2}\cos\vartheta\cos\phi\ . \tag{5.27b}$$

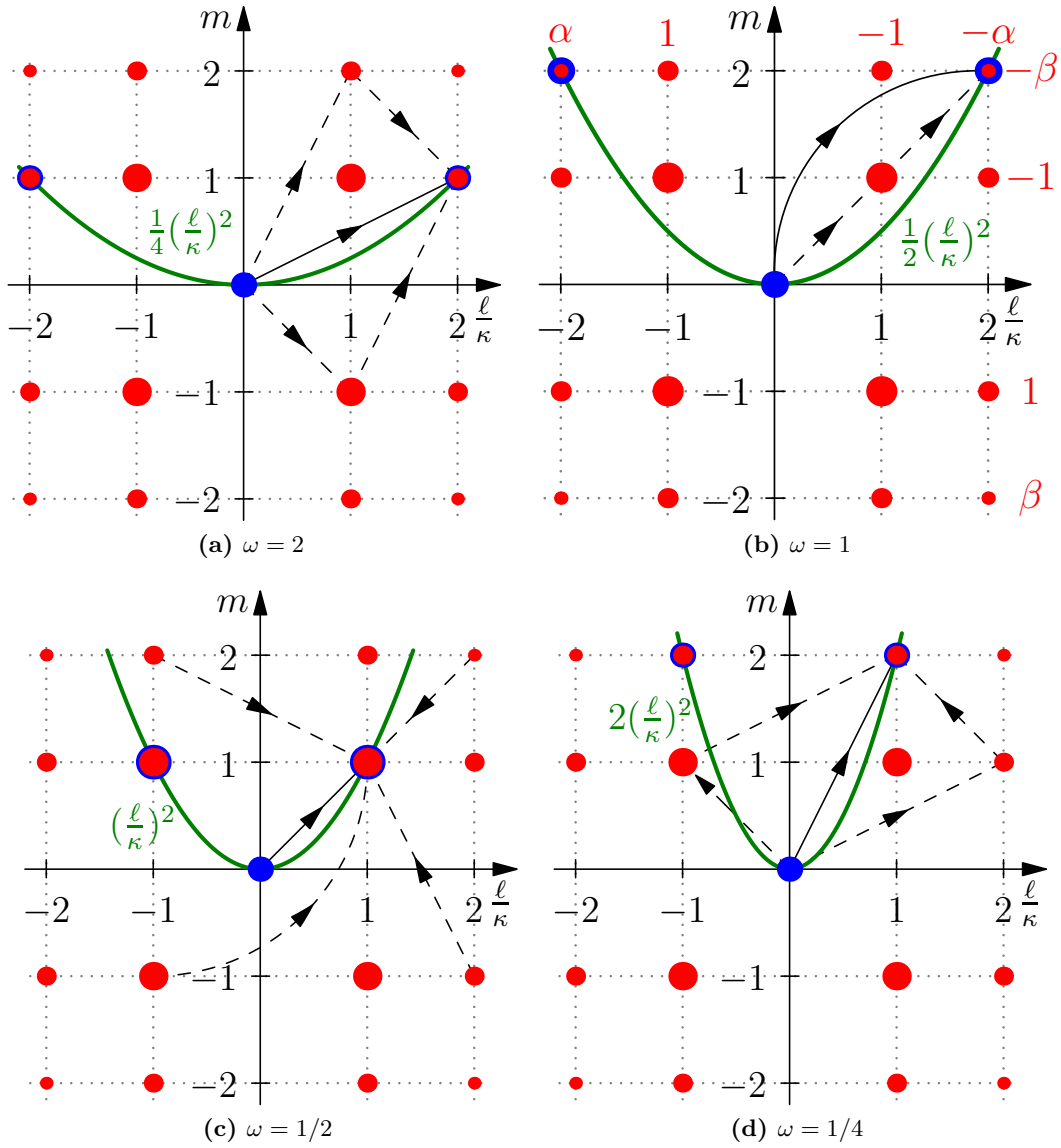

(a) $\omega = 2$ **(b)** $\omega = 1$

(c) $\omega = 1/2$ **(d)** $\omega = 1/4$

Figure 5.5.: *Graphical representation of the four main resonant cases of* V^{II}. The arrows indicate first (solid lines) and second (dashed lines) order contributions of the transition elements of the T-matrix for the transition to the positive angular momentum mode. The contributions of the transition to the opposite mode is not shown, but can be obtained by mirroring at the vertical axis. Negative driving frequencies $\omega < 0$ would yield a parabola that points downwards, and the related resonances are equivalent to the ones shown here. The size of the red dots reflects the absolute value of the respective Fourier component for $\alpha, \beta < 1$.

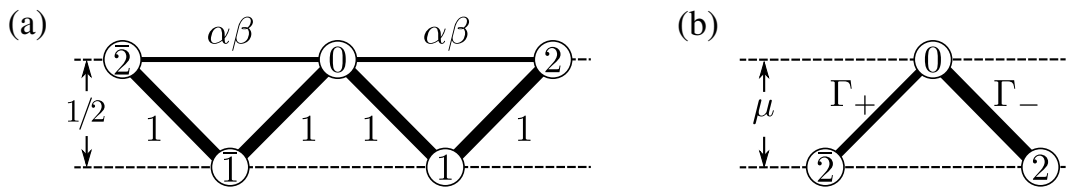

Figure 5.6.: *Few mode representation for the driving potential V^{II} for the resonance at $\omega = 1$.* (a) Representation of the few mode system, including the virtually visited modes $|1\rangle$ and $|\bar{1}\rangle$, which lie quasienergetically below the resonant modes by an amount of $\frac{1}{2}$. The numbers beneath the connecting lines are the magnitudes of the transition strengths. (b) Graphical representation without intermediate modes and effective coupling strengths.

5.6.2. Numerical study

The driving V^{II} involves a more complicated calculation to obtain the parameters of the truncated Hamiltonian $H_{3\mathrm{LS}}$, than for V^{I}. Therefore, we compare this approximation with a numerical solution of the full system, involving a large number of modes.

The single particle wave function is numerically integrated in time using a split-operator method[4], in each case checking that the time discretization, Δt, is sufficiently small to produce converged results. The size of Δt depends strongly on the amplitude K of the driving, with the surprising result that smaller values of K demand a much finer discretization to produce converged results. As an additional verification, results were also checked using a fourth-order Runge-Kutta technique.

The analysis of the previous section predicts that, in addition to the main resonance at $\omega = 1$, additional resonances for $\omega = 1/4$, $1/2$, and 2. To verify this prediction Fig. 5.7[5] shows the time-averaged current, obtained for a fixed driving strength of $K = 0.05$ as the frequency is varied over a wide range. We can first note that we indeed see peaks at the four resonant frequencies indicated by the resonance condition 5.15. A similar set of resonance peaks was observed in the experimental investigation of this ratchet [SKH+09], indicating that the periodic boundary conditions are a good model for the extended lattice, used in this experiment. The peak at $\omega = 1$ is considerably larger than the others, and it is interesting to note that the response for $\omega = 1/2$ is of opposite sign to the other peaks. This peak is also unusual in its sensitivity to the averaging procedure used; the stroboscopic result, given by

$$\bar{I}_{\mathrm{strob}}(t_0) = \lim_{\mathcal{N}\to\infty} \frac{1}{\mathcal{N}} \sum_n I(nT + t_0), \tag{5.28}$$

is larger and broader than the continuous time-average. Figure 5.7b shows an enlargement of the small-scale structure in the current response, which indicates the existence of further families of sub-resonant peaks, of much smaller magnitude than the four primary peaks, occurring at commensurate fractions of the driving frequencies. This indicates the role of higher order processes, which could in principle be described by a suitable generalization of the here presented procedure.

Figure 5.8a shows the agreement between the analytical prediction of the three-level model and the full numerical simulation for the time-dependent ratchet current in the weak coupling case ($K = 0.1$). In particular, this shows that the analytical predictions (5.27a) for the Rabi frequency and Eq.(5.27b) for the long-time ratchet current become essentially exact in the weak-driving limit. In both cases the exact dynamics features a fast oscillation, whose frequency is of the order of the driving frequency, and has already been observed in previous comparisons of a driven two-mode system – cf. Fig. 4.4. As expected, the agreement with the perturbative analytical calculation is worse for the higher value of K, see Fig. 5.8b.

In the strong driving limit the contributions of further modes, beyond those contained in the truncated three-level picture, become important and the dynamics is no more given by a simple Rabi oscillation. This limit was studied in Ref. [CS09], where it was shown that strong driving can yield an effective time-inversion asymmetry, which gives rise to long lasting transient ratchet currents.

The analytical predictions for the Rabi-frequency and the ratchet current, given in table 5.2, are compared with a numerical study in Figs. 5.9 and 5.10, respectively. We observe a good agreement for weak driving strengths, where the effective three-level

[4]The split-operator code for this calculation was implemented by Charles Creffield.
[5]The data for this figure was created by Charles Creffield.

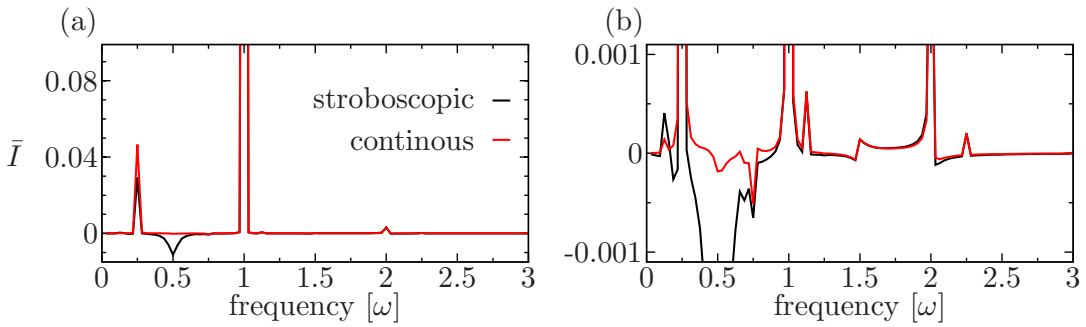

Figure 5.7.: Time-averaged current, averaged over 4000 driving periods plotted as a function of the driving frequency, for $K = 0.05$. The asymmetry parameters are $\alpha = \beta = 0.2$, and $\phi = \vartheta = 0$. Four peaks appear at $\omega = 1/4$, $1/2$, 1 and 2 in agreement with the resonant condition (5.15). (b) Magnified view, showing the existence of sub-resonances at commensurate fractions of the resonant frequencies. We also note the reduction of the resonance at $\omega = 1/2$ when the time-average is evaluated continuously instead of stroboscopically.

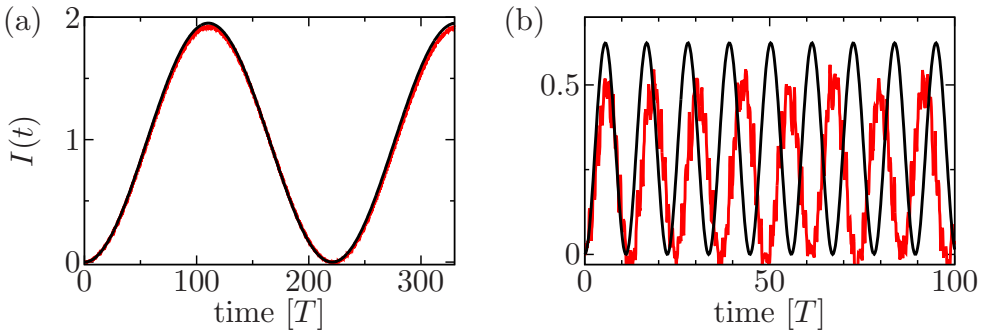

Figure 5.8.: Comparison of the time-dependent current, predicted by the effective three-level model and the exact numerical results. The exact resonance at $\omega = 1$ is considered. (a) For weak driving ($K = 0.1$) the three-level model predicts a Rabi oscillation which fits well the exact results, given by the blue curve. (b) For a stronger driving amplitude ($K = 0.5$) the high-frequency oscillations contribute stronger to the dynamics but the main behavior is still well-described by the effective model. Further values of the parameters are $\alpha = \beta = 0.2$, and $\phi = \vartheta = 0$.

model produces quantitatively accurate results. For higher driving strengths the model diverges from the exact results, as expected for a perturbative result.

Conclusions

We have studied two types of ratchet potentials, which give rise to an effective truncation of Hilbert space to three main modes. The components of the corresponding three-level Hamiltonian are either the *naked* matrix elements of the full Hamiltonian, or arise by an interference between first- and second-order processes in the driving. For the latter case, the predictions of the truncated picture, such as Rabi frequency or ratchet current, compare well to those of a full numerical solution of the underlying equation of motion. The mathematical analysis was supplemented by a graphical illustration of the resonance conditions and the basic processes which lead to a ratchet current. The analytical calculations, presented here, represent a novel type of application of the tt'-formalism.

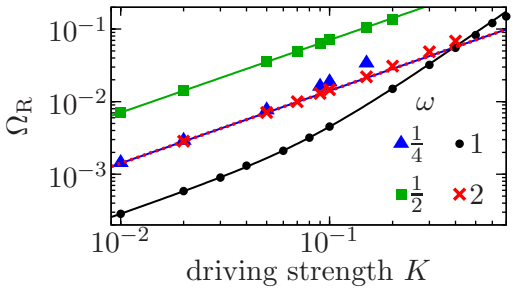

Figure 5.9: Rabi frequencies, Ω_R, predicted by the effective three-level model (see table 5.2) are shown with solid lines, to compare with data extracted from numerically exact simulations.

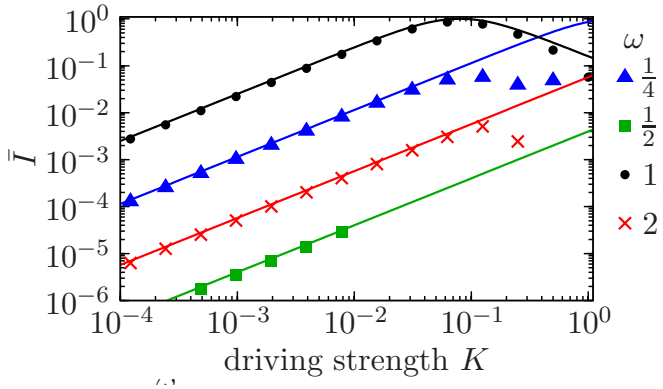

Figure 5.10.: *Ratchet current over driving strength.* Comparison of the analytical results with numerically exact data for the four principal resonances, $\omega = 1/4$, $1/2$, 1, and 2 (see table 5.2). The values for $\omega = \frac{1}{2}$ are actually negative. Therefore, their absolute value is displayed. For all the curves the parameters are $\alpha = \beta = 0.2$, and $\phi = \vartheta = 0$.

6. Particle interactions in Hamiltonian quantum ratchets

The concept of an orbital Josephson junction can be applied to study and understand the role of particle interactions in a Hamiltonian quantum ratchet of the type considered in Chapter 5. A central result is that the three-mode description remains valid for interacting particles and the Hamiltonian (5.21) can be translated to second quantization, including particle interactions. The resulting many-body Hamiltonian is that of a Josephson junction with three macroscopically occupied modes[1].

6.1. Many-body quantum systems

Understanding the role of particle interactions in quantum many-body systems out of equilibrium represents a challenging topic in current research. In the absence of interactions, a many-body system is correctly described with a single-particle picture. Even if the system is described by a statistical ensemble instead of a pure state, one can find a closed equation of motion for the single particle density matrix (SPDM)

$$\rho^{(1)}(\mathbf{x},\mathbf{x}';t) = \langle \hat{\psi}^\dagger(\mathbf{x},t)\hat{\psi}(\mathbf{x}',t)\rangle\,, \tag{6.1}$$

where $\langle\cdot\rangle$ denotes an average of the ensemble and $\hat{\psi}(\mathbf{x},t)$ is the field operator in the Heisenberg picture which was introduced in Section 3.4.2.

This changes drastically for interacting particles. Already the simplest case of pure two-body interactions gives rise to the so-called BBGKY hierarchy[2]. This is an infinite system of coupled equations of motion, in which the equation of motion of the n-particle density matrix, given by

$$\begin{aligned}\rho^{(n)}&(\mathbf{x}_1,\cdots,\mathbf{x}_n,\mathbf{x}_1',\cdots,\mathbf{x}_n';t)\\ &= \langle \hat{\psi}^\dagger(\mathbf{x}_1,t)\hat{\psi}^\dagger(\mathbf{x}_2,t)\cdots\hat{\psi}^\dagger(\mathbf{x}_n,t)\hat{\psi}(\mathbf{x}_1',t)\hat{\psi}(\mathbf{x}_2',t)\cdots\hat{\psi}(\mathbf{x}_n',t)\rangle\,,\end{aligned} \tag{6.2}$$

involves the $(n+1)$-particle density matrix. Accordingly, it is by no means sufficient to study a two-particle system in order to analyze the whole phenomenology of an interacting many-body system, since most of the phenomena in these systems will be emergent.

6.2. Interacting Bose gas on a ring

In Chapter 5 we studied the dynamics of a driven ideal Bose gas in a ring trap. Here, we will consider the same type of system, but now with nonzero particle interactions. The dynamics of an interacting Bose gas can be described by the Heisenberg equation of motion of bosonic field operators – see Section 3.4.2. For the case of a single degree

[1] This result is published for a specific type of ratchet potential in Ref. [HCCS12]. A publication presenting further possible potentials, as considered in this chapter, is in preparation [HHC+].

[2] Named after Bogolioubov, Born, Green, Kirkwood, and Yvon.

of freedom and periodic boundary conditions, Eq. (3.37) reads

$$i\partial_t\hat{\psi}(x,t) = [-\tfrac{1}{2}\partial_{xx} + V(x,t) + \lambda\hat{\psi}^\dagger(x,t)\hat{\psi}(x,t)]\hat{\psi}(x,t), \tag{6.3}$$

which is just the second quantized version of Eq. (5.1). The operators $\hat{\psi}(x,t)$ obey bosonic commutation relations, given in Eq. (3.36) and x is the remaining degree of freedom given by the angle along the circumference of the ring[3]. The strength of the contact interaction term is given by $\lambda = 8aR/r_\perp^2$, where a is the s-wave scattering length of the gas atoms and $r_\perp$ is the characteristic length of the perpendicular confinement, cf. Section 5.2.

6.3. Translation to tt'-formalism

The main goal of this section is to combine the results, obtained in previous chapters, to obtain a few-mode description for the interacting many-body system [Eq. (6.3)]. To be precise, we will apply the tt'-formalism for field operators, introduced in Chapter 3, in order to incorporate particle interactions in the few-mode description obtained in Chapter 5.

To this end, we translate Eq. (6.3) to the corresponding tt'-version (cf. Section 3.4.2):

$$\mathrm{i}\partial_t\hat{\psi}(x,t';t) = [-\tfrac{1}{2}\partial_{xx} - \mathrm{i}\partial_{t'} + V(x,t') + \lambda\hat{\psi}^\dagger(x,t';t)\hat{\psi}(x,t';t)]\hat{\psi}(x,t';t). \tag{6.4}$$

The commutation relations of the operators $\hat{\psi}(x,t';t)$ are given in Eq. (3.40).

We consider the particle interactions and the driving potential to be weak. This implies that the dominant terms of Eq. (6.4) are given by the kinetic energy term and the partial derivative with respect to t'. As for the single-particle case, the dynamics will be mainly governed by the eigenmodes of the unperturbed Floquet operator $\mathcal{H}_0$, see Eq. (5.9). Therefore we transform the operators of second quantization, $\hat{\psi}(x,t';t)$, to the discrete basis of the unperturbed Floquet states, cf. Eq. (5.10),

$$\hat{a}_{\ell m}(t) = \frac{1}{T}\iint dx\ dt'\phi^*_{\ell m}(x,t')\hat{\psi}(x,t';t)\ . \tag{6.5}$$

The commutation relations of the operators $\hat{a}_{\ell m}$ and $\hat{a}^\dagger_{\ell m}$ are given in Eq. (3.49).

The equation of motion for $\hat{a}_{\ell m}(t)$ can be obtained as special case of Eq. (4.11)

$$\begin{aligned} i\tfrac{\partial}{\partial t}\hat{a}_{\ell m}(t) = \varepsilon^0_{\ell m}\hat{a}_{\ell m}(t) + \sum_{\ell_1 m_1} V_{(\ell_1-\ell),(m_1-m)}\hat{a}_{\ell_1 m_1}(t) \\ + \frac{\lambda}{2\pi}\sum_{\ell_1\ell_2}\sum_{m_1 m_2}\hat{a}^\dagger_{\ell_1+\ell_2-\ell,m_1+m_2-m}(t)\hat{a}_{\ell_1 m_1}(t)\hat{a}_{\ell_2,m_2}(t), \end{aligned} \tag{6.6}$$

where we have used that the two-body matrix elements, defined in Eq. (4.12), for the angular momentum eigenstates $|\ell\rangle$ are of the simple form

$$w_{\ell_1\ell_2,\ell_3\ell_4} = \frac{1}{2\pi}\delta_{\ell_1+\ell_2,\ell_3+\ell_4}. \tag{6.7}$$

The next step will be to truncate Eq. (6.6) to a system equations that involves only the resonant modes.

[3] See Section 5.2 for a discussion of the units used here.

6.4. Truncated picture

As we are considering systems with weak particle interactions and weak driving, the set of modes which mainly contributes to the dynamics is dominated by the unperturbed single particle Floquet operator $\mathcal{H}_0$. Accordingly, the identification of these modes, as well as the calculation of the effective transition amplitudes among them, can be calculated within a single particle picture, which was considered in the previous chapter.

A further implication of the weak interaction strengths considered here, is that the energy eigenstates can be assumed to be fully condensed in one of the angular momentum eigenmodes. In the following, we consider the system to be initially condensed in the zero angular momentum eigenmode, which is the ground state of the undriven single particle part of the Hamiltonian. Furthermore, we focus on those cases in which the driving potential V induces a coupling among the initial zero angular momentum mode $|0\rangle$ and two side modes $|\pm\rangle$ with mutually opposed momenta of same magnitude. The potentials V^{I} and V^{II} from the previous chapter are examples of such driving potentials. Just as for the case of two main modes (see Chapter 4), we drop the index m for the specification of the modes since, in this truncated picture, the value of m follows from the knowledge of the quantum number ℓ.

A truncation of Eq. (6.6) to the set of modes $\{-,0,+\}$ yields the system of equations

$$\mathrm{i}\partial_t \hat{a}_- = -\mu + \Gamma_-^* \hat{a}_0 + \frac{\lambda}{2\pi}(2\hat{a}_+^\dagger \hat{a}_+ \hat{a}_- + 2\hat{a}_0^\dagger \hat{a}_0 \hat{a}_- + \hat{a}_-^\dagger \hat{a}_- \hat{a}_-), \tag{6.8a}$$

$$\mathrm{i}\partial_t \hat{a}_0 = \Gamma_+ \hat{a}_+ + \Gamma_- \hat{a}_- + \frac{\lambda}{2\pi}(2\hat{a}_+^\dagger \hat{a}_+ \hat{a}_0 + \hat{a}_0^\dagger \hat{a}_0 \hat{a}_0 + 2\hat{a}_-^\dagger \hat{a}_- \hat{a}_0), \text{ and} \tag{6.8b}$$

$$\mathrm{i}\partial_t \hat{a}_+ = -\mu + \Gamma_+^* \hat{a}_0 + \frac{\lambda}{2\pi}(\hat{a}_+^\dagger \hat{a}_+ \hat{a}_+ + 2\hat{a}_0^\dagger \hat{a}_0 \hat{a}_+ + 2\hat{a}_-^\dagger \hat{a}_- \hat{a}_+)\,, \tag{6.8c}$$

where the parameters μ and $\Gamma_\pm$ depend on the parameters of the driving potential and on the resonance to be considered. The calculation of these parameters have been presented in Chapter 5 for two types of driving potential.

In complete analogy to the case of two levels, the commutation relations (3.49) become standard bosonic commutation relations with the truncation to the three levels, i.e.

$$[\hat{a}_\mu^\dagger, \hat{a}_\nu] = \delta_{\mu\nu}, \text{ and} \tag{6.9a}$$

$$[\hat{a}_\mu^\dagger, \hat{a}_\nu^\dagger] = [\hat{a}_\mu, \hat{a}_\nu] = 0 \text{ for } \nu, \mu \in \{-,0,+\}. \tag{6.9b}$$

Furthermore, Eq. (6.8) can be regarded as Heisenberg equation of motion, arising from the three-level system Hamiltonian

$$\hat{H}_{3\mathrm{LS}} = \Gamma_+ \hat{a}_0 \hat{a}_+^\dagger + \Gamma_- \hat{a}_0 \hat{a}_-^\dagger + \mathrm{h.c.} + \mu(\hat{n}_+ + \hat{n}_-) - \frac{\lambda}{4\pi}\sum_\nu \hat{n}_\nu(\hat{n}_\nu - 1) - \frac{\lambda}{2\pi}\left(\hat{N}^2 - \hat{N}\right), \tag{6.10}$$

where $\hat{n}_\nu \equiv \hat{a}_\nu^\dagger \hat{a}_\nu$ is the occupation number operator of the mode ν, and $\hat{N} = \sum_{\nu\in\{-,0,+\}} \hat{n}_\nu$ is the total particle number operator within the truncated space. We will focus on systems with conserved total particle number. This means the term $-\lambda\left(\hat{N}^2 - \hat{N}\right)/2\pi$ has no influence on the dynamics, and can be omitted.

The prefactor in the interaction term is independent of the specific driving potential, of the considered resonance, and of the wave number of the participating modes.

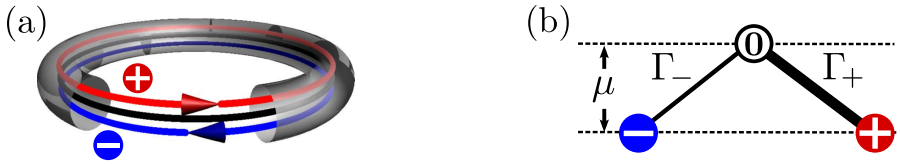

Figure 6.1.: *Schematic illustration of system setup and effective model.* (a) An external driving potential induces a coupling between the initial mode (black line) and two opposite angular momentum eigenstates (red and blue line). (b) The effective description is that of two adjacent Josephson links – cf. Hamiltonian (6.10).

6.5. Dynamical regimes

Bosonic Josephson junctions with two modes are known to feature two qualitatively different types of dynamics, depending on the interaction strength. Bosonic three-mode systems have a much richer set of dynamical regimes. Here, we will introduce three main regimes that can be observed, two of which can also be observed in a two-mode system. The main dynamical regimes are:

1. *Rabi oscillations* are expected to occur for weak particle interactions $g \ll \Omega_{\mathrm{R}} = \sqrt{4\Gamma^2 + \mu^2}$, where $g = \lambda(N-1)$ is the mean-field interaction strength, and $\Gamma^2 = |\Gamma_+|^2 + |\Gamma_-|^2$. The condensate oscillates between the initial mode $|0\rangle$ and a superposition of the side modes given by $|a\rangle \propto \Gamma_+ |+\rangle + \Gamma_- |-\rangle$ with a frequency close to Ω_{R} – cf. Section 2.3. This regime was basically considered in Chapter 5.

2. *Chaotic dynamics* are expected for intermediate particle interaction strengths. In this regime the dynamics cannot any more be described as an oscillation between $|0\rangle$ and $|a\rangle$. A third state is involved and a positive maximal Lyapunov exponent is observed within the mean-field approximation. Chaotic dynamics cannot occur for a two-mode system ($\Gamma_+ = 0$ or $\Gamma_- = 0$), nor for symmetric coupling ($\Gamma_+ = \Gamma_-$) because the dimension of the effective phase space would be too low in these cases [Sch88].

3. *Self-trapping* occurs when the particle interaction dominates the dynamics. In this case the condensate cannot *leave* the initial mode because it would lose more interaction energy than can be compensated by the single-particle part of the Hamiltonian [SFGS97][4]. Note that the total quasi-energy is conserved in this system. The critical interaction strength for the occurrence of self-trapping is

$$g_c = 8\pi \max(|\Gamma_+|, |\Gamma_-|). \tag{6.11}$$

   This prediction of the critical interaction strength for the self-trapping transition is based on the observation that for interaction strengths close to but below g_c ($g \lesssim g_c$) the system is partially trapped in the subsystem consisting of the center mode and the side mode with the strongest coupling. This phenomenon of partial self-trapping will be discussed more deeply in Chapter 7.

In Chapter 7, we will have a closer look on these systems and introduce two further types of dynamics that can be found in a bosonic three-level system.

[4] For a symmetric two-mode system (either $\Gamma_+ = 0$ or $\Gamma_- = 0$) the condensate can still tunnel tunnel to the other mode, but tunneling times become exponentially large.

6.6. Numerical cross-check

An effective description in terms of a BJJ is not guaranteed to always withstand a comparison with an exact simulation of the full system. For example for a BEC in a one dimensional double-well trap, the related two-mode description has been proven to be invalid near and in the regime where the two-mode model predicts self-trapping [SSAC09], although common criteria for the validity of the two-mode description were met. In the following, we present a numerical check where the results, obtained with the truncated three-mode description as OJE are compared to the full dynamics of the system. Such a comparison is done for both driving potentials introduced in Chapter 5. The dynamics under the driving potential V^{I} are solved numerically on a full many-body level, while for V^{II} particle interactions will be taken into account within the GP approximation.

6.7. Ellipsoidal driving

The coupling parameters $\Gamma_{\pm}$ for the ellipsoidal driving potential V^{I}, defined in Eq. (5.17) are given in Eq. (5.21). An advantage of the driving potential V^{I} over V^{II} is that it rules out possible effects of intermediate modes, as those involved in the perturbative calculation for V^{II}. Hence, the ellipsoidal driving allows us to focus solely on the interplay between interaction and truncated picture.

6.7.1. Methods and parameter regimes

The numerical solution of the full many-body dynamics (FMB) is done with the so-called multi-configurational time-dependent Hartree for bosons (MCTDHB)[5] algorithm [MMR05, ASC08, HB11]. This method allows us to go systematically beyond a mean-field approximation by permitting a variable number M of orbitals to be macroscopically occupied. It is particularly suitable for the study of Bose systems with a handful of macroscopically occupied modes. The related many-body dynamics of the three-level description (3LS), characterized by the Hamiltonian (6.10), is solved numerically via an exact diagonalization routine.

For the simulations presented here we choose $\kappa = 1$. This allows the use of a relatively small single-particle basis for the FMB simulations (based on MCTDHB). The overall driving amplitude is chosen to be $K = 0.1$, such that the effective description can be assumed to be valid. The amplitude K should not be chosen too small either, since this would decrease the related Rabi-frequency and one would have to simulate, or perform experiments, over very long times in order to see a single Rabi cycle. As driving frequency, we choose the resonant frequency $\omega = 0.5$ for $\kappa = 1$, without detuning ($\Delta = 0$). For the amplitudes of the constituent plane waves of the driving we choose $K_+ = 0.07$, $K_- = 0.03$, and the phases $\varphi\pm = 0$. With this asymmetry all dynamical regimes mentioned in Section 6.5 can be observed. We consider total particle numbers up to $N = 40$.

According to Eq. (6.11), the critical mean-field interaction strength for the self-trapping transition is $g_c \approx 0.88$. We will consider four different values of g, referring to qualitatively different dynamics: Rabi oscillations ($g = 0.1$), chaos ($g = 0.5$), dynamics near the critical point ($g = 0.9$), and self-trapped dynamics ($g = 1.5$).

An initial condensate depletion due to particle interactions is discarded within 3LS. Accordingly, we expect 3LS to work better in the limit of high particle numbers and small interaction strength λ. With the FMB simulations, we can analyze possible effects

[5] The MCTDHB simulations were performed by David Hochstuhl.

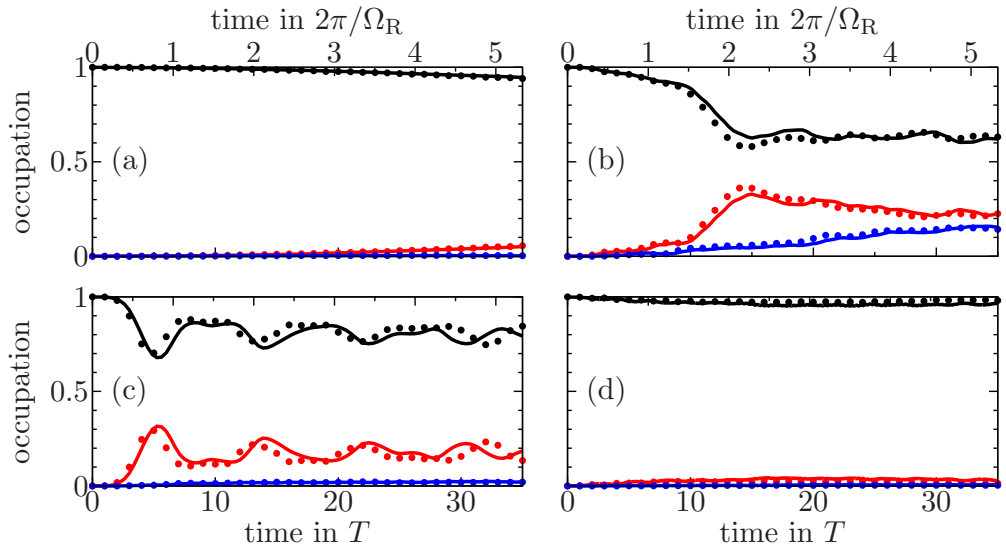

Figure 6.2.: *Occupation of natural orbitals.* The solid lines show FMB results, and the points refer to results obtained within 3LS. Four different interaction strengths, which refer to qualitatively different types of dynamics, are considered: (a) Rabi-regime ($g = 0.1$), (b) chaos ($g = 0.5$), (c) dynamics close to the critical interaction strength $g = 0.9$, and (d) self-trapped dynamics ($g = 1.5$). Further parameters are: $N = 40$, $K_+ = 0.07$, $K_- = 0.03$, $\varphi_\pm = 0$, $\kappa = 1$, $\omega = 0.5$. The upper horizontal axis reflects the relevant time-scale within 3LS, given by the Rabi period $T_R = 2\pi/\Omega_R$.

that originate in the initial depletion due to particle interactions. The FMB simulations presented in the following use the ground state of the initial static Hamiltonian as initial state, including particle interactions. Consequently, the initial state of the full system is depleted to some extent. This is a realistic choice as initial state, since it can be experimentally obtained by cooling of an interacting Bose gas. For $N = 40$ particles the initial depletion for the considered interaction strengths stays below $1.4 \cdot 10^{-3}$ which is reached for $g = 1.5$.

6.7.2. Simulation results

Figures 6.2 and 6.3 show a comparison of the dynamics obtained with FMB and with 3LS over a time range of 35 driving cycles. This corresponds more than five Rabi cycles. A first observation is that the fast oscillatory onset, which becomes obvious for the driven two-mode system, see Fig. 4.4, is nearly invisible in this case.

Figure 6.2 shows the normalized occupation numbers of the natural orbitals over time. Natural orbitals are the eigenstates of the SPDM, defined in Eq. (6.1). The highest occupied orbital is the condensate orbital. If more than one orbital is macroscopically occupied the condensate is said to be fragmented [SS99]. For a normalized condensate occupation close to 1 the system can be well described by the GP equation.

For the extreme cases of weak particle interactions ($g = 0.1$), shown in Fig. 6.2a, and strong interactions ($g = 1.5$), see Fig. 6.2d, the system remains condensed during the depicted time range. For the case of weak particle interactions this is not surprising, since in the limit of zero particle interactions the system remains fully condensed for all times. In both cases the depletion reaches a maximal value of about 5%. For the values of g in between these extreme cases (Fig. 6.2bc) the dynamics is more complex and real many-body effects gain importance. For the intermediate interaction strengths,

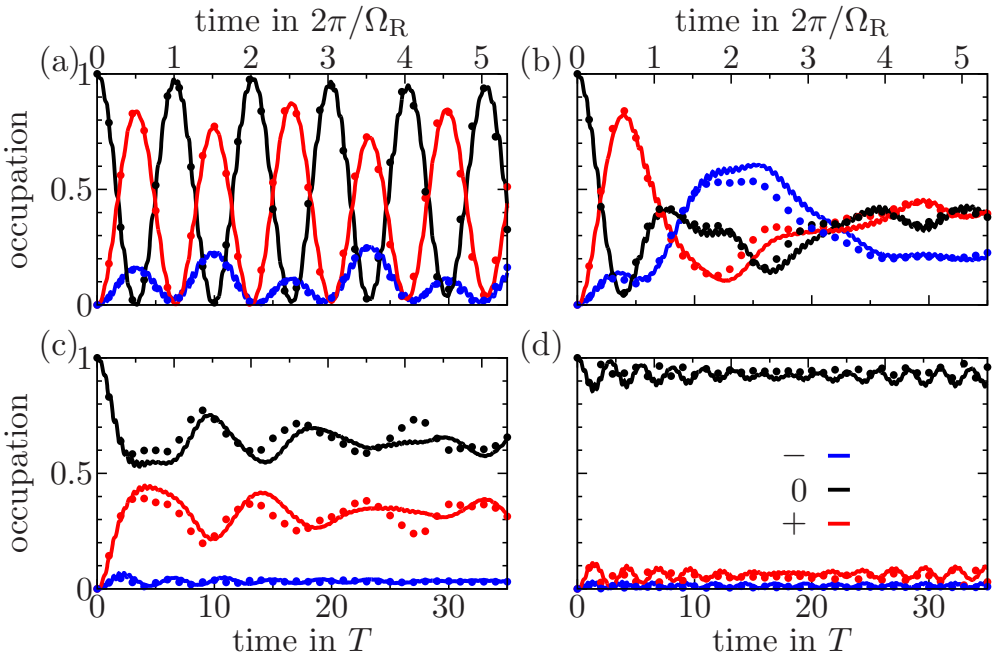

Figure 6.3.: *Comparison of full dynamics with effective description.* The graphs show the normalized occupation numbers of the main modes $(-, 0, +)$ over time. Solid lines refer to the FMB dynamics and points refer to 3LS. The parameters and dynamical regimes are the same as in Fig. 6.2.

considered in Figs. 6.2bc, a second orbital becomes macroscopically occupied by an amount of up to 30%. In these cases, a mean-field treatment would fail. For $g = 0.5$ the maximal Lyapunov exponent, calculated within GP for the three-level description (3GP) is $\lambda_M \approx 0.5\Omega_R$[6]. The failure of GP in those dynamical regimes, where GP predicts chaotic dynamics was first discussed by Castin and Dum [CD97], and has recently been reconsidered [vCL+11, vLS+12, HCCS12]. In Chapter 7 we will have a closer look on the chaotic dynamics within 3LS. In all cases the occupation numbers predicted by 3LS agree well with the FMB results. To be precise, the absolute differences in both results between the normalized occupation numbers are below 0.1 for the considered values of g.

The effective description, 3LS, works best for weak particle interactions – see Fig. 6.2a and 6.3a. This implies that for the ellipsoidal driving, a coupling to modes outside the three-level description, is mainly induced by the interaction term of the full Hamiltonian. On the other hand, the discrepancies between both descriptions do not increase monotonically with an increase of g. The strongest discrepancies are found for the intermediate interaction strengths. For $g = 0.5$ ($g = 0.9$) the occupation of the center mode deviates by an amount of up to 0.09 (0.1).

Figure 6.4 shows the occupation number of the outer modes, i.e. those modes that lie outside the three-level Hilbert space spanned by $|-\rangle$, $|0\rangle$, and $|+\rangle$. This quantity is defined as

$$\sigma_3 \equiv \sum_{\ell \neq -1,0,1} \langle \psi(t) | a_\ell^\dagger a_\ell | \psi(t) \rangle \,. \tag{6.12}$$

Three different particle numbers ($N = 20$, 30, 40) and the mean-field limit is considered. Fig. 6.4 shows that the relative participation of outer modes is stable with respect to

[6]For details on the calculation of the maximal Lyapunov exponent see Appendix A.

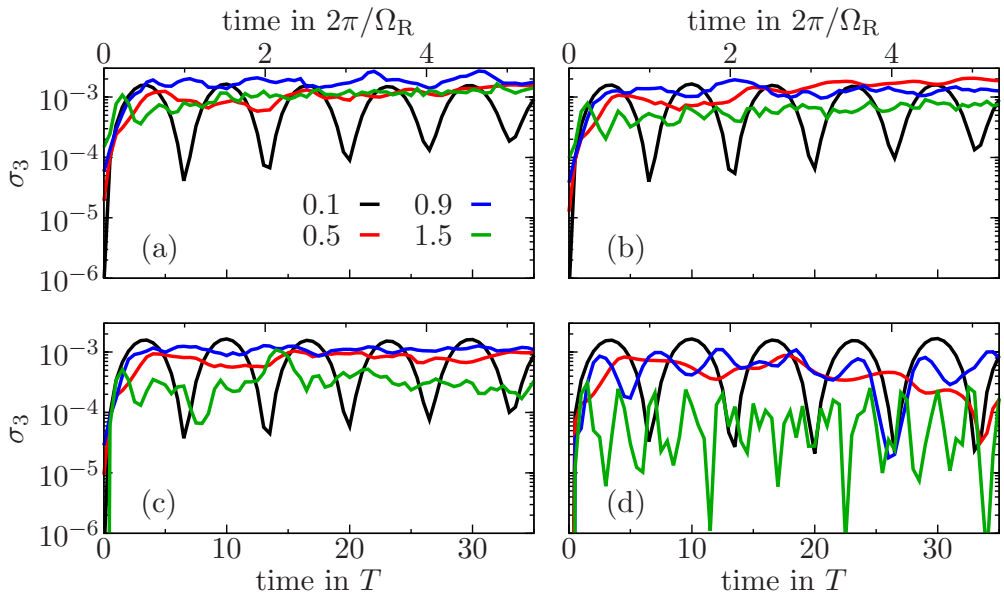

Figure 6.4.: *Contribution of outer modes.* Shown is the quantity σ_3, defined in Eq. (6.12), for various mean-field interaction strengths (see key) and total particle numbers: (a) $N = 20$, (b) $N = 30$, (c) $N = 40$, (d) mean-field.

a variation of the total particle number. Furthermore, we see that GP can provide information about the relative participation of outer modes. A clear trend of an increase of the participation of outer modes in time cannot be distinguished. The value of σ_3 seems to reach a saturated value after less than one Rabi period and the dynamics has a fluctuation onset after reaching saturation. In the self-trapping regime, GP clearly underestimates the contribution of outer modes to the dynamics.

Additionally, FMB simulations with a fully condensed initial state in the $k = 0$ mode have been performed. This way it is possible to detect whether some of the observed discrepancies between the effective description and the full dynamics can be assigned to the depletion which is present in the initial state of the FMB calculation, and would be present in a realistic experiment. For all considered interaction strengths the discrepancies between the 3LS and the full dynamics exceed the discrepancies observed between the two versions of the full many-body simulations (with and without initial depletion). This suggests that initial depletion of the condensate plays a minor role in the comparison presented here.

Figure 6.5 shows the same comparison as in Figs. 6.2 and 6.3, but with a weaker driving (halved values of $K_\pm$) and for only one dynamical regime. The interaction strength is $g = 0.25$, such that the dynamics is completely analogous to the chaotic case, shown in Figs 6.2b and 6.3b. It shows that in this case both descriptions approach each other for smaller values of the driving amplitude. Note further that the time range in Fig. 6.5 has doubled, compared to Figs. 6.2 and 6.3. It shows that both descriptions approach each other for smaller values of the driving amplitude. For example, the difference in the occupation of the center mode between 3LS and FMB after three Rabi periods amounts to 0.1 for $K = 0.1$ and for $K = 0.05$ it has decreased to 0.05.

Figure 6.6 shows the instantaneous overall current per particle

$$I(t) \equiv -i \int dx \, \langle \psi(t) | \hat{\psi}^\dagger(x) \partial_x \hat{\psi}(x) | \psi(t) \rangle \, / N, \tag{6.13}$$

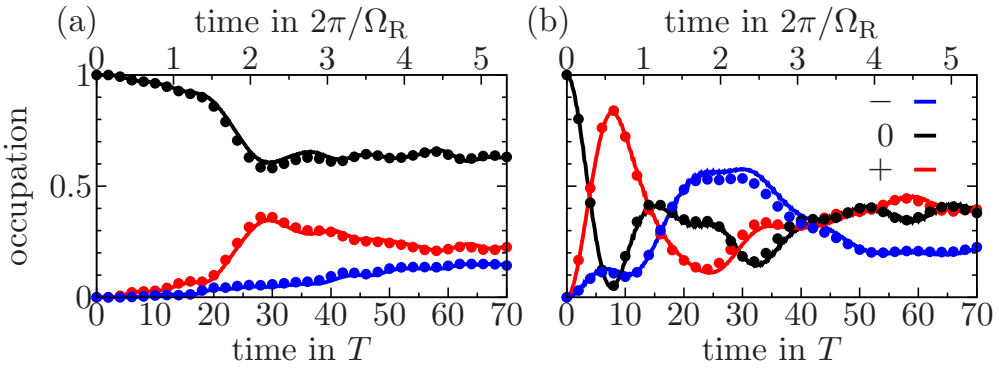

Figure 6.5.: *Comparison of effective description and full dynamics with weaker driving amplitude.* Shown is (a) the time-evolution of the normalized occupation numbers of the natural orbitals and (b) the occupation of the main modes $(-, 0, +)$. Points refer to effective description and the solid lines show the full many-body dynamics. Parameters: $K_+ = 0.035$, $K_- = 0.015$, $g = 0.025$, $N = 40$. This parameter set corresponds to a chaotic motion analog to those in Figs. 6.2b and 6.3b. The unmentioned parameters are the same as in Fig. 6.2.

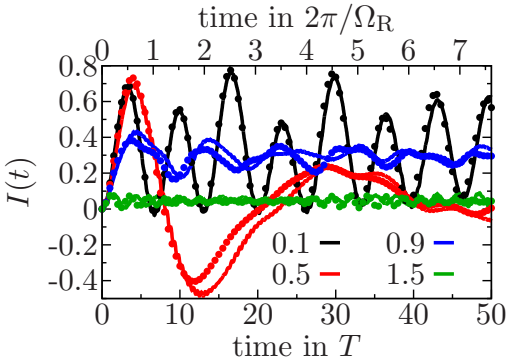

Figure 6.6: *Instantaneous particle current over time.* Solid lines refer to FMB results and dots refer to 3LS. The key indicates the considered mean-field interaction strengths g. The parameters are the same as in Fig. 6.2.

during 50 driving cycles. For the unstable cases ($g = 0.5$ and $g = 0.9$) the discrepancies among 3LS and FMB become quite large at certain times, e.g. for $g = 0.5$ the two description deviate by about 40% after $15T$; but both curves revert to a well agreement at about $35T$. The chaotic case is the only one, in which the value of the ratchet current becomes notably inverted.

6.7.3. Convergence analysis

Within MCTDHB the maximal number of natural orbitals that are taken into account is controlled via the parameter M, which plays a central role in this approximation. Therefore, it is sometimes given directly in brackets in order to clarify that one refers to the MCTDHB algorithm with respect to a certain choice of M, i.e. MCTDHB(M). For $M = 1$ the GP approximation is obtained; $M = 2$ allows the description of a condensate that is fragmented into two orbitals, and so on. In other words, M is the maximal number of nonzero eigenvalues of the SPDM. The value of M has to be chosen sufficiently high in order to obtain converged results. The FMB simulations presented here refer to $M = 4$. The convergence was checked in two ways:

1. A small occupation number of the M^{th} orbital indicates that the system is already well described. By definition, the $(M+1)^{\text{th}}$ natural orbital is unoccupied within MCTDHB(M). Setting the occupation number n_M of the M^{th} natural orbital to

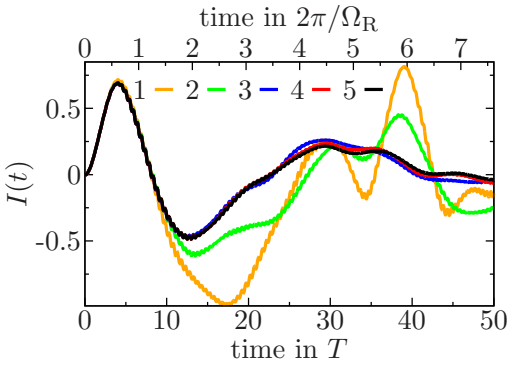

Figure 6.7: *Convergence analysis of the MCTDHB simulations.* The curves show the instantaneous particle current over time for various values of M. The system parameters are the same as in Fig. 6.2b (chaotic motion).

zero (e.g. by decreasing the value of M) changes the expectation value of a single-particle operator O by less than $n_M \|O\|_{\mathrm{op}}$, where $\|O\|_{\mathrm{op}}$ denotes the operator norm of O [Ric78]. Therefore, n_M/N may serve as a first estimate for the relative error made by MCTDHB(M). For $N = 40$ and $M = 4$ the normalized occupation of the fourth natural orbital stays below $1.2 \cdot 10^{-3}$ during the considered time range, for all shown interaction strengths.

2. A comparison with the results obtained with an incremented M (here $M = 5$) is probably the safest way to check whether the simulation is converged. However, it is not the most efficient way. For $N = 40$ and $M = 4$ the occupation of the condensate orbital changes by less than 5% when M is increased to $M = 5$, for all considered values of g. Fig. 6.7 shows the instantaneous particle current for values of $M = 1, \ldots, 5$. The difference in the value of the current between the $M = 4$ and the $M = 5$ stays below 0.06 for the considered time range.

Further parameters that have to be chosen properly to obtain converged results are the number of single-particle basis functions, and the tolerances for the adaptive-step size integrator used in the MCTDHB code. The results are obtained using a basis of angular momentum eigenmodes ranging from $k = -4$ to $k = 4$. The normalized occupation of the angular momentum modes ($k = \pm 4$) is below $5 \cdot 10^{-6}$ during the considered time range, for all values of g. This implies that for the precision of the results, given in this section, the contribution of the modes $|\pm 4\rangle$ is already vanishing small. Convergence with respect to the time step adaption has also been checked for selected parameter sets.

6.8. Factorizable driving

In this section, we will check the effective three-level description that corresponds to the driving potential V^{II} [see Eq. (5.23)] against a numerical solution of the full dynamics. Note that the calculation of the effective parameters of the three-level Hamiltonian is qualitatively different for the driving potential V^{II} than for V^{I}, since it involves a perturbative calculation up to second order in K. We expect the observation of the same dynamical regimes as have been discussed in Section 6.5 and observed in Section 6.7, since the truncated picture is equivalent.

6.8.1. Methods and parameter regimes

For this system three different approximations to investigate the dynamics are employed: full numerical solution of the time-dependent Gross-Pitaevskii equation (FGP) using a fourth-order Runge-Kutta method with a fixed time-step; study of the GP equation in

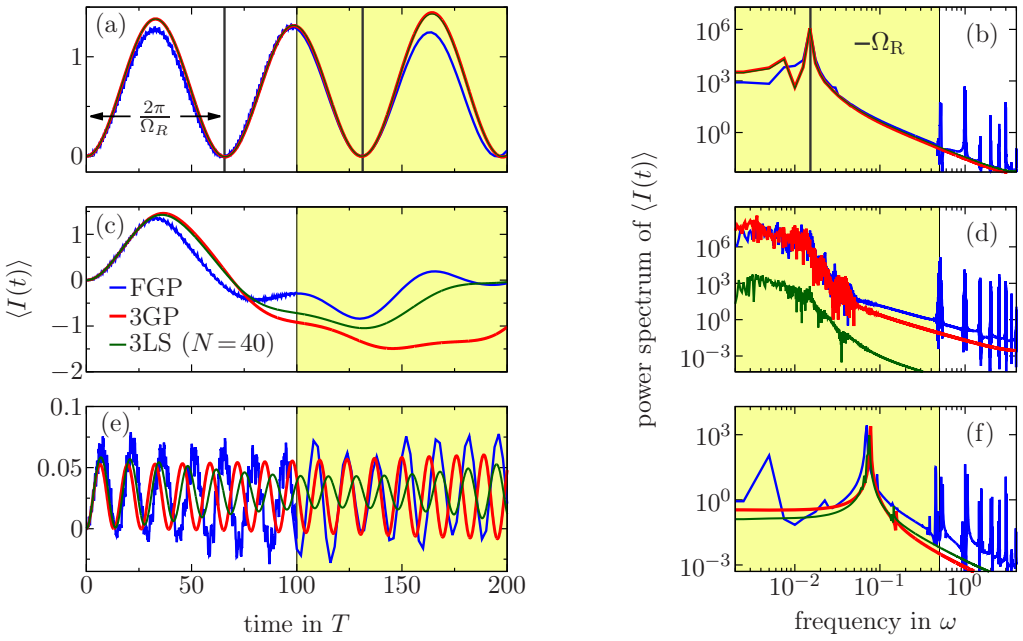

Figure 6.8.: *Time evolution and power spectrum of the particle current.* Three regimes are depicted: (a,b) weak interaction strength ($g=0.01$), showing regular Rabi oscillations; (c,d) intermediate interaction ($g=0.08$), displaying chaotic dynamics; and (e,f) strong interaction ($g=0.5$), showing self-trapping. Parameters: $K = 0.2$, $\varphi = 0$, $\omega = 1$ ($\Delta = 0$), $\alpha = \beta = 0.2$. The shaded region shows the stroboscopic current, which erases the short time dynamics responsible for the peaks in the white region of the current spectrum. In (a,b) the green curve almost coincides with the red curve.

the truncated space of the three resonant states $0, \pm$ (3GP); and solution of the many-body problem in the three-level system (3LS), via exact diagonalization of the effective interacting Hamiltonian (6.10) with up to 40 atoms. Note that 3GP can be obtained both as a truncation of FGP or a mean-field version of 3LS.

For all numerical simulations, presented in the following, we consider the value $K = 0.2$ for the driving amplitude and the asymmetry parameters are chosen to $\alpha = \beta = 0.2$ and $\varphi = \vartheta = 0$. The first results presented we refer to the case of exact resonance $\Delta = 0$. The effect of detuning is studied further below in this section. This parameter set yields a Rabi period of about 67 driving cycles. Note that for ellipsoidal driving the number of driving cycles contained in a single Rabi period was about ten times smaller, although the overall amplitude K was even smaller in this case. As for the ellipsoidal driving, for smaller driving amplitudes one obtains better agreement among both descriptions but one has to simulate over longer times in order to see a single Rabi oscillation.

Figure 6.8 shows the expectation value of the instantaneous ratchet current $I(t)$, defined in Eq. (6.13) over the first 200 driving cycles. The regimes of weak, moderate, and strong interaction, characterized by $g \equiv \lambda(N-1)$, are all calculated with the three methods described above. For weak interactions, the two truncated-space calculations (3GP and 3LS) yield similar Rabi oscillations, both differing from FGP in that they do not display high-frequency dynamics, which is stronger in this case as for ellipsoidal driving (V^{I}). The Fourier spectrum in Fig. 6.8 emphasizes clearly the separation of time scales in the time dependence of the current. The fast dynamics of FGP disappears if the stroboscopic current is plotted, as shown in the shaded region.

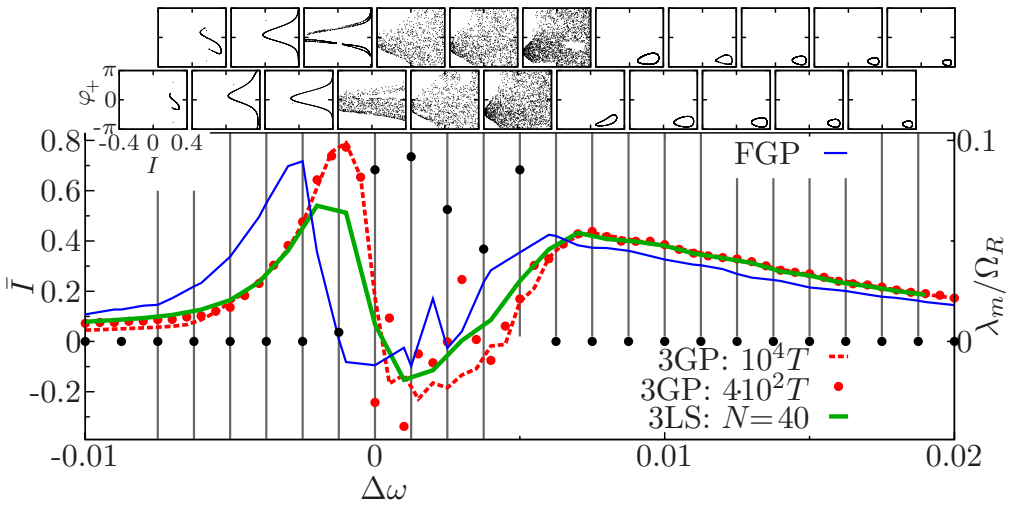

Figure 6.9.: *Ratchet current as a function of the detuning* Δ. Shown are four different calculations (3GP is computed at two different times, $400T$ and 10^4T). The black dots show the maximal Lyapunov exponents and refer to the scale on the right (Ω_R is the Rabi frequency). Poincaré sections are shown for the values of Δ marked with horizontal gray lines. They are obtained from points in the hyperplane $n_+ + n_- = 0.2$. The plotted variables are the instantaneous ratchet current $\langle I \rangle$ and the relative phase φ_+ between states $|0\rangle$ and $|+\rangle$. Parameters are: $\alpha = \beta = 0.2$, $K = 0.2$, $\varphi = 0$. In (a-b) averages are performed over 400 cycles unless otherwise indicated.

For strong interactions, the system is trapped in the initial state. The three numerical methods predict differing behaviors of the resulting small current, but agree on the position and strength of the main peak in the spectrum. For intermediate interaction, discrepancies between the three methods soon appear, which suggests chaotic behavior. This is confirmed and studied further below.

Within the accuracy limited by the ω-sampling, the positions of the main peaks coincide exactly in the Rabi regime, and vary by about 10% in the self-trapping case. The peak heights vary by about 6% in the Rabi case, and about 9% between FGP and 3GP in the the self-trapped regime. However for 3LS, the discrepancy with FGP (and 3GP) is worse (differing by a factor of 3), which coincides with the observation that for the self-trapped dynamics one has to consider particle numbers far beyond $N = 40$ in order to get an agreement between the full many-body description and the mean-field result [MCWW97].

6.8.2. Effect of detuning

Figure 6.9 shows a plot of the time-averaged ratchet current $\bar{I}$ as a function of the detuning Δ for $g = 0.1$. The results are obtained with the three different calculation methods described before. A calculation of the maximal Lyapunov exponent λ_M (given by black dots in Fig. 6.9), reveals a correlation between the emergence of chaotic behavior and reduction of ratchet current, as λ_M acquires positive finite values there. The Poincaré sections, given in the upper part of Fig. 6.9 become spread out for chaotic motion and serve as a further evidence of chaos. Further details are discussed in Chapter 7 and appendix A.

An obvious discrepancy between the curves obtained with FGP and 3GP is a shift by a

detuning offset of about $1.3 \cdot 10^{-3}$. This shift could be corrected to some extent by including further processes in the calculation of the effective three-level Hamiltonian (6.10), presented in Section 5.6.

Figure 6.9 also indicates that in the chaotic regime the convergence in time is slower than in the regular regime, as can be seen by the discrepancy between 3GP calculations performed over 400 or 10^4 driving periods. It was checked that the current reversal feature in the chaotic region is not just a transient, but reflects a lasting behavior; it was checked with up to 10^5 periods in some cases.

6.8.3. Contribution of outer modes

So far, we have checked the validity of the three-level description by comparing the time-evolution of observables, computed with the full and the effective description. In addition to such comparisons, we can consider the time-averaged contribution of those modes that lie outside the truncated Hilbert space, i.e.

$$\bar{\sigma}_3 = \frac{1}{\tau}\int_0^\tau dt \sum_{\ell\neq -2,0,2} |\,\langle\psi(t)|\ell\rangle\,|^2. \tag{6.14}$$

The calculation was done in FGP, which includes a large number of modes. Note that $\bar{\sigma}_3$ is not calculated within the framework of tt'-formalism, which means that for this calculation we integrate out the quantum number m, associated with the t'-dependence in the extended Hilbert space.

A natural question to ask is how much of σ_3 comes from a contribution of the intermediate modes $|1\rangle$ and $|\bar{1}\rangle$ (cf. Section 5.6), which are involved in the calculation of the effective three-level Hamiltonian. This can be obtained by a comparison of σ_3 and its analog involving also the intermediate modes:

$$\bar{\sigma}_5 = \frac{1}{\tau}\int_0^\tau dt \sum_{\ell\neq -2,\ldots,2} |\,\langle\psi(t)|\ell\rangle\,|^2, \tag{6.15}$$

which is also calculated within FGP (same as σ_3).

Figure 6.10 shows both measures as functions of the mean-field interaction g and the amplitude K of the driving, calculated over a time range of $400T$. A first observation is that the contribution of outer modes becomes more significant for larger values of K. This result is expected, since the three-level description is meant to be an approximation for weakly driven systems. Equipotential lines are included in both graphs in order to visualize trends. The equipotential lines in $\bar{\sigma}_3$ become linear for $g > g_c$. Note that the estimate for the critical interaction strength g_c is based on 3GP, so the actual critical value observed in FGP might differ, especially for larger values of K. For a fixed driving amplitude K, $\bar{\sigma}_3$ reaches its maximum at values of g slightly below g_c. The same trend can be observed for $\bar{\sigma}_5$ in Fig. 6.10b. The value of $\bar{\sigma}_5$ is below $7 \cdot 10^{-2}$ for the entire parameter range shown in Fig. 6.10. More precisely, $\bar{\sigma}_5$ lies one or more orders of magnitude below the corresponding value of $\bar{\sigma}_3$, indicating that the main contribution in $\bar{\sigma}_3$ comes from the intermediate modes $|1\rangle$ and $|\bar{1}\rangle$. Consequently, the calculations performed in the FGP approximation indicate that, for large K and g close to the self-trapping transition g_c (beyond which the system essentially remains in $|0\rangle$), the behavior experiences a significant influence from states beyond the three-state basis $0, \pm$.

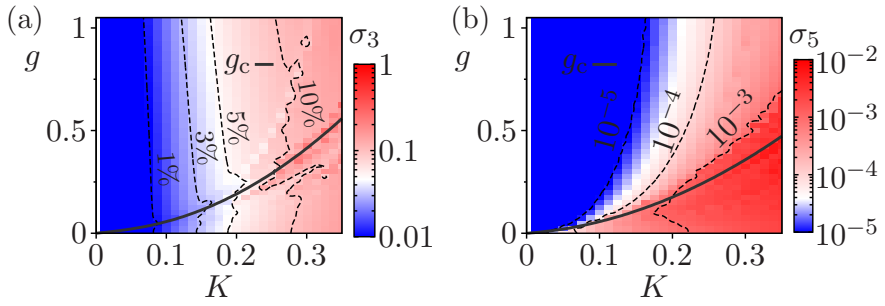

Figure 6.10.: *Contribution of the outside modes.* The averaging was done over 400 driving periods. Values that are smaller than a the threshold value 0.1 in (a) and 10^{-5} in (b), the threshold value is depicted. This way the solution of the values above this threshold improves in this kind of graphic. Further parameters are $\alpha = \beta = 0.2$ and $\Delta = \phi = \vartheta = 0$.

Conclusions

Describing a BEC-based Hamiltonian quantum ratchet in terms of a bosonic Josephson junction has been shown to be a very efficient approach to study the effects of particle interactions in these systems. For a sufficiently small amplitude of the driving potential, the few-mode description can be regarded as a good approximation. However, even for larger amplitudes, where discrepancies are stronger, it still serves as a powerful means to gain insight into the main mechanisms that lead to a certain dynamical behavior. Discrepancies between the full dynamics of the system and the effective description may arise due to particle interactions (for the case of ellipsoidal driving) or due to a coupling to intermediate states on a single-particle level. In contrast to a Josephson link, realized with a one dimensional double-well potential, in the here presented setups, the self-trapping regime finds its counterpart on a full many-body level.

7. Three-level system revisited

In Chapter 6, we saw that bosonic three-mode systems can show chaotic behavior within the mean-field approximation. In this chapter we will have a closer look on this dynamical regime, as well as on the self-trapping transition. The analysis, presented in the following, refers to all kinds of systems that are well described by a bosonic three-level Hamiltonian, cf. Eq. (6.10) [1]. Nevertheless, at some points we explicitly interpret the system as to describe a BEC-based Hamiltonian quantum ratchet.

A natural energy scale for systems that are described by Hamiltonian (6.10) is given by $\Gamma = \sqrt{|\Gamma_+|^2 + |\Gamma_-|^2}$, which will serve as energy scale in the following; and its inverse Γ^{-1} serves as time scale (we set $\hbar = 1$). As a result, the coupling among the modes can be expressed via a new parameter γ in the following manner

$$\hat{H} = \cos(\gamma) a_+^\dagger a_0 + \sin(\gamma) a_-^\dagger a_0 + \text{h.c.} + \bar{\mu}(\hat{n}_+ + \hat{n}_-) + \frac{\lambda'}{2} \sum_\nu \hat{n}_\nu (\hat{n}_\nu - 1). \tag{7.1}$$

As shown in Chapter 6, there exist at least two possible driving potentials which yield this Hamiltonian as truncated description of a Hamiltonian quantum ratchet. Therefore, it is rather inconvenient to analyze the dynamics in dependence on the parameters of each specific driving potential. Instead, we will study the dynamics of such a three-level system under variation of the effective parameters γ, $\bar{\mu}$, and λ'. The notation of the modes is the same as in the previous chapter $(-, 0, +)$ and we refer to the modes $|\pm\rangle$ as *side modes* and to $|0\rangle$ as *center mode*, as has been done so far as well. The Hamiltonian (7.1) has only three parameters γ, $\bar{\mu}$, and λ', which are obtained from the previously used parameters $\Gamma_\pm$, μ, and λ (cf. Chapters 5 and 6) as

$$\gamma = \arctan(|\Gamma_+|/|\Gamma_-|), \quad \lambda' = -\frac{\lambda}{2\pi\Gamma}, \text{ and } \bar{\mu} = \frac{\mu}{\Gamma}. \tag{7.2}$$

Furthermore, for a system with fixed number of particles we define the mean-field interaction strength $\bar{g} = (N-1)\lambda'$. For example, for the parameter set used in Fig. 6.8, we have $\Gamma_+/\Gamma_- = 7/3$, which gives $\Gamma \approx 0.0076$. From this follows $\gamma \approx 0.405$, and $\bar{g} = 0.209$ for $g = 0.01$, $\bar{g} = 1.672$ for $g = 0.08$, and $\bar{g} = 10.449$ for $g = 0.5$. The potential difference $\mu = 0.0025$ yields $\bar{\mu} = 0.328$.

For $\gamma = \pi/4$, the coupling terms of both side modes are equal, in which case the system is symmetric under a swap of the side modes. If Hamiltonian (7.1) is regarded as to describe a triple-well system, such a swap corresponds to the parity symmetry. Symmetric three-level systems have been extensively studied in Refs. [FP01a, YT10]. We will focus on the asymmetric case, i.e. $\gamma \neq \pi/4$, in this chapter. Throughout the following analysis refers to an initial preparation in which the system is fully condensed in the center mode.

[1] Some results presented in this chapter are published in Ref. [HCCS12] as part of this thesis. However, the present chapter provides a more general presentation, since the three-level Hamiltonian considered in Ref. [HCCS12] is regarded as a model for a specific ratchet system.

7.1. Self-trapping in two-mode BECs

For a two-level Bose gas, self-trapping is a well understood dynamical regime which occurs for strong particle interactions [SFGS97]. This regime can be observed when the potential energy difference between both modes vanishes and the condensate is initially located in one of the modes. In this case the interaction energy decreases during the transition to the other mode. If the particle interaction is so strong that this loss of interaction energy cannot be compensated by the single particle part of the Hamiltonian, the system remains trapped in the initial mode due to energy conservation. This regime has been experimentally observed for a BEC in a double-well potential [AGF+05].

Strictly speaking, the self-trapping regime is just an artifact of the GP approximation. Self-trapping does not occur with a full many-body description; but in any case the dynamics changes drastically: The tunneling times for a transition to the other mode become exponentially large (precisely, they become proportional to $\lambda'^N N!/N^2$ [CDFGM10]) and Schrödinger cat states are generated during the tunneling process. In this scenario, the tunneling process occurs in a qualitatively different manner as compared to the case of weakly interacting particles. Nevertheless, it has been shown by Carr et al. [CDFGM10] that even the slightest asymmetry in the system inhibits tunneling in the strongly interacting regime. This effect and decoherence due to interactions with the environment is what makes self-trapping a real physical phenomenon, instead of being just an artifact of the used approximation.

Furthermore, it is known that deep inside the self-trapping regime GP remains valid for long times and that this validity can be relatively well controlled by increasing the particle number [MCWW97]. Note that controlling the validity of GP by increasing the total particle number and decreasing the interaction strength turns out to have an inconvenient scaling even for weak mean-field interaction strengths. Precisely, one has to take the particle number squared, in order to double the time, which the system needs to accumulate a certain threshold of depletion [SSAC12].

7.2. Self-trapping and partial self-trapping in three-mode BECs

We have already seen that chaos can be observed in the system, when a third level participates in the dynamics. But this is not the end of the story. In fact, the system features another regime. It is characterized by the condensate being partially self-trapped in the subsystem that consists of the center mode and the side mode with the stronger coupling. It occurs for interaction strengths slightly below the critical interaction λ'_c, beyond which the system is entirely self-trapped in the initial mode. In Chapter 6, partial self-trapping was not mentioned as a proper regime of the system, because it can coincide with the chaotic motion.

The GP approximation of the system described by Hamiltonian (7.1) yields a nonlinear equation of motion for the expansion coefficients of the condensate orbital. Accordingly, in this limit the many-body state is given by

$$|\Psi\rangle = \frac{1}{\sqrt{N!}}(A_-\hat{a}_- + A_0\hat{a}_0 + A_+\hat{a}_+)^N |\mathrm{vac}\rangle \tag{7.3}$$

for all times, where $A_\nu(t)$ $(\nu = 0, \pm)$ are the time-dependent expansion coefficients of the condensate orbital. In the following we consider the dynamics governed by Hamiltonian (7.1) within the GP approximation, and initial condensate orbital given by $\mathbf{A} = (0, 1, 0)$. The time-dependent GP equation was solved with a linear multi-step

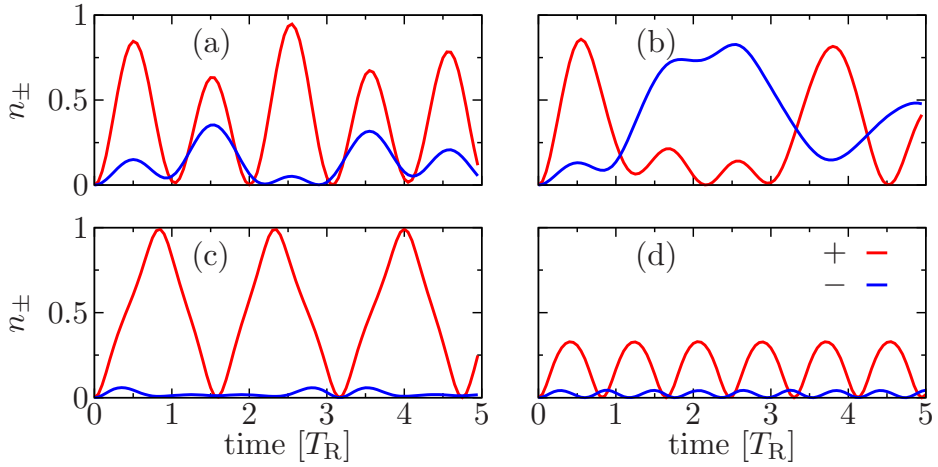

Figure 7.1.: *Occupation of the side modes for different dynamical regimes, obtained within the GP approximation.* Four different types of dynamics are considered (a) Quasi-periodic dynamics beyond Rabi where interactions are still relatively weak; (b) chaos; (c) partially self-trapped in the modes $|+\rangle$ and $|0\rangle$; (d) self-trapped in the initial mode 0. The key, given in (d) refers to all graphs. Parameters are $\gamma = \arctan(3/7)$ and $\mu = 0$. The values of λ' differ for each panel and are given below.

method[2].

Figure 7.1 shows the time evolution of the normalized occupation number of both side modes $n_\pm = |A_\pm|^2$ for four different values of λ' over the length of five Rabi cycles ($10\Gamma^{-1}$). In the quasi-periodic and in the chaotic regime, the system moves nearly freely among the modes, although with a possible imbalance for $\gamma \neq \pi/4$. In the partially self-trapped regime this imbalance is strongly enhanced, such that the mean occupation of the side modes may differ by an order of magnitude. The ratio between the time-averaged occupation numbers $r_\pm = \bar{n}_+/\bar{n}_-$, with $n_\pm$ given by

$$\bar{n}_\pm = \frac{1}{\tau}\int_0^\tau dt\, |A_\pm(t)|^2, \tag{7.4}$$

amounts to 22 in this regime; while one obtains $r_\pm = 3, 1, 8$ for the quasi-periodic, chaotic, and self-trapped regime, respectively. This observation can be used to predict the critical interaction strength for the self-trapping transition. We do this simply by ignoring the existence of the mode with the weaker coupling, which in practice is correct close to the self-trapping transition. In this way, the problem is reduced to the prediction of the self-trapping transition in a two-level system. For a symmetric two-level system, with the condensate being initialized in one of the modes, self-trapping occurs when the initial interaction strength exceeds the Rabi-frequency of the system. Hence, we obtain

$$\lambda'_\mathrm{c} = 4\max\{\cos(\gamma), \sin(\gamma)\} \tag{7.5}$$

as critical interaction strength for the three-level system given by Hamiltonian (7.1).

Figure 7.2 shows $\bar{n}_+$ for four different values of γ. The two extreme cases $\gamma = 0$ and $\gamma = \pi/4$ yield a system that is completely decoupled from the mode $|-\rangle$ and a completely ("parity") symmetric system, respectively. The other two values of γ yield non-zero but asymmetric coupling to both side modes. For the three asymmetric cases

[2]The integrator was provided by the python library *scipy*.

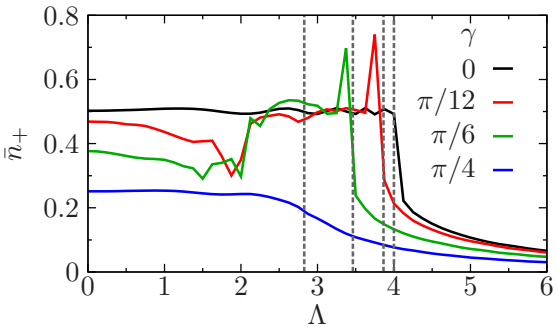

Figure 7.2: Time-averaged occupation of the side mode $|+\rangle$. The gray vertical lines indicate the transition points λ'_c, given in equation (7.5). Averages are performed over 10 Rabi cycles.

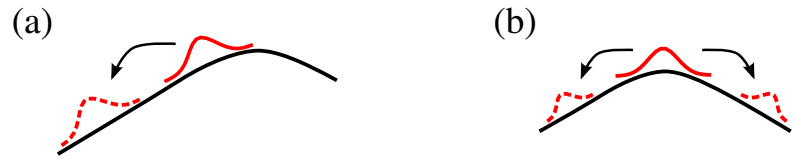

Figure 7.3.: *Quantum dynamics close to a classically unstable fixpoint.* The center of the hill represents two qualitatively distinct initializations: (a) Beneath an unstable fixpoint and (b) right on top of it.

($\gamma = 0, \pi/12, \pi/6$), the critical interaction strength is clearly indicated by the sharp edge of the curves. For the two intermediate values of γ, the edges are preceded by clear peaks. These peaks arise because for values of λ' slightly below λ'_c the system manages to perform one oscillation to the mode $|+\rangle$ and then gets basically stuck (or trapped) in this side mode. For the symmetric case the transition point cannot be clearly distinguished. The system enters the self-trapping regime in a rather smooth manner with increasing λ'.

If we take the point where the curves cross the horizontal line $\bar{n}_+ = \frac{1}{2}$ as the correct value for λ'_c, we obtain an error of about 2%, compared with our estimation (7.5), for all three asymmetric cases. The fact that this error is finite, indicates that the contribution of the other side mode does not vanish completely at the transition point. In a previous work the critical interaction strength for the self-trapping transition has been predicted numerically for a BEC in a symmetric triple-well [LFYL07], without providing analytical estimates.

The considerations above are obtained within the mean-field approximation. In this semi-classical picture, the self-trapping transition point marks an unstable fixpoint in the phase space of the system [MJCZ03]. A BEC that is initialized on such an unstable fixpoint gets faster depleted or even fragmented than for regimes with regular dynamics. Accordingly, the GP approximation fails after a short time. A heuristic picture of this phenomenon is shown in Fig. 7.3. The unstable fixpoint is represented by a peak of a hill, and the quantum system by a wave-packet. A classical particle that is initialized exactly on such an unstable fixpoint would stand still for all times. For a quantum particle, the *location* in phase space is always smeared out due to the Heisenberg principle. As a consequence, the system enters a superposition by moving simultaneously in both directions, away from the unstable fixpoint. This heuristic picture does also apply to the case of a BEC, but the definitions of the classical and the quantum limit are slightly different. In this case, the classical limit refers to a fully condensed system, which is correctly described by the GP equation and the quantum case refers to the full many-body description, given by the (second) quantized version of the GP equation. Accordingly, an unstable fixpoint within the mean-field limit can cause a rapid departure of the system from a full condensate. Unstable fixpoints are one example of a dynamical instability.

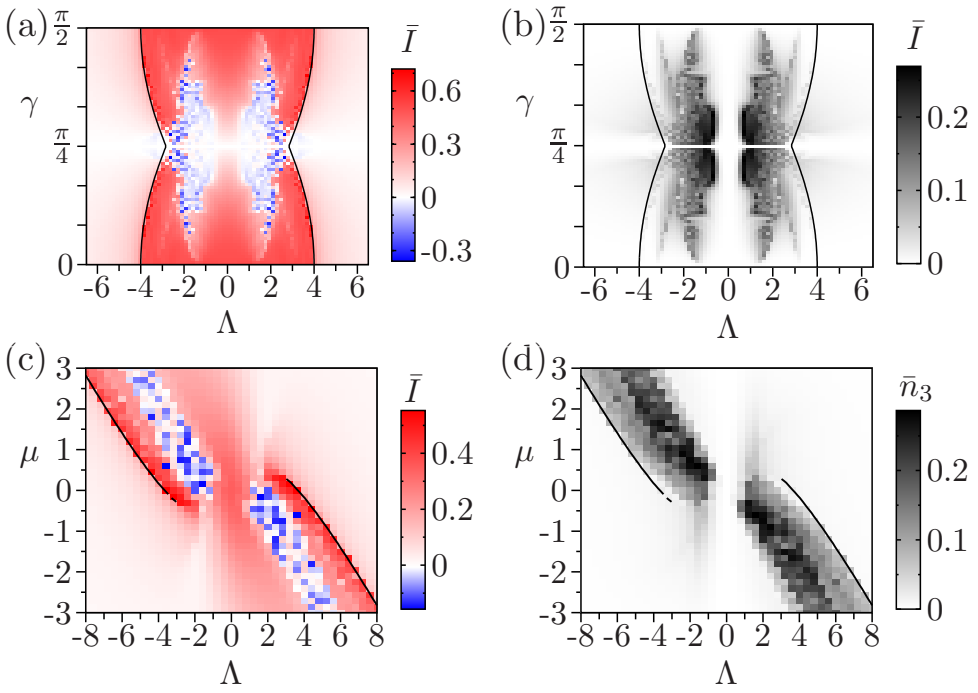

Figure 7.4.: *Parameter space symmetries.* Shown are (a,c) the time average of the population imbalance of the side modes (ratchet current); (b,d) the third largest eigenvalue of the time-averaged one-particle density matrix. Averages are taken over five Rabi periods ($5T_\mathrm{R}$). Parameters: $\omega = 1$ ($\Delta = 0$), $\alpha = \beta = 0.2$, $\varphi = 0$.

Another example would be chaotic motion, which will be studied in Section 7.4

7.3. Parameter space symmetries

Two-mode systems are known to feature interesting symmetries with respect to sign inversion of certain parameters [SSAC10, FP01b]. This section presents an analog symmetry analysis for the three-level Hamiltonian (7.1). Figures 7.4a,c show the time-averaged population imbalance of the side modes,

$$\bar{I} = \frac{1}{\tau}\int_0^\tau dt[n_+(t) - n_-(t)] = \bar{n}_+ - \bar{n}_-, \tag{7.6}$$

which is calculated after five Rabi periods, i.e. $\tau = 5T_\mathrm{R}$. If the Hamiltonian is to be understood as effective description of a ratchet system, this quantity is just the time-averaged particle current.

Two different cuts through parameter space are considered. The mirror symmetry in Fig. 7.4a and particularly the point symmetry in Fig. 7.4c suggest an interesting symmetry of the dynamics when both the parameters λ' and μ are inverted simultaneously, i.e. $(\lambda', \mu) \to (-\lambda', -\mu)$. Note that this symmetry is not a symmetry of the system in that sense that there exists a corresponding operator that commutes with the Hamiltonian (7.1). The related symmetry operation is present in parameter space. In order to study this symmetry, we introduce the basis transformation, defined as

$$\hat{R}\,|n_+ n_0 n_-\rangle = (-1)^{n_0}\,|n_+ n_0 n_-\rangle\,, \text{ i.e. } \hat{R}^\dagger a_0 \hat{R} = -1, \text{ and } \hat{R}^\dagger a_\pm \hat{R} = 1. \tag{7.7}$$

The introduced operator $\hat{R}$ is diagonal in number representation with diagonal values

being either 1 or -1. It thus satisfies the relations

$$\hat{R}^\dagger = \hat{R}, \text{ and } \hat{R}\hat{R} = 1. \tag{7.8}$$

It is straight forward to show that

$$\hat{R}\hat{H}(\lambda', \mu)\hat{R} = -H(-\lambda', -\mu). \tag{7.9}$$

From the second identity given in Eq. (7.8) follows

$$\hat{R}^n = \begin{cases} 1\,, & n \text{ even}, \\ \hat{R}\,, & n \text{ odd}, \end{cases} \qquad \text{for } n \in \mathbb{N}. \tag{7.10}$$

We can apply this property to obtain the following relation for the corresponding time evolution operator

$$e^{-\mathrm{i}t\hat{R}\hat{H}(\lambda',\mu)\hat{R}} = \hat{R}e^{\mathrm{i}t\hat{H}(-\lambda',-\mu)}\hat{R}. \tag{7.11}$$

This relation in turn, can be used for the calculation of the time evolution of $n_\nu = \langle a_\nu^\dagger a_\nu \rangle$. We obtain

$$\begin{aligned} n_\nu(t, -\lambda', -\mu) &= \langle 0N0 |\, e^{\mathrm{i}t\hat{H}(-\lambda',-\mu)} a_\nu^\dagger a_\nu e^{-\mathrm{i}t\hat{H}(-\lambda',-\mu)} \,| 0N0 \rangle \\ &= \langle 0N0 |\, \hat{R}e^{-\mathrm{i}t\hat{H}(\lambda',\mu)} \hat{R} a_\nu^\dagger a_\nu \hat{R} e^{\mathrm{i}t\hat{H}(\lambda',\mu)} \hat{R} \,| 0N0 \rangle \\ &= n_\nu(t, \lambda', \mu)^* = n_\nu(t, \lambda', \mu), \end{aligned} \tag{7.12}$$

what rigorously confirms our observations from the numerical data. Recently it was shown that such symmetry does also hold for an extended homogeneous Bose-Hubbard lattice [DSS+12].

Figures 7.4a and 7.4d show the effect of a potential energy shift of the side modes. It can be seen that the choice $\mu \neq 0$ leads to a shift of the dynamics towards stronger interactions. This effect can be understood by noting that, for nonzero values of μ, the degeneracy between the three states $|\pm\rangle$ and $|0\rangle$ disappears. Degeneracy is restored due to the massive initial occupation of $|0\rangle$, which lowers its energy via the mean-field interaction in Eq. (2.4). In other words, the effect of a positive μ is counteracted by an increase of the interaction strength. In particular, the starting degeneracy recovered with the help of interactions permits the onset of Rabi oscillations. If the considered system refers to a ratchet system, this explanation describes the shift of the resonance frequency due to particle interactions.

7.4. Chaos, depletion, and macroscopic superpositions

Within the GP approximation, the six dimensions of the complex valued triple (A_-, A_0, A_+) become reduced to an effectively three-dimensional phase space, due to conservation of total energy and norm, and due to separability of the global phase. A three-dimensional phase space allows for the occurrence of chaotic motion. This dynamical regime has already been observed in Chapter 6 and we will have a closer look on that regime in this section.

The parameter regimes for which chaotic motion is expected can be identified in Figs. 7.4b and 7.4d, which show the population n_3 of the third eigenstate of the time-averaged SPDM (calculated within GP)

$$\bar{\rho}_{\nu\nu'}(t) \equiv \frac{1}{t}\int_0^t dt' A_\nu^*(t') A_{\nu'}(t') \ . \tag{7.13}$$

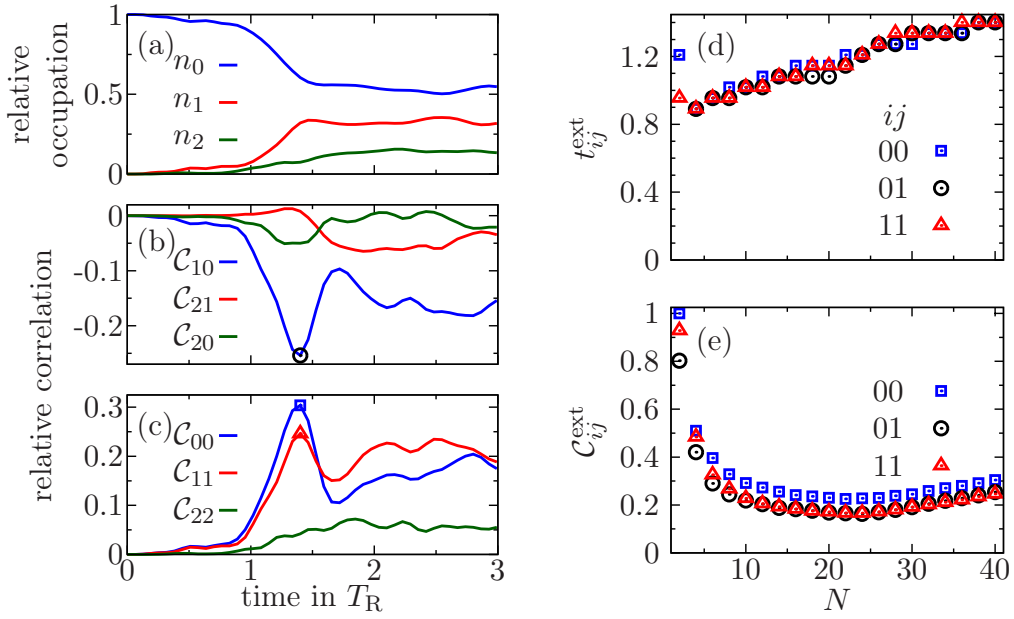

Figure 7.5.: *Correlated occupation in the chaotic regime.* (a) Normalized occupation numbers $n_i \equiv \langle n_i \rangle / N$ and (b-c) normalized particle number correlations $\mathcal{C}_{ij}$ of the (instantaneous) natural orbitals (eigenstates of the reduced one-particle density matrix) for $N = 40$ atoms. The time-point $t_{\max}$ of the local maximum of $\mathcal{C}_{00}$ [marked as a blue square in (c)] for different particle numbers N is given in (d) and its value $\mathcal{C}_{00}^{\max}$ is shown in (e) – same for the maximum of $\mathcal{C}_{11}$ (red triangles) and the minimum of $\mathcal{C}_{01}$ (black circles). In (a-c) parameters correspond to those of Figs. 6.8 c-d, the same holds for (d-e), except for the total particle number N, which is here plotted as a variable.

Comparison with Fig. 7.4a shows a clear correlation between the occupation of a third state and the suppression or weak reversal of the ratchet current. Both observations, suppression of ratchet current and increase of n_3, are clear indicators for chaotic dynamics, since for an ergodic system $\bar{\rho}_{\nu\nu'}(t)$ approaches the identity matrix for $t \to \infty$.

It was noted in Ref. [GJD+00] and hinted in a previous work [CD97] that chaotic motion within GP indicates the end of validity of this approximation. This was recently reexamined in Refs. [vCL+11, vLS+12]. Furthermore, in the previous section it was argued that this statement can even be generalized to any kind of dynamical instabilities. For the three-level system we are able to test the validity of GP directly for relatively high particle numbers. To this end we solve the many-body dynamics, using exact diagonalization, and analyze the relative occupation numbers of the natural orbitals. Those are obtained by diagonalizing the SPDM, defined in a many-body context as

$$\rho_{\mu\nu}^{(1)}(t) \equiv \langle \hat{a}_\mu^\dagger(t) \hat{a}_\nu(t) \rangle \,. \tag{7.14}$$

For the two limiting cases of Rabi oscillations and self-trapping the relative occupation of the condensate orbital (defined here as the most occupied eigenstate of $\rho^{(1)}$) stays above 98% during the first three Rabi cycles, which justifies a mean-field treatment. In contrast, for the chaotic regime, we find that the occupation of the condensate orbital decreases abruptly after about 2 Rabi periods and a second natural orbital gets macroscopically occupied, see Fig. 7.5a. This behavior is stable against variation of the total particle number.

In this chaotic regime, the macroscopic occupation of more than one orbital does not

occur via a simple fragmentation of the condensate into separable condensates. This can be seen in the particle number correlation functions $C_{ij} \equiv \langle n_i n_j \rangle - \langle n_i \rangle \langle n_j \rangle$, where i, j refer to the natural orbitals. In a system of separable condensates, i.e. a system of the type $a_i^{\dagger N/2} a_j^{\dagger N/2} |\mathrm{vac}\rangle$, $\mathcal{C}_{ij} \equiv 4C_{ij}/N^2$ would be zero (for $N \to \infty$), while for a noon (cat) type state, such as e.g.

$$|\mathrm{noon}\rangle = \frac{1}{\sqrt{2}}(|N00\rangle + |0N0\rangle), \tag{7.15}$$

its absolute value approaches unity, reflecting the creation of macroscopic particle number correlations. Figures 7.5b-c show the time-evolution of $\mathcal{C}_{ij}$ for the same parameter set as in Figs. 7.1c-d. We see that, with the decrease of the condensate fraction, some particle number correlations increase in a non-negligible way. In order to check the scaling of this behavior with the particle number, we focus on the local maximum of the variance of the condensate occupation ($\mathcal{C}_{00}$) for different particle numbers. Figure 7.5d shows that this maximum gets shifted to later times for higher N. The value of this maximum stays above 0.2 for all considered particle numbers and increases monotonically for $N > 25$, as shown in Fig. 7.5e. This indicates a scaling of the correlations C_{ij} with N^2, which in turn reveals noon-like (7.15) behavior, i.e., a dynamics dominated by a few many-body configurations differing by macroscopically large relative particle numbers. Similar observations have been made by Weiss and Teichmann [WT08], investigating a driven double-well system.

Thus we find that in this chaotic regime more than one orbital gets macroscopically occupied. At the same time the particle number correlation functions scale with the square of the total particle number. This indicates a complex dynamics in which the macroscopically large particle number correlations become a substantial feature.

7.5. Two coupled non-rigid pendula

Within the mean-field approximation, the Hamiltonian of a two mode BEC can be transformed to that of a nonrigid pendulum [SFGS97, Hol01]. These concepts have been extended to the case of the BEC with three modes [LFYL07]. The resulting Hamiltonian can be interpreted as describing two coupled nonrigid pendula. For completeness, we will see in the following how such a transformation is done for an asymmetric three-level system. The mean-field version of Hamiltonian (7.1) reads

$$\begin{aligned} H(\mathbf{A}, \mathbf{A}^*) = {} & \mathrm{c}_\gamma (A_+^* A_0 + A_0^* A_+) + \mathrm{s}_\gamma (A_-^* A_0 + A_0^* A_-) \\ & + \bar{\mu}(|A_-|^2 + |A_+|^2) + \tfrac{1}{2}\lambda'(|A_-|^4 + |A_0|^4 + |A_+|^4), \end{aligned} \tag{7.16}$$

where the vector $\mathbf{A} = (A_+, A_0, A_-)$ contains the amplitudes condensate wave-function with respect to the three modes. Together with the generalized momenta $\mathbf{A}^* = (A_+^*, A_0^*, A_-^*)$, they form the canonical coordinates of the six dimensional phase space. In our convention, the condensate wave-function is normalized to unity, i.e.

$$\sum_\nu |A_\nu|^2 = 1. \tag{7.17}$$

This normalization is conserved in time, which follows directly from the observation that $H(\mathbf{A}, \mathbf{A}^*)$ is a real-valued function. This means that the equations of motion for each

of the amplitudes A_ν and their canonical conjugate A_ν^*[3] reads

$$\mathrm{i}\dot{A}_\nu = \frac{\partial H}{\partial A_\nu^*} \text{ and } \mathrm{i}\dot{A}_\nu^* = -\frac{\partial H}{\partial A_\nu}. \tag{7.18}$$

The prefactors i in front of the time-derivatives appear, because, strictly speaking, the canonical momentum of the generalized coordinate A_μ is $-\mathrm{i}A_\mu^*$. Hence, this difference from the textbook version of Hamilton's equations is merely a question of conventions. The derivatives with respect to a complex number are defined by

$$\frac{\partial}{\partial A_\nu} \equiv \tfrac{1}{2}\Big(\frac{\partial}{\partial x} - \mathrm{i}\frac{\partial}{\partial y}\Big) \text{ and } \frac{\partial}{\partial A_\nu^*} \equiv \tfrac{1}{2}\Big(\frac{\partial}{\partial x} + \mathrm{i}\frac{\partial}{\partial y}\Big), \tag{7.19}$$

with x and y being the real and imaginary part of the complex numbers A_ν.

A canonical transformation to phase φ_ν and absolute n_ν, defined as

$$A_\nu = \sqrt{n_\nu}e^{\mathrm{i}\varphi_\nu} \text{ and } A_\nu^* = \sqrt{n_\nu}e^{-\mathrm{i}\varphi_\nu}, \tag{7.20}$$

yields the Hamiltonian

$$\begin{aligned} H(\varphi_\nu, n_\nu) = {} & \mathrm{c}_\gamma\sqrt{n_+ n_0}\cos(\varphi_+ - \varphi_0) + \mathrm{s}_\gamma\sqrt{n_- n_0}\cos(\varphi_- - \varphi_0) \\ & + \bar{\mu}(n_+ + n_-) + \tfrac{1}{2}\lambda'\sum_\nu n_\nu^2. \end{aligned} \tag{7.21}$$

A straight forward way to show that the transformation to the new generalized coordinates (φ_μ, n_μ) is a canonical transformation, is to calculate the Poisson brackets

$$\{-\mathrm{i}A_\mu^*, A_\nu\} = -\mathrm{i}\sum_\lambda \frac{\partial A_\mu^*}{\partial\varphi_\lambda}\frac{\partial A_\nu}{\partial n_\lambda} - \frac{\partial A_\mu^*}{\partial n_\lambda}\frac{\partial A_\nu}{\partial\varphi_\lambda} = \delta_{\mu\nu}, \tag{7.22}$$

when A_μ and A_μ^* are regarded as functions of φ_μ and n_μ. In this representation, the normalization condition (7.17) translates to $\sum_\nu n_\nu = 1$. Consequently, we can make a further canonical transformation, such that the norm of $\mathbf{A}$ becomes a canonical momentum. Fortunately, this transformation is linear and can be separated in a transformation for the phases φ_ν

$$\begin{pmatrix}\phi_+\\ \phi_0\\ \phi_-\end{pmatrix} = \begin{pmatrix}1 & -1 & 0\\ 0 & 1 & 0\\ 0 & -1 & 1\end{pmatrix}\begin{pmatrix}\varphi_+\\ \varphi_0\\ \varphi_-\end{pmatrix} \Leftrightarrow \begin{pmatrix}\varphi_+\\ \varphi_0\\ \varphi_-\end{pmatrix} = \begin{pmatrix}1 & 1 & 0\\ 0 & 1 & 0\\ 0 & 1 & 1\end{pmatrix}\begin{pmatrix}\phi_+\\ \phi_0\\ \phi_-\end{pmatrix}, \tag{7.23a}$$

and one for the absolute values n_ν

$$\begin{pmatrix}p_+\\ p_0\\ p_-\end{pmatrix} = \begin{pmatrix}1 & 0 & 0\\ 1 & 1 & 1\\ 0 & 0 & 1\end{pmatrix}\begin{pmatrix}n_+\\ n_0\\ n_-\end{pmatrix} \Leftrightarrow \begin{pmatrix}n_+\\ n_0\\ n_-\end{pmatrix} = \begin{pmatrix}1 & 0 & 0\\ -1 & 1 & -1\\ 0 & 0 & 1\end{pmatrix}\begin{pmatrix}p_+\\ p_0\\ p_-\end{pmatrix}. \tag{7.23b}$$

This transformation yields the Hamiltonian

$$\begin{aligned} H = {} & \mathrm{c}_\gamma\sqrt{p_+(1-p_- - p_+)}\cos(\phi_+) + \mathrm{s}_\gamma\sqrt{p_-(1-p_- - p_+)}\cos(\phi_-) \\ & + \bar{\mu}(p_+ + p_-) + \lambda'\Big(p_+(p_+ - 1) + p_-(p_- - 1) + p_+p_-\Big) + \frac{\lambda'}{2}, \end{aligned} \tag{7.24}$$

[3] In this representation the canonical conjugate of the generalized coordinates A_ν equal their complex conjugate.

where we have already used $p_0 = 1$. Hence, with these two transformation steps, we have obtained a Hamiltonian that is completely independent of the overall phase ϕ_0 and norm p_0. As a consequence, the dimension of the phase space has been effectively reduced to four. This reduction was possible because of particle number conservation. In principle, it is possible to further reduce the effective dimensionality to a three-dimensional phase space, due to conservation of total energy, but the required transformations are much harder to find.

Hamiltonian (7.24) can be regarded as the Hamiltonian of a system of two coupled non-rigid pendula, where the phases $\phi_\pm$ represent the angles and $p_\pm \leq 1$ the length of the rod.

An interesting observation is that the Hamiltonians (7.21) and (7.24) do not provide an obvious distinction between their linear and non-linear contributions, which in all cases is the term with the prefactor λ'.

Conclusions

A bosonic three-mode system features a much richer set of dynamical regimes as compared to its two-mode counterpart. Among these are Rabi oscillations, quasi periodic oscillations, chaos, partial self-trapping, dynamics that refer to an initialization *on top* of a classically unstable fixpoint, and the self-trapping regime. We were able to work out a semi-empiric formula for the critical interaction strength for the self-trapping transition when the system is initially fully condensed in the center mode. Furthermore, for this initial condition the time evolution of the expectation values of the occupation numbers of each mode is symmetric under an inversion of the particle interaction, which could be proven rigorously.

8. Conclusions

The results of this work can be subdivided into three conceptually different aspects: (*i*) the development of a mathematical approach for the study of periodically driven systems, (*ii*) the theoretical prediction of a novel manifestation of the Josephson effect (JE) in Bose-Einstein condensates (BECs), and (*iii*) the study of the role of particle interactions in Hamiltonian quantum ratchets (HQRs) based on BECs. Each of these results can be regarded as a consequence of its predecessor in this list. They will be discussed in detail in the following sections.

8.1. Approaching periodically driven systems

One of the main achievements, which may find applications for the study of a wide range of periodically driven systems, is the extension of the tt'-formalism to arbitrary time-periodic equations of motion (see Section 3.1). This framework was known so far to be a useful method to map a linear system with a time-dependent Hamiltonian to another linear system with a static Hamiltonian. Its extended version is applicable to a wide range of systems and should thus be valuable far beyond the scope of this thesis.

It was shown in Section 3.3 that the extended tt'-formalism provides a natural generalization of the concept of Floquet states to nonlinear systems. For a driven linear system, the Floquet states correspond to stationary states within the tt'-framework. Accordingly, nonlinear Floquet states can be defined as stationary solutions of the corresponding tt'-version of the underlying equation of motion.

A geometrical interpretation which helps to understand the mathematical concepts behind the extended tt'-formalism has been worked out as part of this thesis. According to this interpretation, the tt'-formalism describes the dynamics of a generalized loop which lives in the phase space of the system, cf. Fig. 3.1. The prediction of resonant driving frequencies in quantum ratchet systems was illustrated with a further geometric construct (see Figs. 5.3, 5.4, and 5.5), resembling the Ewald construction for the study of wave diffraction on a lattice.

8.2. Orbital Josephson effect

The application of the extended tt'-formalism to the Heisenberg equation of motion of field operators turns out to be a very efficient approach to study the role of particle interactions in resonantly driven BECs. In particular it was shown that periodic driving may lead to a novel manifestation of the Josephson effect in BECs. It arises by an effective truncation of the single-particle Hilbert space of a driven system to a few Floquet modes, which live in the extended Hilbert space of the tt'-formalism. The participating modes are characterized by center-of-mass wave functions, whose densities may overlap strongly. This characteristic gave rise to the name *orbital Josephson effect* (OJE).

Orbital Josephson junctions can be realized under very general assumptions (Section 4.2) and in a large variety of experimental setups. The corresponding few-mode description withstands comparison with simulations of the full-system, including a large

number of modes, see, e.g., Figs. 4.4 and 6.2. This numerical cross-check confirms its correctness over a large variety of dynamical regimes, such as Rabi oscillations, dynamical instabilities, such as chaos or a classically unstable fixpoint, and the self-trapping regime. For sufficiently weak driving amplitudes, the few-mode description can be regarded as a relatively precise approximation. However, when the amplitude of the driving potential becomes stronger, discrepancies may grow, but still it may be regarded as an efficient way to predict the occurrence of qualitatively different dynamical regimes and their corresponding regions in parameter space, for a given initial state.

8.3. Hamiltonian quantum ratchets

Another central result is the identification of the main dynamical processes that lead to a ratchet current for a very common type of ratchet potential (5.23), which has been used in an experiment by Salger et al. [SKH+09]. As a result, the ratchet current can be understood as originating from an *interference* between first and second order processes in the driving, which can be constructive in one direction and destructive in the other. These results are obtained within a single particle picture and are hence not limited the study of ratchet systems based on BECs.

The role of particle interactions in a BEC-based HQR can be well understood when it is regarded as realization of a bosonic Josephson junction with three modes: the zero angular momentum mode and two further modes with mutually opposite angular momenta. A surprising implication of this approach is that, within the description as bosonic Josephson junction, the particles do only interact with each other when they are in the same mode, although all modes share exactly the same region of space. The presence of a third mode allows for a richer variety of dynamical regimes as compared to bosonic two-mode systems. In particular, it is possible to observe chaotic dynamics within the GP approximation. This regime occurs at intermediate interaction strengths, between those connected to Rabi oscillations and to self-trapping.

The observation of chaos within the GP approximation indicates its failure and full many-body considerations become important. This departure from the mean-field limit due to chaos was analyzed in this work, and we have found hints for the occurrence of macroscopic superposition states (see Section 7.4).

8.4. Outlook

The extended tt'-formalism has to date only been successfully applied to study the dynamics of driven BECs. It is surely an enrichment of the mathematical toolbox for the treatment of time-periodic systems. However, predicting whether or not its application to other systems is practicable is difficult to assess.

So far the OJE lacks experimental evidence. Nevertheless, due to its considerable generality it could in principle, be readily realized in experiments with BECs. A possible candidate could be a BEC-based ratchet system of the type reported in Ref. [SKH+09]. In this experiment the particle density of the condensate cloud was lowered, such that the limit, in which the system is well described with a single particle picture, was reached.

Even without experimental realization, an orbital Josephson junction with three modes (see Chapter 6) may serve as an ideal ground for the theoretical study of out-of-equilibrium dynamics of many-body quantum systems. Due to their complexity and computational requirements, such systems are still to be explored. A question, which we will address in the future, is whether chaotic dynamics leads to a notable increase of spatial entanglement, which is a fundamental resource for quantum information processing. Already

intriguing signs have been seen in a preliminary study that the growth of spatial entanglement is uncorrelated to the qualitative dynamical regime of the corresponding semi-classical limit. This implies that the efficiency of the simulation of these systems based on the matrix product state formalism is independent of the dynamical regime in this limit. An important goal would be to confirm this behavior for large particle numbers.

Resumen en español

De acuerdo con la normativa relativa a la elaboración, defensa y evaluación de la tesis doctoral del Real Decreto 1393/2007, por el que se establece la ordenación de las enseñanzas universitarias oficiales de la Universidad Complutense de Madrid, a continuación se presenta un resumen en español de la tesis doctoral presente. Este resumen incluye una introducción al tema de la tesis, expone los objetivos principales y las aportaciones fundamentales de la misma y termina con las principales conclusiones.

Introducción y objetivos

Controlar materia mediante un campo periódico en el tiempo ofrece un emocionante panorama que proporciona la posibilidad de observar nuevos fenómenos y el diseño de nuevas aplicaciones técnicas. Un ejemplo bién conocido es el bombeo láser, que consiste en la excitación periódica de un medio activo para la creación de luz altamente intensa y coherente (luz láser) [Car63, Gou59]. Otro ejemplo es la conversión de un semiconductor a un medio conductor exponiéndolo a radiación electromagnética [MABW71]. De manera similar, la transición de un gas normal a plasma puede ser inducido por la aplicación de voltajes ac [Stu94] en el espectro de las radiofrecuencias. Por otra parte, la síntesis de materiales complejos puede ser enormemente acelerada con la ayuda de campos en el régimen de las microondas [CFFM05].

El objetivo de este trabajo es la introducción de herramientas matemáticas para el estudio de sistemas periódicos en el tiempo y en concreto está enfocado hacia el estudio de la dinámica de condensados de Bose-Einstein. Los siguientes párrafos proporcionan una visión conjunta de los experimentos más vanguardistas relativos a gases bosónicos ultrafríos y a la teoría subyacente. Además, se presta especial atención a la posibilidad de controlar estos sistemas mediante un campo periódico en el tiempo.

Gases atómicos ultrafríos

La implementación y el avance de sistemas de átomos ultrafríos permite estudiar la dinámica los átomos bajo la ausencia de efectos termales y de decoherencia. Los condensados de Bose-Einstein atómicos representan un paradigma de este tipo de sistemas. Originalmente, los condensados de Bose-Einstein surgen en un gas bosónico tridimensional al pasar por una transición de fase, cuando la temperatura traspasa un valor crítico T_{C}. La ocupación múltiple de un estado de una partícula es posible para partículas con espín entero (bosones), por el hecho de que no están sometidos al principio de Pauli. La obtención de los primeros condensados de Bose-Einstein ha sido galandonada con el premio Nobel en Física [AEM+95, DMA+95].

Control AC de sistemas de atomos ultrafríos

El uso de potenciales periódicos temporales para conseguir mas control sobre sistemas de átomos ultrafríos ha ganado mucha importancia en los últimos años. De hecho, una de las primeras trampas para el almacenamiento de condensados de Bose-Einstein fue creada por un potencial promedio orbitante [PAEC95]. La idea tras este tipo de pozo

de potencial es que el centro de la parte estática de la trampa oscile tan rápido que los átomos no sean capaces de responder. Esta idea de crear un potencial eficaz estático formado con una perturbación disonante es un concepto habitual en el campo de gases cuánticos ultrafríos.

Los condensados de Bose-Einstein están formados por átomos neutrales. Como consecuencia de ello, no es posible controlar su movimiento de la misma manera que el de los electrones en un circuito electrónico. Por eso, una meta fascinante del control AC de gases cuánticos es la inducción de corrientes de partículas a través de un potencial cuya fuerza promedio ni tire ni empuje. Este fenómeno se llama efecto trinquete y ocurre a causa de la rotura de las simetrías de inversión del espacio y del tiempo. Estas roturas de las simetría se pueden imponer al sistema a través de un campo externo. En el presente trabajo se analiza este tipo de efectos trinquetes.

Sinopsis de los resultados centrales de la tesis

Esta tesis introduce métodos novedosos para el estudio teórico de sistemas cuánticos de muchas partículas bajo la influencia de fuerzas periódicas en el tiempo. Dichos métodos están aplicados y minuciosamente analizados para el estudio de la dinámica de condensados de Bose-Einstein perturbados resonantemente con un potencial externo. En este contexto, el término resonancia hace referencia a aquellos casos en los cuales el potencial de control induce una unión entre varios orbitales del Hamiltoniano inicial. La dinámica de sistemas con interacciones entre las partículas puede ser muy compleja como se ve en este trabajo. El método introducido aquí permite representar el sistema perturbado a través de un Hamiltoniano estático que describe un gas de bosones que ocupan pocos estados. El contenido de esta tesis está subdividido de la siguiente manera:

El capítulo 2 presenta algunos cálculos básicos para sistemas mecánico-cuánticos de pocos estados. El resultado central de este capítulo es una fórmula para calcular el Hamiltoniano eficaz cuando una fracción de los estados participa sólo marginalmente en la dinámica. Además, contiene cálculos de promedios temporales de valores esperados de ciertas observables, así como la identificación de escalas temporales relevantes.

El capítulo 3 introduce un formalismo matemático para el tratamiento de sistemas periódicos en el tiempo: el formalismo tt' extendido. El capítulo comienza con una presentación de este formalismo usando hipótesis muy generales de la ecuación de movimiento subyacente. A continuación se discute su aplicación a tres tipos diferentes de ecuaciones de movimiento que son relevantes para esta tesis. Estas son: la ecuación de Schrödinger, la ecuación de Schrödinger no lineal y la ecuación de movimiento de Heisenberg para operadores de campo. En el primer caso se destaca su relación con la teoría de Floquet.

En el capítulo 4 los conceptos presentado en los capítulos anteriores son usados para la derivación de una descripción eficaz de un condensado controlado por un potencial temporalmente periodico. La estructura del correspondiente Hamiltoniano permite a los sistemas subyacentes ser considerados como uniones de Josephson bosónicas. Los estados participantes son funciones de onda cuyas densidades pueden solaparse considerablemente. Estas características dan lugar al nombre *effecto Josephson orbital*. Las derivaciones matemáticas en este capítulo están respaldadas por varias evidencias numéricas. Al comienzo de este capítulo se presenta una introducción a las uniones de Josephson bosónicas.

El capítulo 5 presenta un análisis de los mecanismos subyacentes para la creación de corrientes coherentes de trinquete en condensados de bosones ideales resonantemente perturbados. Se dedica especial atención a dos potenciales diferentes que producen un

Hamiltoniano estático eficaz. Para uno de los potenciales aplicados se utiliza una aproximación perturbacional del tipo presentado en el capítulo 2. Además, se introduce una construcción geométrica para determinar las condiciones de resonancia de una perturbación temporalmente periódica.

El capítulo 6 muestra cómo el concepto de uniones Josephson orbitales puede ser aplicado al estudio del rol de las interacciones entre las partículas en trinquetes cuánticos hamiltonianos. Se consideran los dos potenciales de trinquete introducidos en el capítulo 5 y, para uno de ellos, se presenta una minuciosa comparación numérica entre la descripción eficaz y los resultados obtenidos a través de un cálculo numérico más exacto (MCTDHB). Un resultado fundamental es que el método introducido aquí es correcto y en algunos casos preferible a una aproximación de campo medio, porque los efectos de muchos cuerpos pueden llegar a ser importantes.

El capítulo 7 profundiza en el estudio de la dinámica de un sistema bosónico de tres niveles. Se presta especial atención al régimen dinámico de autoatrapamiento y a la dinámica caótica. En el último caso, correlaciones entre los números de ocupación advierten la creación de estados de superposiciones macroscópicas.

Los apéndices presenta cálculos detallados que son necesarios para la comprensión de las derivaciones matemáticas de este trabajo pero que no tenían cabida en los capítulos principales. El apéndice A presenta detalles sobre el cálculo del exponente Lyapunov que se utiliza para identificar dinámicas caóticas. En el apéndice B se muestra que cualquier operador en un espacio de Fock bosónico o fermiónico puede expresarse en términos de operadores de creación y aniquilación. Finalmente, en el apéndice C se derivan las relaciones de conmutación de operadores de creación y aniquilación dentro del formalismo tt' extendido para el caso de una reducción del espacio de Hilbert a tres estados.

Conclusiones

Los resultados de este trabajo se pueden subdividir en tres aspectos conceptualmente diferentes: (*i*) el desarrollo de un método matemático para el estudio de un sistema periódico en el tiempo, (*ii*) la predicción teórica de una nueva manifestación del efecto de Josephson en condensados de Bose-Einstein y (*iii*) el estudio del rol de interacciones entre las partículas en un trinquete cuántico hamiltoniano basado en un condensado de Bose-Einstein.

Efecto Josephson orbital

La aplicación del formalismo tt' extendido a la ecuación de movimiento de Heisenberg de operadores de campo resulta ser un método muy eficiente para estudiar el rol de interacciones entre las partículas en un condensado de Bose-Einstein bajo la influencia de un potencial temporalmente periódico. En particular, se muestra que perturbaciones periódicas pueden llevar a una nueva manifestación del efecto Josephson en condensados de Bose-Einstein. Esto surge de una reducción del espacio de Hilbert a unos pocos estados de Floquet. Las características de los estados participantes dieron pie al nombre *efecto de Josephson orbital*.

Las uniones Josephson orbitales pueden realizarse bajo suposiciones muy generales (sección 4.2) y en una amplia variedad de sistemas experimentales. La correspondiente descripción eficaz se refuerza al compararla con cálculos numéricos más exactos del sistema y 6.2 y la comprobación numérica confirma su corrección en una gran variedad de regímenes dinámicos, tales como las oscilaciones de Rabi, dinámicas inestables como el

caos y el régimen de autoatrapamiento (ver por ejemplo las figuras 4.4). Para amplitudes del potencial externo suficientemente bajas, la descripción eficaz se puede considerar una aproximación relativamente precisa pero para amplitudes más altas pueden incrementarse las discrepancias. Sin embargo, la descripción eficaz en términos de una unión Josephson orbital puede seguir considerándose una manera eficiente para predecir la aparición de regímenes diferentes y dónde se encuentran en el espacio de parámetros.

Trinquetes cuanticos

Otro resultado central es la identificación de los procesos dinámicos principales que generan una corriente para un tipo de potencial de trinquete que ha sido utilizado en un experimento reciente [SKH+09]. Como resultado, la corriente de trinquete proviene de una interferencia entre procesos de primer y segundo orden respecto a un cálculo perturbativo. Dicha interferencia puede ser constructiva en una dirección y destructiva en la otra.

El rol de interacciones entre las partículas en trinquetes cuánticos hamiltonianos puede entenderse con facilidad si se considera como una unión de Josephson bosónica con tres estados: el estado de momento angular cero y dos estados más con momentos angulares mutuamente opuestos. La presencia de un tercer estado permite una mayor variedad de regímenes dinámicos en comparación con un sistema bosónico de dos estados. En particular, es posible observar dinámicas caóticas dentro de la aproximacion de campo medio.

Perspectivas

El formalismo tt' extendido ha sido aplicado con éxito únicamente al estudio de la dinámica de un condensado de Bose-Einstein. Seguramente, este formalismo supone un enriquecimiento del conjunto de herramientas matemáticas dedicadas al estudio de sistemas periódicos en el tiempo. Sin embargo es difícil predecir si es aplicable a más típos de sistemas.

Hasta la actualidad, el efecto Josephson orbital carece de evidencias experimentales. Sin embargo, debido a su considerable generalidad se podría observar fácilmente en experimentos actuales con condensados atómicos de Bose-Einstein. Un posible candidato podría ser un sistema de trinquete que ha sido presentado en la referencia [SKH+09]. En este experimento la densidad de partículas del condensado fue disminuida hasta tal punto que el sistema pudo ser considerado como un gas ideal.

Incluso sin la realización experimental, una unión de Josephson orbital con tres estados (ver capítulo 6) puede servir como una base ideal para el estudio teórico de dinámicas fuera del equilibrio en sistemas cuánticos de muchas partículas. Debido a su complejidad y requisitos computacionales, tales sistemas están aún por explorar.

A. Calculation of Lyapunov exponent within 3GP

This appendix[1] presents details on the calculation of the maximal Lyapunov exponent λ_{M} given in Fig. 6.9. The Lyapunov exponent reflects how fast the distance between two neighboring trajectories grows over time. The distance between two Hilbert space vectors can be quantified via the Euclidean norm,

$$d_2(\psi_1, \psi_2) \equiv \sqrt{\langle \psi_1 - \psi_2 | \psi_1 - \psi_2 \rangle}, \tag{A.1}$$

with $|\psi_1 - \psi_2\rangle \equiv |\psi_1\rangle - |\psi_2\rangle$. The maximal Lyapunov exponent for the trajectory $|\psi_0(t)\rangle$ is defined over the double limit

$$\lambda_{\mathrm{M}} \equiv \lim_{\psi_1 \to \psi_0} \lim_{t \to \infty} \frac{1}{t} \log \left[\frac{d(\psi_1(t), \psi_0(t))}{d(\psi_1(0), \psi_0(0))} \right], \tag{A.2}$$

where $|\psi_0(t)\rangle$ and $|\psi_1(t)\rangle$ are both solutions of the GP equation. Because of the Hamiltonian structure of the nonlinear Schrödinger equation, it is convenient to allow only perturbations that yield states with the same energy [vCL+11]. Within 3GP, the dynamics is given by the 3-tuple $\mathbf{A}(t) = (A_+(t), A_0(t), A_-(t))$, reflecting the expansion coefficients of the condensate orbital with respect to the three modes $\pm, 0$, cf. Section 7.5. In order to extract the Lyapunov exponent from the dynamics of the system, we consider the time evolution of the two initial states

$$\mathbf{A}_{\delta+} = \mathrm{N}_\delta(i\delta, 1, 0) \quad \text{and} \quad \mathbf{A}_{\delta-} = \mathrm{N}_\delta(0, 1, i\delta), \tag{A.3}$$

where $\mathrm{N}_\delta = 1/\sqrt{1+\delta^2}$ is the normalization factor. The parameter δ parameterizes the initial distance, $\sqrt{2}\delta$, between the trajectories $\mathbf{A}_{\delta\pm}(t)$. The Hamiltonian of both the states $\mathbf{A}_{\delta\pm}$ has the same value, and for $\delta = 0$, we recover the initial state considered here. Their time-dependent separation is denoted by $d_\delta(t) \equiv d_2(\mathbf{A}_{\delta+}(t), \mathbf{A}_{\delta-}(t))$, which will be used to estimate the Lyapunov exponent. The limit $\psi_1 \to \psi_0$ in the definition (A.2) translates into the limit $\delta \to 0$.

Figure A.1 shows the time evolution of $d_\delta(t)$ on a logarithmic scale for chaotic (a), and regular dynamics (b). Two different values of δ are considered. For chaotic dynamics the distance between the two trajectories $d_\delta(t)$ grows over several orders of magnitude, until it saturates at a value around unity. This saturation occurs because the distance $d_\delta(t)$ is bounded from above by the value 2, since both states $\mathbf{A}_{\delta\pm}$ are normalized to unity. The value of λ_{M} is estimated by fitting an exponential to the rising slope of $d_\delta(t)$ before saturation is reached. For the case shown we obtain $\lambda_{\mathrm{M}} \approx 0.097$ (0.08) for $\delta = 10^{-6}$ (10^{-5}). The estimated values thus have a relative difference of about 18%, which implies a high relative uncertainty. Nevertheless, the obtained value for λ_{M} is clearly positive, indicating chaotic dynamics.

In the regular regime $d_\delta(t)$ deviates by less than 10% of its initial value during the depicted time range, for both values of δ. Chaos can be precluded when the global

[1] The present appendix was published as part of this thesis in Ref. [HCCS12].

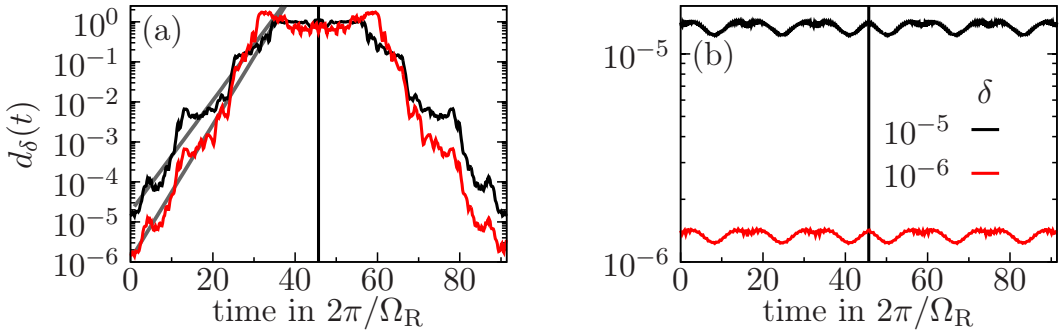

Figure A.1.: *Trajectory distances over time.* Two paradigmatic cases are considered: (a) chaotic, and (b) regular dynamics. After 45.7 Rabi cycles (vertical line) the time propagation is inverted to check the accuracy. The key in (b) refers to both panels. In (a), an exponential fit is included for both values of δ, given by the straight gray lines. Parameters [cf. Hamiltonian 7.1] are $\gamma = 0.405$, $\bar{g} = \lambda'(N-1) = 2.08$, $\mu = -0.66$ for (a), and $\mu = 1.97$ for (b).

maximum of $d_\delta(t)$ can be decreased by choosing smaller values for δ.

In all cases, the accuracy of the simulation was checked by propagating both the states $\mathbf{A}_{\delta\pm}$ backward in time after $t = 45.7$ Rabi cycles. The simulation is reliable, when $d_\delta(t)$ comes back to its starting value after $t = 91.4$ Rabi periods. This check is necessary to ensure that the observed separation of trajectories is not due merely to numerical errors.

Additionally calculated the maximal Lyapunov exponent was calculated by a different method described e.g. in Ref. [Sch88]. The results obtained by that approach confirm the results presented here, by identifying the same parameter regions as chaotic (and regular) and yielding values λ_M of similar magnitude.

B. Generators of Fock space

This appendix demonstrates that the creation and annihilation operators $\hat{a}_\ell^{(\dagger)}$ form a set of generators for all operators on Fock space, when we allow for infinite sums instead of polynomials (finite sums) to generate operators. This will be done in a constructive manner; thus by finding the expression of a given operator on Fock space in terms of the creation and annihilation operators.

For convenience, we assume a Fock space based on a finite set of L single-particle orbitals. That means, the basis[1] of Fock space is given by the (anti-) symmetrized product states

$$|n_1 \dots n_L\rangle\,, \tag{B.1}$$

where n_ℓ indicate the occupation number of the orbital that is characterized by the quantum number ℓ. Its range is $\mathbb{N}_0$ for a bosonic Fock space and $\{0, 1\}$ for fermionic particle statistics. A linear basis of the space of operators acting on Fock space is then given by

$$B_{\{\bar{n}\},\{n\}} \equiv |\bar{n}_1 \dots \bar{n}_L\rangle \langle n_1 \dots n_L| = \bigotimes_{\ell=1}^{L} |\bar{n}_\ell\rangle \langle n_\ell|\,, \tag{B.2}$$

where $\{n\}$ is a short form for the tuple of occupation numbers given on the right hand side. The latter equality underlines the fact that this basis can be written as tensorial product of basis operators that only act on a single single-particle orbital ℓ. The main idea of the present demonstration is to show that any of these basis operators can be expressed in terms of the creation and annihilation operators. From this follows directly that any operator can be expressed in such a way, which is what we want to show in this chapter.

To this end, we introduce the projection operator that projects any state onto the subspace in which the ℓth orbital is m-fold occupied

$$\hat{P}_\ell(m) \equiv \frac{1}{2\pi} \int_0^{2\pi} d\varphi e^{\mathrm{i}\varphi(\hat{n}_\ell^2 - m^2)}, \tag{B.3}$$

where $\hat{n}_\ell = \hat{a}_\ell^\dagger \hat{a}_\ell$ is the occupation number operator. This projector $\hat{P}_\ell(m)$ is generated by the pair of operators $(\hat{a}_\ell^\dagger, \hat{a}_\ell)$ via an infinite sum. The squares in the exponent make sure that negative signs, which occur in the case of a fermionic Fock space, cancel. For bosonic spaces, one could skip these squares. With fermionic operators, the projector (B.3) becomes simply $(1 - m - \hat{n}_\ell^2)$, where $m \in \{0, 1\}$.

The action of $\hat{P}_\ell(m)$ on a basis state is given by

$$\hat{P}_\ell(m)\,|n_1 \dots n_L\rangle = \delta_{m,n_\ell}\,|n_1 \dots n_L\rangle\,. \tag{B.4}$$

This projection is analog to the projection on angular momentum eigenstates [YL06], used as correction in symmetry-breaking mean-field approximations.

Each of the *factor* in the tensorial product in Eq. (B.2) can be expressed via the

[1] Strictly speaking, the sets that are labeled bases in this work are actually *complete orthonormal sets*. In agreement with many physics literature, and in contrast to literature on Hilbert space theory, these sets will be labeled bases.

projectors $\hat{P}_\ell(m)$, as

$$|\bar{m}_\ell\rangle\langle m_\ell| = \frac{1}{\sqrt{\bar{m}!m!}}\hat{P}_\ell(\bar{m})\hat{a}_\ell^{\dagger\bar{m}}\hat{a}_\ell^m\hat{P}_\ell(m). \tag{B.5}$$

With this identity, any basis operator $B_{\{\bar{n}\}\{n\}}$ can be constructed with the set of L creation and annihilation operators. Hence, any operator can be expressed with them as generators.

For practical purposes, such a construction is typically not necessary, since operators are usually considered in a first quantized context first and then translated to second quantization.

For a Fock space that is based on an infinite dimensional single particle Hilbert space $L \to \infty$, the tensorial product in Eq. (B.2) would be infinite, but none of the other steps would be affected.

Let us consider the particular case of a bosonic Fock space based on a single single-particle orbital ($L = 1$). In this case, all operators can be generated by a single pair of annihilation and creation operator. This is somewhat counterintuitive in two regards. (*i*) On one hand, one can show that the set of generators of of the space of $d \times d$-matrices, with d finite, contains d elements. An extrapolation of this result would yield an infinite set of generators for the space of infinite dimensional matrices. (*ii*) On the other hand, two bosonic Hilbert spaces with different sizes of single particle bases are isomorphic because they are both countable infinite dimensional. Hence, the spaces of operators acting on each of them is isomorphic as well. This implies that the set of generators referring to the larger single particle basis is not minimal, i.e. there exists a smaller set of generators to generate any operator acting on that space.

For completeness we will argue in the following that the minimal set of generators for an infinite dimensional Hilbert space, with countable basis, contains only two elements. A first step is to define an ordering of the basis states, such that any basis state $|\nu\rangle$ is given by a non-negative integer number $\nu \in \mathbb{N}_0$. With this ordering, one can define an abstract pair of *creation* and *annihilation* operator, whose action is given by

$$\hat{A}\,|\nu\rangle \equiv \sqrt{\nu}\,|\nu-1\rangle\,, \text{ and } \hat{A}^\dagger\,|\nu\rangle \equiv \sqrt{\nu+1}\,|\nu+1\rangle\,. \tag{B.6}$$

These operators $\hat{A}^{(\dagger)}$ can in general not be interpreted as creators or annihilators of particles, but they serve as a minimal set of generators to generate any operator that acts on the considered Hilbert space. Anyway, such an approach is probably not practicable in most cases.

C. Commutation relations in truncated Hilbert space

In this appendix we will go through all possible cases that have to be taken into account in order to show that Eqs. (3.49) transform to standard bosonic commutation relations when the Hilbert space is truncated to the three modes $\{-\kappa 1, 00, \kappa 1\}$, considered in Chapter 6.

The truncation consists in the assumption that modes (ℓ, m) other than $\{-\kappa 1, 00, \kappa 1\}$ do not participate in the dynamics, which in turn means that the related operators $\hat{a}^{(\dagger)}_{\ell m}$ do effectively vanish for $(\ell, m) \notin \{-\kappa 1, 00, \kappa 1\}$.

Unfortunately, there is no elegant way to obtain the commutation relations with such a truncation and we have to go through cases with different values of ℓ, ℓ', and m.

Commutators of annihilation and creation operators

In the full Hilbert space, the commutation relation between a creation and an annihilation operator reads

$$\sum_{m'} [\hat{a}_{\ell,m+m'}(t), \hat{a}^\dagger_{\ell' m'}(t)] = \delta_{\ell\ell'}\delta_{m0} \text{ for all } \ell, \ell', m. \tag{C.1}$$

Case $m = 0$, $\ell = -\kappa$, $\ell' = 0$**:**

$$\sum_{m'} \underbrace{[\hat{a}_{-\kappa,m'}, \hat{a}^\dagger_{0,m'}]}_{\text{always zero}} = 0 \qquad \Rightarrow \qquad 0 = 0. \tag{C.2}$$

The remark below the underbrace refers to the product of both operators in the commutator. This case does not provide information for the commutation rules within the truncated picture. In the following, we will focus on those cases that do provide information about the commutation relations within the truncated space.

Case $m = 0$, $\ell = \ell' = 0$**:**

$$\sum_{m'} \underbrace{[\hat{a}_{0,m'}, \hat{a}^\dagger_{0,m'}]}_{\text{zero except for } m'=0} = 1 \qquad \Rightarrow \qquad [\hat{a}_{0,0}, \hat{a}^\dagger_{0,0}] = 1. \tag{C.3}$$

Case $m = 0$, $\ell = \ell' = -\kappa$**:**

$$\sum_{m'} \underbrace{[\hat{a}_{-\kappa,m'}, \hat{a}^\dagger_{-\kappa,m'}]}_{\text{zero except for } m'=1} = 1 \qquad \Rightarrow \qquad [\hat{a}_{-\kappa,1}, \hat{a}^\dagger_{-\kappa,1}] = 1. \tag{C.4}$$

Analogously, the case $m = 0$, $\ell = \ell' = \kappa$ yields $[\hat{a}_{\kappa,1}, \hat{a}^\dagger_{\kappa,1}] = 1$.

Case $m = 1$, $\ell = \kappa$, $\ell' = 0$**:**

$$\sum_{m'} \underbrace{[\hat{a}_{\kappa,1+m'}, \hat{a}^\dagger_{0,m'}]}_{\text{zero except for } m'=0} = 0 \qquad \Rightarrow \qquad [\hat{a}_{\kappa,1}, \hat{a}^\dagger_{0,0}] = 0 \tag{C.5}$$

Analogously, the the case $m = 1$, $\ell = \kappa$, $\ell' = 0$ yields $[\hat{a}_{-\kappa,1}, \hat{a}^\dagger_{0,0}] = 0$.

Case $m = -1$, $\ell = 0$, $\ell' = \kappa$:

$$\sum_{m'} \underbrace{[\hat{a}_{0,-1+m'}, \hat{a}^\dagger_{\kappa,m'}]}_{\text{zero except for } m'=1} = 0 \qquad \Rightarrow \qquad [\hat{a}_{0,0}, \hat{a}^\dagger_{\kappa,1}] = 0. \tag{C.6}$$

Analogously, the case $m = -1$, $\ell = 0$, $\ell' = -\kappa$ yields $[\hat{a}_{0,0}, \hat{a}^\dagger_{-\kappa,1}] = 0$.

Commutator of annihilation operators

In the full Hilbert space, the commutation relation between two operators of particle annihilation operator reads

$$\sum_{m'} [\hat{a}_{\ell,m'-m}, \hat{a}_{\ell' m'}] = 0, \text{ for all } \ell, \ell', m. \tag{C.7}$$

Case $m = 0$, $\ell = \ell' = 0$:

$$\sum_{m'} \underbrace{[\hat{a}_{0,m'}, \hat{a}^\dagger_{0,m'}]}_{\text{zero except for } m'=0} = 0 \qquad \Rightarrow \qquad [\hat{a}_{0,0}, \hat{a}_{0,0}] = 0 \tag{C.8}$$

Case $m = -1$, $\ell = \kappa$, $\ell' = 0$:

$$\sum_{m'} \underbrace{[\hat{a}_{\kappa,m'+1}, \hat{a}^\dagger_{0,m'}]}_{\text{zero except for } m'=0} = 0 \qquad \Rightarrow \qquad [\hat{a}_{\kappa,1}, \hat{a}_{0,0}] = 0 \tag{C.9}$$

Case $m = 0$, $\ell = \kappa$, $\ell' = \kappa$:

$$\sum_{m'} \underbrace{[\hat{a}_{\kappa,m'}, \hat{a}_{\kappa,m'}]}_{\text{zero except for } m'=1} = 0 \qquad \Rightarrow \qquad [\hat{a}_{\kappa,1}, \hat{a}_{\kappa,1}] = 0 \tag{C.10}$$

Analogously, the case $m = 0$, $\ell = \ell' = \kappa$ ($\ell = \ell' = 0$) yields $[\hat{a}_{-\kappa,1}, \hat{a}_{-\kappa,1}] = 0$ ($[\hat{a}_{0,0}, \hat{a}_{0,0}] = 0$), and the case $m = 0$, and $\ell = -\ell' = \kappa$ yields $[\hat{a}_{\kappa,1}, \hat{a}_{-\kappa,1}] = 0$.

Commutator of creation operators

Since the Fourier transformation with respect to the parameter t' does not commute with the formation of the Hermitian adjoint (cf. Box 3.4.2), we cannot obtain the following cases simply by considering the Hermitian adjoint of the relations obtained in the previous section. In the full Hilbert space, the commutation relation between two operators of particle creation operator reads

$$\sum_{m'} [\hat{a}^\dagger_{\ell,m'-m}, \hat{a}^\dagger_{\ell'-m'}] = 0, \text{ for all } \ell, \ell', m. \tag{C.11}$$

Case $m = 0$, $\ell = \ell' = 0$:

$$\sum_{m'} \underbrace{[\hat{a}^\dagger_{0,m'}, \hat{a}^\dagger_{0,-m'}]}_{\text{zero except for } m'=0} = 0 \qquad \Rightarrow \qquad [\hat{a}^\dagger_{0,0}, \hat{a}^\dagger_{0,0}] = 0. \tag{C.12}$$

Case $m = -1$**,** $\ell = \kappa$**,** $\ell' = 0$**:**

$$\sum_{m'} \underbrace{[\hat{a}^\dagger_{\kappa,1+m'}, \hat{a}^\dagger_{0,-m'}]}_{\text{zero except for } m'=0} = 0 \qquad \Rightarrow \qquad [\hat{a}^\dagger_{\kappa,1}, \hat{a}^\dagger_{0,0}] = 0. \tag{C.13}$$

Case $m = -2$**,** $\ell = \kappa$**,** $\ell' = \kappa$**:**

$$\sum_{m'} \underbrace{[\hat{a}^\dagger_{\kappa,2+m'}, \hat{a}^\dagger_{\kappa,-m'}]}_{\text{zero except for } m'=-1} = 0 \qquad \Rightarrow \qquad [\hat{a}^\dagger_{\kappa,1}, \hat{a}^\dagger_{\kappa,1}] = 0. \tag{C.14}$$

Analogously, the case $m = -2$ and $\ell = \ell' = \kappa$ yields $[\hat{a}^\dagger_{-\kappa,1}, \hat{a}^\dagger_{-\kappa,1}] = 0$, and $\ell = -\ell' = \kappa$ yields $[\hat{a}^\dagger_{\kappa,1}, \hat{a}^\dagger_{-\kappa,1}] = 0$.

D. Glossary

Abbreviation or symbol	Explanation
BEC	Bose-Einstein condensate
GP	Gross-Pitaevskii (approximation)
CDT	coherent destruction of tunneling
TOP	time-averaged orbiting potential
QKR	quantum kicked rotor
BJJ	bosonic Josephson junction
OJE	orbital Josephson effect
RWA	rotating wave approximation
MCTDHB	multi configurational time-dependent Hartree for bosons
SPDM	single-particle density matrix
Sambe space	Hilbert space obtained by the tensor product of the *conventional* Hilbert space and the space of periodic functions
$\|\psi\rangle\rangle$	Notation for a vector that lives in Sambe space

Bibliography

[AEM+95] M. H. Anderson, J. R. Ensher, M. R. Matthews, C. E. Wieman, and E. A. Cornell, *Observation of Bose-Einstein condensation in a dilute atomic vapor*, Science **269**, 198 (1995).

[AGF+05] M. Albiez, R. Gati, J. Fölling, S. Hunsmann, M. Cristiani, and M. K. Oberthaler, *Direct observation of tunneling and nonlinear self-trapping in a single bosonic Josephson junction*, Phys. Rev. Lett. **95**, 010402 (2005).

[AGR06] A. S. Arnold, C. S. Garvie, and E. Riis, *Large magnetic storage ring for Bose-Einstein condensates*, Phys. Rev. A **73**, 041606 (2006).

[AM69] M. F. Atiyah and I. G. Macdonald, *Introduction to commutative algebra*, volume 19, Addison-Wesley Reading, MA (1969).

[AM76] N. W. Ashcroft and D. N. Mermin, *Solid state physics*, Holt, Rinehart and Winston, New York (1976), ISBN 0030839939.

[AR63] P. W. Anderson and J. M. Rowell, *Probable observation of the Josephson superconducting tunneling effect*, Phys. Rev. Lett. **10**, 230 (1963).

[ASC08] O. E. Alon, A. I. Streltsov, and L. S. Cederbaum, *Multiconfigurational time-dependent Hartree method for bosons: Many-body dynamics of bosonic systems*, Phys. Rev. A **77**, 033613 (2008).

[ATM+97] M. Andrews, C. Townsend, H.-J. Miesner, D. Durfee, D. Kurn, and W. Ketterle, *Observation of interference between two bose condensates*, Science **275**, 637 (1997).

[AV85] O. Avenel and E. Varoquaux, *Observation of singly quantized dissipation events obeying the Josephson frequency relation in the critical flow of superfluid* ^{4}He *through an aperture*, Phys. Rev. Lett. **55**, 2704 (1985).

[BCD+10] G. Benenti, G. Casati, S. Denisov, S. Flach, P. Hänggi, B. Li, and D. Poletti, *Comment on "coherent ratchets in driven Bose-Einstein condensates"*, Phys. Rev. Lett. **104**, 228901 (2010).

[BCPS91] F. Benvenuto, G. Casati, A. S. Pikovsky, and D. L. Shepelyansky, *Manifestations of classical and quantum chaos in nonlinear wave propagation*, Phys. Rev. A **44**, R3423 (1991).

[BDZ08] I. Bloch, J. Dalibard, and W. Zwerger, *Many-body physics with ultracold gases*, Rev. Mod. Phys. **80**, 885 (2008).

[BG12] T. Billam and S. Gardiner, *Coherence and instability in a driven Bose-Einstein condensate: a fully dynamical number-conserving approach*, New J. Phys. **14**, 013038 (2012).

[BnS12] P. Bargueño and F. Sols, *Macroscopic amplification of electroweak effects in molecular Bose-Einstein condensates*, Phys. Rev. A **85**, 021605 (2012).

[BSH97] C. C. Bradley, C. A. Sackett, and R. G. Hulet, *Bose-Einstein condensation of lithium: Observation of limited condensate number*, Phys. Rev. Lett. **78**, 985 (1997).

[BSSD04] V. Bretin, S. Stock, Y. Seurin, and J. Dalibard, *Fast rotation of a bose-einstein condensate*, Phys. Rev. Lett. **92**, 050403 (2004).

[Car63] T. R. Carver, *Optical pumping*, Science **141**, 599 (1963).

[CD97] Y. Castin and R. Dum, *Instability and depletion of an excited Bose-Einstein condensate in a trap*, Phys. Rev. Lett. **79**, 3553 (1997).

[CD98] Y. Castin and R. Dum, *Low-temperature Bose-Einstein condensates in time-dependent traps: Beyond the $U(1)$ symmetry-breaking approach*, Phys. Rev. A **57**, 3008 (1998).

[CDFGM10] L. D. Carr, D. R. Dounas-Frazer, and M. A. Garcia-March, *Dynamical realization of macroscopic superposition states of cold bosons in a tilted double well*, Europhys. Lett. **90**, 10005 (2010).

[CFFM05] D. E. Clark, D. C. Folz, C. E. Folgar, and M. M. Mahmoud, *Microwave Solutions for Ceramic Engineers*, American Ceramic Society, Westerville, Ohio (2005), ISBN 1574982249.

[CLMZ98] J. I. Cirac, M. Lewenstein, K. Mølmer, and P. Zoller, *Quantum superposition states of Bose-Einstein condensates*, Phys. Rev. A **57**, 1208 (1998).

[CM06] C. E. Creffield and T. S. Monteiro, *Tuning the Mott transition in a Bose-Einstein condensate by multiple photon absorption*, Phys. Rev. Lett. **96**, 210403 (2006).

[CMZ99] J. F. Corney, G. J. Milburn, and W. Zhang, *Weak-force detection using a double Bose-Einstein condensate*, Phys. Rev. A **59**, 4630 (1999).

[CS09] C. E. Creffield and F. Sols, *Coherent ratchets in driven Bose-Einstein condensates*, Phys. Rev. Lett. **103**, 200601 (2009).

[CS10] C. E. Creffield and F. Sols, *Reply*, Phys. Rev. Lett. **104**, 228902 (2010).

[CS11] C. E. Creffield and F. Sols, *Directed transport in driven optical lattices by gauge generation*, Phys. Rev. A **84**, 023630 (2011).

[DF01] S. Denisov and S. Flach, *Dynamical mechanisms of dc current generation in driven Hamiltonian systems*, Phys. Rev. E **64**, 056236 (2001).

[DGPS99] F. Dalfovo, S. Giorgini, L. P. Pitaevskii, and S. Stringari, *Theory of Bose-Einstein condensation in trapped gases*, Rev. Mod. Phys. **71**, 463 (1999).

[DKH09] S. Denisov, S. Kohler, and P. Hänggi, *Underdamped quantum ratchets*, Europhys. Lett. **85**, 40003 (2009).

[DKK+12] F. K. Diakonos, P. A. Kalozoumis, A. I. Karanikas, N. Manifavas, and P. Schmelcher, *Geometric-phase-propagator approach to time-dependent quantum systems*, Phys. Rev. A **85**, 062110 (2012).

[DMA+95] K. B. Davis, M.-O. Mewes, M. R. Andrews, N. J. van Druten, D. S. Durfee, D. M. Kurn, and W. Ketterle, *Bose-Einstein condensation in a gas of sodium atoms*, Phys. Rev. Lett. **75**, 3969 (1995).

[DMMFH07] S. Denisov, L. Morales-Molina, S. Flach, and P. Hänggi, *Periodically driven quantum ratchets: Symmetries and resonances*, Phys. Rev. A **75**, 063424 (2007).

[DSC02] W. Dür, C. Simon, and J. I. Cirac, *Effective size of certain macroscopic quantum superpositions*, Phys. Rev. Lett. **89**, 210402 (2002).

[DSS+12] A. Deuchert, K. Sakmann, A. I. Streltsov, O. E. Alon, and L. S. Cederbaum, *Dynamics and symmetries of a repulsively bound atom pair in an infinite optical lattice*, Phys. Rev. A **86**, 013618 (2012).

[Eco06] E. N. Economou, *Green's Functions in Quantum Physics*, Springer-Verlag, Berlin, Heidelberg (2006), ISBN 3540288384.

[Fey63] R. P. Feynman, *The Feynman lectures on physics, Vol.1*, Addison-Wesley Pub. Co, Massachusetts, USA (1963), ISBN 0201021161, chapter 46.

[FP01a] R. Franzosi and V. Penna, *Self-trapping mechanisms in the dynamics of three coupled Bose-Einstein condensates*, Phys. Rev. A **65**, 013601 (2001).

[FP01b] R. Franzosi and V. Penna, *Spectral properties of coupled Bose-Einstein condensates*, Phys. Rev. A **63**, 043609 (2001).

[FYZ00] S. Flach, O. Yevtushenko, and Y. Zolotaryuk, *Directed current due to broken time-space symmetry*, Phys. Rev. Lett. **84**, 2358 (2000).

[GBR05] R. Gommers, S. Bergamini, and F. Renzoni, *Dissipation-induced symmetry breaking in a driven optical lattice*, Phys. Rev. Lett. **95**, 073003 (2005).

[GCR+12] G. L. Gattobigio, A. Couvert, G. Reinaudi, B. Georgeot, and D. Guéry-Odelin, *Optically guided beam splitter for propagating matter waves*, Phys. Rev. Lett. **109**, 030403 (2012).

[GDJH91] F. Grossmann, T. Dittrich, P. Jung, and P. Hänggi, *Coherent destruction of tunneling*, Phys. Rev. Lett. **67**, 516 (1991).

[GH98] M. Grifoni and P. Hänggi, *Driven quantum tunneling*, Phys. Rep. **304**, 229 (1998).

[GHF+06] R. Gati, B. Hemmerling, J. Fölling, M. Albiez, and M. K. Oberthaler, *Noise thermometry with two weakly coupled Bose-Einstein condensates*, Phys. Rev. Lett. **96**, 130404 (2006).

[Gir60] M. Girardeau, *Relationship between systems of impenetrable bosons and fermions in one dimension*, J. Math. Phys. **1**, 516 (1960).

[GJD+00] S. A. Gardiner, D. Jaksch, R. Dum, J. I. Cirac, and P. Zoller, *Nonlinear matter wave dynamics with a chaotic potential*, Phys. Rev. A **62**, 023612 (2000).

[GKL+12] M. Gring, M. Kuhnert, T. Langen, T. Kitagawa, B. Rauer, M. Schreitl, I. Mazets, D. A. Smith, E. Demler, and J. Schmiedmayer, *Relaxation and prethermalization in an isolated quantum system*, Science **337**, 1318 (2012).

[GME+02] M. Greiner, O. Mandel, T. Esslinger, T. W. Hänsch, and I. Bloch, *Quantum phase transition from a superfluid to a Mott insulator in a gas of ultracold atoms*, Nature **415**, 39 (2002).

[Gou59] R. G. Gould, *The laser, light amplification by stimulated emission of radiation*, in *The Ann Arbor Conference on Optical Pumping, the University of Michigan*, volume 15, 128 (1959).

[GWH+05] A. Griesmaier, J. Werner, S. Hensler, J. Stuhler, and T. Pfau, *Bose-Einstein condensation of chromium*, Phys. Rev. Lett. **94**, 160401 (2005).

[HB11] D. Hochstuhl and M. Bonitz, *Two-photon ionization of helium studied with the multiconfigurational time-dependent Hartree–Fock method*, J. Chem. Phys. **134**, 084106 (2011).

[HCCS12] M. Heimsoth, C. E. Creffield, L. D. Carr, and F. Sols, *Orbital Josephson effect and interactions in driven atom condensates on a ring*, New J. Phys. **14**, 075023 (2012).

[HCS10] M. Heimsoth, C. E. Creffield, and F. Sols, *Weakly driven quantum coherent ratchets in cold-atom systems*, Phys. Rev. A **82**, 023607 (2010).

[HHC+] M. Heimsoth, D. Hochstuhl, C. E. Creffield, L. D. Carr, and F. Sols, *Effective Josephson dynamics in resonantly driven Bose-Einstein condensates* To be submitted.

[HMWC98] D. S. Hall, M. R. Matthews, C. E. Wieman, and E. A. Cornell, *Measurements of relative phase in two-component Bose-Einstein condensates*, Phys. Rev. Lett. **81**, 1543 (1998).

[Hol01] M. Holthaus, *Towards coherent control of a Bose-Einstein condensate in a double well*, Phys. Rev. A **64**, 011601 (2001).

[HRMB09] K. Henderson, C. Ryu, C. MacCormick, and M. G. Boshier, *Experimental demonstration of painting arbitrary and dynamic potentials for Bose-Einstein condensates*, New J. Phys. **11**, 043030 (2009).

[JAP97] F. Jülicher, A. Ajdari, and J. Prost, *Modeling molecular motors*, Rev. Mod. Phys. **69**, 1269 (1997).

[Jos62] B. Josephson, *Possible new effects in superconductive tunnelling*, Physics Letters **1**, 251 (1962).

[KCU08] R. Kanamoto, L. D. Carr, and M. Ueda, *Topological winding and unwinding in metastable Bose-Einstein condensates*, Phys. Rev. Lett. **100**, 060401 (2008).

[KKK+00] Y. Kagan, V. A. Kashurnikov, A. V. Krasavin, N. V. Prokof'ev, and B. Svistunov, *Quasicondensation in a two-dimensional interacting Bose gas*, Phys. Rev. A **61**, 043608 (2000).

[KS03] S. Kohler and F. Sols, *Chemical potential standard for atomic Bose-Einstein condensates*, New J. Phys. **5**, 94 (2003).

[LC11] S. Lepri and G. Casati, *Asymmetric wave propagation in nonlinear systems*, Phys. Rev. Lett. **106**, 164101 (2011).

[Leg01] A. J. Leggett, *Bose-Einstein condensation in the alkali gases: Some fundamental concepts*, Rev. Mod. Phys. **73**, 307 (2001).

[Leg06] A. Leggett, *Quantum liquids Bose condensation and Cooper pairing in condensed-matter systems*, Oxford University Press, Oxford New York (2006), ISBN 0198526431.

[LFYL07] B. Liu, L.-B. Fu, S.-P. Yang, and J. Liu, *Josephson oscillation and transition to self-trapping for Bose-Einstein condensates in a triple-well trap*, Phys. Rev. A **75**, 033601 (2007).

[LSA+07] M. Lewenstein, A. Sanpera, V. Ahufinger, B. Damski, A. Sen, and U. Sen, *Ultracold atomic gases in optical lattices: mimicking condensed matter physics and beyond*, Adv. Phys. **56**, 243 (2007).

[MABW71] K. E. Mortenson, A. L. Armstrong, J. M. Borrego, and J. F. White, *A review of bulk semiconductor microwave control components*, Proceedings of the IEEE **59**, 1191 (1971).

[MBS+12] S. Moulder, S. Beattie, R. P. Smith, N. Tammuz, and Z. Hadzibabic, *Quantized supercurrent decay in an annular Bose-Einstein condensate*, Phys. Rev. A **86**, 013629 (2012).

[MCL95] N. Moiseyev, M. Chrysos, and R. Lefebvre, *The solution of the time-dependent Schrödinger equation by the (t,t') method: application to intense field molecular photodissociation*, J. Phys. B-At. Mol. Opt. **28**, 2599 (1995).

[MCL+06] O. Morizot, Y. Colombe, V. Lorent, H. Perrin, and B. M. Garraway, *Ring trap for ultracold atoms*, Phys. Rev. A **74**, 023617 (2006).

[MCWW97] G. J. Milburn, J. Corney, E. M. Wright, and D. F. Walls, *Quantum dynamics of an atomic Bose-Einstein condensate in a double-well potential*, Phys. Rev. A **55**, 4318 (1997).

[MGS08] J. Martin, B. Georgeot, and D. L. Shepelyansky, *Time reversal of Bose-Einstein condensates*, Phys. Rev. Lett. **101**, 074102 (2008).

[MJCZ03] A. Micheli, D. Jaksch, J. I. Cirac, and P. Zoller, *Many-particle entanglement in two-component Bose-Einstein condensates*, Phys. Rev. A **67**, 013607 (2003).

[MMF08] L. Morales-Molina and S. Flach, *Resonant ratcheting of a Bose-Einstein condensate*, New J. Phys. **10**, 013008 (2008).

[MMR05] D. Masiello, S. B. McKagan, and W. P. Reinhardt, *Multiconfigurational hartree-fock theory for identical bosons in a double well*, Phys. Rev. A **72**, 063624 (2005).

[MO06] O. Morsch and M. Oberthaler, *Dynamics of Bose-Einstein condensates in optical lattices*, Rev. Mod. Phys. **78**, 179 (2006).

[MPG+03] J. B. Majer, J. Peguiron, M. Grifoni, M. Tusveld, and J. E. Mooij, *Quantum ratchet effect for vortices*, Phys. Rev. Lett. **90**, 056802 (2003).

[MS06] N. Moiseyev and T. Seideman, *Alignment of molecules by lasers: derivation of the Hamiltonian within the (t,t') formalism*, J. Phys. B-At. Mol. Opt. **39**, L211 (2006).

[MW97] N. Moiseyev and F. Weinhold, *High harmonic generation spectra of neutral helium by the complex-scaled (t,t') method: Role of dynamical electron correlation*, Phys. Rev. Lett. **78**, 2100 (1997).

[NZCZ01] B. Nordén, Y. Zolotaryuk, P. L. Christiansen, and A. V. Zolotaryuk, *Ratchet due to broken friction symmetry*, Phys. Rev. E **65**, 011110 (2001).

[PAEC95] W. Petrich, M. H. Anderson, J. R. Ensher, and E. A. Cornell, *Stable, tightly confining magnetic trap for evaporative cooling of neutral atoms*, Phys. Rev. Lett. **74**, 3352 (1995).

[Pap03] T. Papenbrock, *Ground-state properties of hard-core bosons in one-dimensional harmonic traps*, Phys. Rev. A **67**, 041601 (2003).

[PBC+09] D. Poletti, G. Benenti, G. Casati, P. Hänggi, and B. Li, *Steering Bose-Einstein condensates despite time symmetry*, Phys. Rev. Lett. **102**, 130604 (2009).

[PDJ+09] S. E. Pollack, D. Dries, M. Junker, Y. P. Chen, T. A. Corcovilos, and R. G. Hulet, *Extreme tunability of interactions in a* ^{7}Li *Bose-Einstein condensate*, Phys. Rev. Lett. **102**, 090402 (2009).

[PE96] J. M. Parrondo and P. Español, *Criticism of Feynman's analysis of the ratchet as an engine*, Am. J. Phys. **64**, 1125 (1996).

[PL83] P. Pfeifer and R. D. Levine, *A stationary formulation of time-dependent problems in quantum mechanics*, J. Chem. Phys. **79**, 5512 (1983).

[PM93] U. Peskin and N. Moiseyev, *The solution of the time-dependent Schrödinger equation by the (t,t') method: Theory, computational algorithm and applications*, J. Chem. Phys. **99**, 4590 (1993).

[PS03] L. Pitaevskii and S. Stringari, *Bose-Einstein condensation*, volume 116, Oxford University Press, USA (2003), ISBN 0198507194.

[PSSV11] A. Polkovnikov, K. Sengupta, A. Silva, and M. Vengalattore, *Colloquium: nonequilibrium dynamics of closed interacting quantum systems*, Rev. Mod. Phys. **83**, 863 (2011).

[PWM+04] B. Paredes, A. Widera, V. Murg, O. Mandel, S. Fölling, I. Cirac, G. V. Shlyapnikov, T. W. Hänsch, and I. Bloch, *Tonks–Girardeau gas of ultracold atoms in an optical lattice*, Nature **429**, 277 (2004).

[RAC+07] C. Ryu, M. F. Andersen, P. Cladé, V. Natarajan, K. Helmerson, and W. D. Phillips, *Observation of persistent flow of a Bose-Einstein condensate in a toroidal trap*, Phys. Rev. Lett. **99**, 260401 (2007).

[RAV+06] C. Ryu, M. F. Andersen, A. Vaziri, M. B. d'Arcy, J. M. Grossman, K. Helmerson, and W. D. Phillips, *High-order quantum resonances observed in a periodically kicked Bose-Einstein condensate*, Phys. Rev. Lett. **96**, 160403 (2006).

[RCGW98] J. Ruostekoski, M. J. Collett, R. Graham, and D. F. Walls, *Macroscopic superpositions of Bose-Einstein condensates*, Phys. Rev. A **57**, 511 (1998).

[RCM08] J. Reslen, C. E. Creffield, and T. S. Monteiro, *Dynamical instability in kicked Bose-Einstein condensates*, Phys. Rev. A **77**, 043621 (2008).

[RDO08] M. Rigol, V. Dunjko, and M. Olshanii, *Thermalization and its mechanism for generic isolated quantum systems*, Nature **452**, 854 (2008).

[Rei02] P. Reimann, *Brownian motors: Noisy transport far from equilibrium*, Phys. Rep. **361**, 57 (2002).

[RGH97] P. Reimann, M. Grifoni, and P. Hänggi, *Quantum ratchets*, Phys. Rev. Lett. **79**, 10 (1997).

[Ric78] R. D. Richtmyer, *Principles of Advanced Mathematical Physics*, volume I, Springer-Verlag, New York, Heidelberg, Berlin, first edition (1978), ISBN 0387088733.

[RWM+11] A. Ramanathan, K. C. Wright, S. R. Muniz, M. Zelan, W. T. Hill, C. J. Lobb, K. Helmerson, W. D. Phillips, and G. K. Campbell, *Superflow in a toroidal Bose-Einstein condensate: An atom circuit with a tunable weak link*, Phys. Rev. Lett. **106**, 130401 (2011).

[Sam73] H. Sambe, *Steady states and quasienergies of a quantum-mechanical system in an oscillating field*, Phys. Rev. A **7**, 2203 (1973).

[Sar77] M. Sargent, *Laser physics*, Perseus Books, Cambridge, Mass (1977), ISBN 0201069032.

[Sch88] H. G. Schuster, *Deterministic chaos : an introduction*, VCH Distribution, USA and Canada, VCH, Weinheim, Germany New York, NY, USA (1988), ISBN 3527268626.

[Sch07] F. Schwabl, *Quantenmechanik*, Springer-Verlag, Berlin, Heidelberg, 7th edition (2007), ISBN 9783540736745.

[SCTH11] R. P. Smith, R. L. D. Campbell, N. Tammuz, and Z. Hadzibabic, *Effects of interactions on the critical temperature of a trapped Bose gas*, Phys. Rev. Lett. **106**, 250403 (2011).

[SFGS97] A. Smerzi, S. Fantoni, S. Giovanazzi, and S. R. Shenoy, *Quantum coherent atomic tunneling between two trapped Bose-Einstein condensates*, Phys. Rev. Lett. **79**, 4950 (1997).

[Sha63] S. Shapiro, *Josephson currents in superconducting tunneling: The effect of microwaves and other observations*, Phys. Rev. Lett. **11**, 80 (1963).

[SKH+09] T. Salger, S. Kling, T. Hecking, C. Geckeler, L. Morales-Molina, and M. Weitz, *Directed transport of atoms in a Hamiltonian quantum ratchet*, Science **326**, 1241 (2009).

[Smo12] M. V. Smoluchowski, *Experimentell nachweisbare, der üblichen thermodynamik widersprechende molekularphenomene*, Phys. Z. **13**, 1069 (1912).

[SMOR11] J. Santos, R. A. Molina, J. Ortigoso, and M. Rodríguez, *Tailored particle current in an optical lattice by a weak time-symmetric harmonic potential*, Phys. Rev. A **84**, 023614 (2011).

[Sol99] F. Sols, *Josephson effect between Bose condensates*, in M. Inguscio, S. Stringari, and C. E. Wieman (Editors), *Bose-Einstein Condensation in Atomic Gases*, IOS Press (1999), ISBN 0967335558.

[SS99] R. W. Spekkens and J. E. Sipe, *Spatial fragmentation of a Bose-Einstein condensate in a double-well potential*, Phys. Rev. A **59**, 3868 (1999).

[SSAC09] K. Sakmann, A. I. Streltsov, O. E. Alon, and L. S. Cederbaum, *Exact quantum dynamics of a bosonic Josephson junction*, Phys. Rev. Lett. **103**, 220601 (2009).

[SSAC10] K. Sakmann, A. I. Streltsov, O. E. Alon, and L. S. Cederbaum, *Quantum dynamics of attractive versus repulsive bosonic Josephson junctions: Bose-Hubbard and full-Hamiltonian results*, Phys. Rev. A **82**, 013620 (2010).

[SSAC12] K. Sakmann, A. I. Streltsov, O. E. Alon, and L. S. Cederbaum, *Universality of fragmentation in the Schrödinger dynamics of bosonic Josephson junctions*, arXiv:1207.1011 (2012).

[Stu94] P. Sturrock, *Plasma physics : An introduction to the theory of astrophysical, geophysical, and laboratory plasmas*, Cambridge University Press, Cambridge England New York (1994), ISBN 0521448107.

[SVY+98] A. I. Safonov, S. A. Vasilyev, I. S. Yasnikov, I. I. Lukashevich, and S. Jaakkola, *Observation of quasicondensate in two-dimensional atomic hydrogen*, Phys. Rev. Lett. **81**, 4545 (1998).

[Tak05] S. Takagi, *Macroscopic quantum tunneling*, Cambridge Univ Pr, City (2005), ISBN 9780521675710.

[vCL+11] I. Březinová, L. A. Collins, K. Ludwig, B. I. Schneider, and J. Burgdörfer, *Wave chaos in the nonequilibrium dynamics of the Gross-Pitaevskii equation*, Phys. Rev. A **83**, 043611 (2011).

[vLS+12] I. Březinová, A. U. J. Lode, A. I. Streltsov, O. E. Alon, L. S. Cederbaum, and J. Burgdörfer, *Wave chaos as signature for depletion of a Bose-Einstein condensate*, Phys. Rev. A **86**, 013630 (2012).

[WDWD12] S. Wüster, B. J. Dabrowska-Wüster, and M. J. Davis, *Macroscopic quantum self-trapping in dynamical tunneling*, Phys. Rev. Lett. **109**, 080401 (2012).

[WHM+03] T. Weber, J. Herbig, M. Mark, H.-C. Nägerl, and R. Grimm, *Bose-Einstein condensation of cesium*, Science **299**, 232 (2003).

[WT08] C. Weiss and N. Teichmann, *Differences between mean-field dynamics and N-particle quantum dynamics as a signature of entanglement*, Phys. Rev. Lett. **100**, 140408 (2008).

[YL06] C. Yannouleas and U. Landman, *Symmetry breaking and Wigner molecules in few-electron quantum dots*, Phys. Status Solidi A **203**, 1160 (2006).

[YT10] M. Yasunaga and M. Tsubota, *Internal Josephson effects in spinor dipolar Bose-Einstein condensates*, Phys. Rev. A **81**, 023624 (2010).

[ZBSH96] I. Zapata, R. Bartussek, F. Sols, and P. Hänggi, *Voltage rectification by a SQUID ratchet*, Phys. Rev. Lett. **77**, 2292 (1996).

[Zib12] T. Zibold, *Classical bifurcation and entanglement generation in an internal bosonic Josephson junction*, Ph.D. thesis, Ruperto-Carola-University of Heidelberg, Germany (2012).

[ZNGO10] T. Zibold, E. Nicklas, C. Gross, and M. K. Oberthaler, *Classical bifurcation at the transition from Rabi to Josephson dynamics*, Phys. Rev. Lett. **105**, 204101 (2010).

[ZSL98] I. Zapata, F. Sols, and A. J. Leggett, *Josephson effect between trapped Bose-Einstein condensates*, Phys. Rev. A **57**, R28 (1998).

Acknowledgements

With these final paragraphs I want to thank all those people who supported me during the past four years, contributing to the success of this PhD thesis.

My foremost grateful words are pointed towards my advisors Charles Creffield and Fernando Sols for sharing their experience with me and for guiding me. In science, intuition is required in order to decide where to go. I think Fernando Sols is equipped with a high-quality intuition for physics and I thank him for sharing this with me. On the other hand, one has to be familiar with the tools of the trade, e.g. mathematical frameworks and numerical code; a part which was greatly filled in by Charles Creffield.

During this thesis, I had the fortune to collaborate with Lincoln Carr who had a decisive influence on the outcome of this work. I admire his dedication and his enthusiasm; and I thank him for hosting me in his group for more than five months, for inviting me over to Heidelberg and for being such a motivating guide.

I am deep indebted to Christopher for the uncountable discussions we had, for his advices, and opinions, and (important for the present work) for proofreading big parts of the thesis. Furthermore, I grateful acknowledge proofreading by Jürgen and Javier M., who where also among my first options to turn to with any kind of inquiry or simply chatting.

I owe a lot of gratitude to all my colleagues from the materials science department, especially Alicia P., Javier B. and Maria for proofreading the Spanish summary; but also my other officemates, Pedro, Alicia G., and all the other close colleagues for freshened discussions during lunch and at other times. I thank David for his collaboration and for being a friend.

The great help and mental support by Miguel-Ángel during the stay in Golden and afterwards is also not forgotten. At this point I also want to thank Jill and Paul whose support was an incredible gift from heaven. Ana, Kurt and I are fortunate to know them. Furthermore, I thank Michael and Teresa for support (physics related and not physics related) and for enjoyable afternoons in Golden.

My parents, my brother, and my sisters provide me a stable foundation for my live and give me the support I need. I also want to thank my Spanish family for adopting me and for supporting me. I thank my son for the hours he invested trying to distract me from physics problems.

Finally, I want to thank my beloved wife, Ana. I am fortunate to have her and no words of gratitude could ever capture the amount of gratitude I owe her. I Thank her for accompanying me in good and in bad. She is a coauthor of this chapter of my live and I know that there are many exciting chapters ahead, to be written together. This work is dedicated to her.